Universidade de Lisboa

Faculdade de Ciências

Departamento de Engenharia Geográfica, Geofísica e Energia

The dynamics of convective orographic precipitation: the transition to convection

Miguel Nogueira

Doutoramento em Ciências Geofísicas e da Geoinformação
(Meteorologia)

2014

Universidade de Lisboa

Faculdade de Ciências

Departamento de Engenharia Geográfica, Geofísica e Energia

The dynamics of convective orographic precipitation: the transition to convection

Miguel Nogueira

Tese orientada por:
Professor Doutor Pedro M. A. Miranda
Professora Doutora Ana P. Barros

Tese especialmente elaborada para a obtenção do grau de Doutor em Ciências Geofísicas e da Geoinformação (Meteorologia)

2014

Contents

Acknowledgements

I would like to thank both my advisors, Professor Pedro Miranda and Professor Ana Barros for their scientific guidance, support and for providing me with the opportunity to work in two fantastic research teams, both at Instituto Dom Luiz at the University of Lisbon and also at Duke University. I want to acknowledge all my colleagues in both groups with whom I had the pleasure of spending these past years. In particular I am grateful to Jing Tao for her tireless help with the hydrological modeling experiments and to Xiaoming Sun for sharing his remarkable WRF simulation efforts over the Andes.

I acknowledge the funding I received from the Fundação para a Ciência e Tecnologia (F.C.T.) under doctoral grant SFRH/BD/61148/2009. I also acknowledge the funding I received from project SMOG (Structure of MOist convection in high-resolution GNSS observations and models) funded by the Portuguese Science Foundation (PTDC/CTE-ATM/119922/2010*)* and project IPHEx (Integrated Precipitation and Hydrology Experiment) at Professor Barros research group at Duke University during this final year of my PhD, supported by NASA grant NNX13AH39G.

Agradeço todo o apoio que recebi da minha mãe, pai, avó e irmão, à família Albergaria e aos meus amigos. Finalmente agradeço à Raquel pelo apoio incondicional sem o qual não teria possível chegar aqui e ao Francisco pela enorme alegria que nos trouxe ao longo destes últimos meses.

Abstract

Multifractal behavior holds to a remarkable approximation over wide ranges of spatial scales in orographic rainfall and cloud fields. The scaling exponents characterizing this behavior are shown to be fundamentally transient with nonlinear dependencies on the particular atmospheric state and terrain forcing. In particular, a robust transition is found in the scaling parameters between non-convective (stable) and convective (unstable) regimes, with clear physical correspondence to the transition from stratiform to organized convective orographic precipitation. These results can explain two often reported scaling regimes for atmospheric wind, temperature and water observations. On the one hand, spectral slopes around 2-2.3 arise under non-convective or very weak convective conditions when the spatial patterns are dominated by large-scale gradients and landform. On the other hand, under convective conditions the scaling exponents generally fluctuate around 5/3, in agreement with the Kolmogorov turbulent regime accounting for the intermittency correction.

High-resolution numerical weather prediction (NWP) models are able to reproduce the ubiquitous scaling behavior of observed atmospheric fields down to their effective resolution length-scale, below which the variability is misrepresented by the model. The effective resolution is shown to be a transient property dependent on the particular simulated conditions and NWP formulation, implying that a blunt decrease in grid spacing without adjusting numerical techniques may not lead to the improvements desired.

Finally, the application of transient spatial scaling behavior for stochastic downscaling and sub-grid scale parameterization of cloud and rainfall fields is investigated. The proposed fractal methods are able to rapidly generate large ensembles of high-resolution statistically robust fields from the coarse resolution information alone, which can provide significant improvements for stochastic hydrological prediction and associated extreme event forecasting and risk management, and also for stochastic sub-grid parameterization of clouds with large potential to improve the current state-of-the-art cloud parameterization schemes.

KEYWORDS: orographic precipitation; convection; multifractals; stochastic parameterization; downscaling.

Resumo

A presente tese focou-se na dinâmica da precipitação orográfica, com particular interesse na transição para o regime convectivo que pode ser responsável por eventos de precipitação extrema, com riscos naturais importantes associados como inundações rápidas, deslizamentos de terras e avalanches de sedimentos. Os eventos de precipitação convectiva representam um enorme desafio do ponto de vista da previsão operacional devido ao seu carácter turbulento, com estrutura localizada e altamente transiente. Os modelos lineares conseguem explicar algumas propriedades importantes da iniciação de convecção e estrutura espacial dos campos resultantes de precipitação e nuvens orográficas, no entanto não conseguem fazer qualquer previsão quantitativa e só conseguem prever qualitativamente a estrutura (aproximadamente) correta em casos muito particulares. Isto deve-se essencialmente ao facto da importância de inúmeras interações não lineares na dinâmica destes eventos não poder ser ignorada. No presente estudo, investigou-se a estrutura multifractal dos campos de nuvens e precipitação orográfica, representando uma aproximação notável para as observações consideradas numa vasta gama de escalas espaciais desde comprimentos da ordem de 1 km até valores superiores a 500 km, capaz de representar a estrutura complexa destes campos com variabilidade numa vasta gama de escalas, resultante da interação de diversos processos não lineares com forte influência orográfica. Mostrou-se que o comportamento multifractal é deformando pela presença de numerosos zeros, característicos em campos de nuvens e precipitação devido à presença de limiares associados às transições de fase e outros efeitos não lineares. Utilizou-se análise de clusters para isolar as regiões chuvosas (i.e. regiões conexas sem zeros) realizando a análise multifractal apenas nestas regiões, recuperando a sua estrutura multifractal não deformada.

A análise multifractal de campos atmosféricos observados e simulados numericamente mostraram que os expoentes fractais que caracterizam o comportamento estocástico de invariância de escala são intrinsecamente transientes, com dependências não lineares nas condições particulares do estado da atmosfera e de forçamento topográfico. Em particular, encontraram-se ligações entre estes parâmetros e a velocidade média do vento, a forma do terreno e a estabilidade estática da atmosfera. Um resultado particularmente robusto foi a transição nos parâmetros fractais entre os regimes não-convectivo (estável) e convectivo (instável), com clara correspondência física com a transição entre precipitação orográfica

estratiforme e convectiva. Estes resultados mantêm-se válidos para análise espectral de Fourier, escalamento dos momentos estatísticos e funções estruturais, mesmo quando a deformação do comportamento multifractal devido à presença de zeros é explicitamente tomada em consideração. Estes resultados explicam dois regimes de invariância de escala amplamente encontrados em campos atmosféricos de vento, temperatura e água suas diversas fases. Por um lado, exponentes espectrais com valores de 2-2.3 surgem em situações não-convectivas ou com estruturas convectivas fracas, quando as distribuições espaciais são dominadas por gradientes de larga escala ou pela topografia. De facto, as propriedades de invariância de escala nestas situações são semelhantes ao comportamento fractal observado nos respetivos campos de elevação topográfica. Por outro lado, em condições convectivas os expoentes espectrais flutuam em torno do valor 5/3, de acordo com as previsões de Kolmogorov para o regime turbulento tomando em consideração as correções associadas à intermitência. O parâmetro de intermitência multifractal mostrou um comportamento semelhante, dando mais robustez aos resultados obtidos. Adicionalmente a simetria horizontal pode ser quebrada em certas ocasiões, gerando anisotropia horizontal no comportamento multifractal com importantes impactos nos campos atmosféricos.

Os modelos numéricos de previsão meteorológica são capazes de reproduzir o comportamento multifractal observado em campos atmosféricos até à escala correspondente à sua resolução efetiva. Abaixo desta escala a variabilidade é representada de forma errónea pelos modelos. Mostrou-se que a resolução efetiva é uma propriedade transiente que depende das condições particulares do sistema simulado e da própria formulação do modelo numérico, com particular sensibilidade a parametrização dos efeitos turbulentos de sub-escala e à difusão numérica, geralmente introduzida para manter a estabilidade das soluções numéricas. Estes efeitos tendem a causar uma remoção excessiva de variabilidade nas pequenas escalas, onde os expoentes espectrais apresentam valores não físicos superiores a 3. Nas escalas superiores à resolução efetiva o modelo representa de forma adequada a estrutura da atmosfera, mostrando que o aumento de resolução dinâmico realizado pelos modelos numéricos a partir do forçamento de resolução grosseira é capaz de conservar e representar as propriedades multifractais da atmosfera. Em particular, os resultados mostraram que nos casos convectivos o aumento de resolução de 6 km, onde um esquema de parametrização para a convecção tem que ser introduzido, para uma resolução de 1.2 km, onde as estruturas convectivas são parcialmente

resolvidas, resultou num aumento de resolução efetiva consideravelmente inferior à diminuição do espaçamento da grelha. Este resultado implica que a diminuição do espaçamento da grelha (i.e. aumento da resolução) por si só, sem um ajustar das técnicas de modelação numérica, poderá não levar à melhoria dos resultados da simulação desejados.

Investigou-se o potencial do comportamento multifractal transiente para aplicações estocásticas de parametrização de sub-escala e de aumento de resolução em campos de nuvens e precipitação. Os métodos fractais propostos têm a habilidade de gerar de forma célere numerosas realizações de alta-resolução estatisticamente robustas apenas a partir da informação de resolução grosseira, preservando a estrutura do forçamento e adicionando informação estatística útil nas escalas não resolvidos. No caso de aumento de resolução estocástico, a geração destes conjuntos de soluções plausíveis, todas elas com a estrutura estocástica coerente, é capaz de suprimir a lacuna de resolução entre os campos observados e simulados e as necessidades de alta resolução de muitas aplicações hidrometeorlógicas. Os resultados mostram que a metodologia proposta permite melhorias significativas na previsão probabilística de variáveis hidrometeorológicas, com importantes consequências para a previsão de eventos extremos e gestão de risco. No caso da parametrização estocástica de sub-escala de nuvens a distribuição de probabilidades é obtida com base em argumentos fractais. Os resultados mostraram que estes métodos representam uma melhoria considerável na representação da distribuição de probabilidades relativamente à distribuição log-normal, tanto nos extremos da distribuição como para intensidades intermédias. De facto, a parametrização estocástica fractal apresenta grande potencial para obter melhorias relativamente aos esquemas de parametrização do atual estado da arte. Adicionalmente consideração do comportamento transiente nestas metodologias fractais permite obter melhores representações da estrutura estatísticas de sub-escala, providenciando mais um argumento em favor do comportamento transiente da estrutura estatística da atmosfera. No entanto, a determinação a priori dos parâmetros fractais a partir da informação de resolução grosseira representa uma questão complexa e não resolvida, devido às numerosas dependências não-lineares que os parâmetros fractais apresentam e à reduzida dimensão da amostra que geralmente se verifica quando a análise estatística se baseia apenas numa realização dos campos de resolução grosseira. No caso de geração de campos de precipitação de alta-resolução para forçamento de modelos hidrológicos mostrou-se que a determinação transiente dos expoentes espectrais a partir da informação de resolução grosseira representa uma boa aproximação, com

resultados notavelmente superiores ao uso de outros métodos de interpolação não fractal, como por exemplo métodos bilineares. No entanto, este tipo de metodologia só pode ser usado quando os campos de resolução grosseira contêm informação suficiente que permitia uma análise estatística robusta, o que nem sempre se verifica. No caso de parametrização de sub-escala de nuvens, mostrou-se que o comportamento das caudas das distribuições de probabilidade são bem representadas quando se consideram valores para o expoente fractal de aproximadamente 5/3 no caso convectivo e aproximadamente 2.1 em casos não-convectivos ou se existirem apenas estruturas convectivas fracas. Finalmente mostrou-se que este tipo de métodos estocásticas baseados na estrutura fractal da atmosfera obtém melhores resultados quando usados para obter distribuições estatísticas plausíveis das variáveis de sub-escala e as respetivas incertezas, e não como métodos deterministas para gerar uma única realização de sub-escala, geralmente obtida como a média de várias realizações plausíveis o que introduz efeitos de alisamento. Este resultado está de acordo com a natureza estocástica dos métodos fractais e dos próprios sistemas turbulentos.

PALAVRAS CHAVE: precipitação orográfica, convecção; multifractais, parametrização estocástica; aumento de resolução

List of acronyms and abbreviations

CAPE	Convective Available Potential Energy
CIN	Convective INhibition
DTM	Double Trace Moment
EFPRB	East Fork Pigeon River Basin
ERA	European center for medium-range weather forecast Re-Analysis
fBS	Fractional Brownian Surface
GATE	Global atmospheric research program Atlantic Tropical Experiment
GFS	Global Forecast System
HRDI	High Resolution Domain of Interest
IPHEx	Integrated Precipitation and Hydrology Experiment
LST	Local Solar Time
MCS	Mesoscale Convective System
MPAS	Model for Prediction Across Scales
NCEP	National Center for Environmental Prediction
NCEP/CPC	National Center for Environmental Prediction Climate Prediction Center
NEXRAD	Next generation Radar Network
NMQ	National Mosaic and multisensor Quantitative precipitation estimates
NOAA	National Oceanic and Atmospheric Administration
NSSL	National Severe Storms Laboratory
NWP	Numerical Weather Prediction
PDF	Probability Distribution Function
PRB	Pigeon River Basin
QPE	Quantitative Precipitation Estimates

SALLJ	South Americal Low Level Jet
TRMM	Tropical Rainfall Measuring Mission
UM	Universal Multifractal
WFPRB	West Fork Pigeon River Basin
WRF	Weather Research and Forecast

List of symbols

C_1	Intermittency parameter
cf	cloud fraction
CAPE	Convective available potential energy
CIN	Convective inhibition
C_L	Fractal scaling adimensional coefficient
c_p	Specific heat capacity for dry air at constant pressure
c_l	Specific heat capacity for liquid water at constant pressure
D_f	Fractal dimension
E	Fourier power spectrum
f_R	Rainfall fraction
g	Gravitational acceleration
H	Non-conservation scaling parameter
h_m	Maximum topographic height
k	Radial wavenumber
(k_x,k_y,k_z)	Spatial wavenumber components
K(q)	Moment scaling exponent function
KE	Kinetic energy density
l	Measuring scale
L_0	Cascade outer scale; domain size
l_{sst}	2-dimensional sinusoidal small-scale terrain weavelength
M_q	q-order statistical moment
N_d	Dry Brunt-Väisälä frequency
N_m	Moist Brunt-Väisälä frequency

P_{ac}^{5h}	5 hour accumulated surface rainfall
p_s	Atmospheric pressure at surface level
p_t	Atmospheric pressure at top of the model grid level
q	Statistical moment order
q_c	Cloud water mixing ratio
q_l	Liquid water mixing ratio
q_s	Saturation mixing ratio
q_t	Total water mixing ratio
q_v	Water vapor mixing ratio
r^2	Linear regression coefficient of determination
RH	Relative humidity
T	Temperature
T_S	Surface temperature
(u,v,w)	Atmospheric wind velocity components
(U,V,W)	Mean atmospheric wind velocity components
V_H	Horizontal wind speed
(x_c,y_c)	Central position of Gaussian shaped topography
z_{qcmax}	Height of maximum cloud water mixing ratio
α	Multifractal parameter
β	Spectral scaling exponent
Δs	Horizontal grid spacing
Δx	Grid spacing in the x-direction
ε	Turbuelent energy flux
λ	Scale ratio
θ_e	Equivalent potential temperature

(σ_x, σ_y)	Decay parameters for Gaussian shaped topography in the (x,y) direction
τ_{adv}	Advective time-scale
φ	Conserved turbulent flux
ϕ_V	Vertically integrated water vapor flux
χ	Scalar variance flux
ω	Angular frequency
Γ_m	Moist adiabatic lapse rate

1 Introduction

Orography plays a fundamental role in the interaction between the land surface and the atmosphere on a wide variety of spatial and temporal scales, one of its most important effects being the modulation of rainfall patterns. The persistent topographic forcing is a major control on the global precipitation, widespread to all climate zones, commonly dominating the hydroclimatology over mountainous regions, causing differences in the mean annual precipitation of several hundred percent between windward slopes of orographic barriers and adjacent valleys or lee side slopes, giving rise to some of the most intense rainfall gradients on Earth and playing a major role in extreme precipitation events (e.g. Barros and Lettenmaier, 1994; Lang and Barros, 2002; Barros and Lang, 2003; Garreaud et al., 2003; Barros et al., 2004, 2006; Roe, 2005; Smith, 2006; Zipser et al., 2006; Bhusan and Barros, 2007; Giovanettone and Barros, 2009; Romatschke and Houze, 2010; Rasmussen and Houze Jr., 2011; Houze, 2012). Consequently, orographic precipitation processes have profound impacts far beyond the field of meteorology, affecting natural ecosystems, hydrology, agriculture, water resources and natural hazards management, and even the geology of many regions.

Fig. 1.1 a) stratiform orographic rainfall; b) convective orographic rainfall (adapted from Houze, 2012).

The perception of the profound influence of orography on precipitation dates back, at least, to Aristotle's Meteorologica that recognized the effect of mountains as "thick sponge overhanging the earth" as "they cool the vapor as it rises and condense again to water" and consequently "they receive the great volume of rain water that falls" (Roe, 2005). But it was not until the second half of the twentieth century that a proper theory of orographic rainfall started to emerge with the theoretical advances in atmospheric dynamics and thermodynamics, along with better observations of the atmosphere. Early reviews on orographic effects on rainfall were given by

Queney et al. (1960) and Smith (1979). Fig. 1a shows the classical picture of orographic precipitation where a prevailing wind is mechanically lifted over the windward flank, with moist air ascending adiabatically above its saturation (cloud base) level and hence causing condensation which leads to the generation and/or enhancement of clouds and precipitation. On the leeward flank, the cloud is evaporated as the air becomes unsaturated due to the descending motion together with decreased moisture and increased temperature caused by the windward precipitation effects, resulting in the well-known rain shadow effect. Under unstable or conditionally unstable conditions, the orographic uplift of the incoming flow together with terrain induced perturbations can bring air parcels above their level of free convection, leading to convective triggering and/or enhancement (Fig. 1b), strongly influencing the observed rainfall amounts and distribution. In a seminal work, Kuo (1963) undertook an analytical analysis of a linearized version of the Navier-Stokes equations to investigate convective triggering in unstable fluid flow. This hypothesis has motivated the application of linear stability analyses to study orographic convective precipitation, providing insight on the triggering, growth and structure of convective features and highlighting the important role of small-amplitude topographic variations in triggering and organizing orographic convection (Kirshbaum and Durran 2004, 2005a,b; Fuhrer and Schär, 2005, 2007; Kirshbaum et al., 2007a,b). Following these previous investigations, the linearized Navier-Stokes, continuity and thermodynamic equations can be reduced to a single wave equation for the vertical velocity, w, under the Boussinesq and inviscid approximations and neglecting earth rotation:

$$\left[\frac{\partial}{\partial t} + U\frac{\partial}{\partial x}\right]^2 (\nabla^2 w) + N_m{}^2 \nabla_{\mathrm{h}}{}^2 w = 0 \tag{1.1}$$

Where U is the mean wind, ∇^2 and $\nabla_{\mathrm{h}}{}^2$ are respectively the three-dimensional and horizontal Laplacian operator and N_m is the moist Brunt-Väisälä frequency of the saturated layer given by Eq. (1.2), which provides an appropriate measure of atmospheric stability in saturated layers as discussed by Emanuel (1994).

$$N_m{}^2 = \frac{1}{1+q_l}\left\{\Gamma_m \frac{d}{dz}\left[\left(c_p + c_l q_l\right) ln(\theta_e)\right] - \left[c_l \Gamma_m ln(T) + g\right]\frac{dq_l}{dz}\right\} \tag{1.2}$$

Here ql represents the liquid water mixing ratio, Γ_{m} is the moist adiabatic lapse rate, g is the acceleration due to gravity, θ_e is the equivalent potential temperature and c_{p} and c_{l} are

respectively the specific heat capacity for dry air and liquid water at constant pressure. A constant value is taken for ${N_m}^2$ in the linear framework for simplicity. By assuming plane-wave perturbations as solutions to Eq. (1.1) given by $w(x,y,z,t) = Ce^{i(k_x x + k_y y + k_z z - \omega t)}$ and considering solid wall boundary conditions at bottom and top boundaries, the following dispersion relation can be extracted:

$$\omega = \pm \sqrt{\frac{{k_x}^2 + {k_y}^2}{{k_x}^2 + {k_y}^2 + {k_z}^2} {N_m}^2} + k_x U \tag{1.3}$$

Where k_x, k_y and k_z represent the spatial wavenumber components. In the case of statically unstable stratification (${N_m}^2 < 0$) the physical solutions of the angular frequency, ω, equation are exponentially growing waves advected by the flow (e.g. Fuhrer and Schar, 2005). The respective growth rate for each small-scale disturbance mode of wavenumber $k = (k_x, k_y, k_z)$ can be estimated as the imaginary part of ω. In this inviscid formulation, maximum growth is obtained for largest possible vertical wavelength (limited by unstable cloud depth) and infinitesimally small horizontal wavelength. Admitting that small-scale disturbances are ubiquitous in the real atmosphere, this result was at odds the spatial scales and spacing between convective structures observed in nature. More realistic solutions capable of representing the observed finite scales governing orographic convective structures can be obtained by the introduction of a simplified (linear) viscosity term that modulates the solutions, strongly increasing the growth times at small horizontal wavelengths (Furher and Schar, 2005, 2007). Additionally, it has also been shown that it is important to take into account the finite amplitude of topographic perturbations upstream of the unstable cloud (Kirshbaum and Durran, 2007b) and to consider limited time-scales for advection (i.e. the in-cloud residence time of air parcels, controlled by mean wind speed and mountain width) and microphysical processes (i.e. the time period for rain production and fallout) (Kirshbaum and Durran, 2004, 2007b). The linear stability analysis revealed some ability in predicting the finite spacing between observed convective banded structures and their initial growth rates for events over low elevation topography, but their main contribution is the understanding of convective orographic features as the result of exponential growth of existing small-scale atmospheric perturbations in an unstable stratified layer, pointing out the importance of landform in controlling the location and occurrence of convective features, generating

unstable cap clouds by forced uplift of conditionally unstable flow and introducing finite amplitude wave perturbations upstream of the orographic cloud.

Detailed observational and modeling studies have shown that orographic precipitation processes encompass a rich set of physical processes such as forced uplift, blocking, channeling and convergence effects, radiative effects of diurnal cycle and differential heating and the resulting mesoscale breeze circulations, microphysical processes, seeder-feeder mechanisms, topographic gravity waves and convective triggering (see e.g. Barros and Lettenmaier, 1994; Roe, 2005; Smith, 2006 for reviews). Additionally, it was found that precipitation over and near mountains is mostly caused by modulation of impinging synoptic-scale weather systems, particularly with frontal systems, tropical cyclones and convective clouds (see Houze, 2012 for a recent review). These numerous non-linear processes modulate the atmospheric fields over a vast span of spatial and temporal scales, giving rise to complex orographic clouds and rainfall structures with variability over a wide spectrum of scales, from synoptic to local and down to microphysics and viscous dissipation scales. Investigations on the variability of orographic precipitation fields over wide ranges of scales have revealed the presence statistical scale-invariant behavior (Harris et al., 2001; Barros et al., 2004, 2006; Nykanen, 2008), hereafter referred to as scaling or fractal behavior as commonly denoted in the atmospheric science literature. The idea of scaling behavior derived from turbulent cascade schemes used to describe turbulent phenomenology since Richardson (1922) and is theoretically supported by the scale invariance symmetries of the Navier-Stokes equations governing atmospheric motion (Frisch, 1991). Over the past 30 years numerous investigations have provided with vast evidence for the presence of scaling behavior in atmospheric and other geophysical fields (see e.g. Veneziano et al., 2006; Lovejoy and Schertzer, 2007; Tuck, 2010 for reviews), implying that their statistical properties measured different scales are related to each other by a scale-changing operation (generally a power law) that involves only the scale ratio and a scaling exponent. Furthermore, these investigations have shown that for geophysical fields the scaling is generally determined not by one, but by infinity scaling exponents given by the scaling exponent function, i.e. they are multifractal. Complete descriptions of the mathematical formulation and analysis tools of multifractal behavior together with literature reviews on multifractal behavior in the atmosphere are provided is Chapters 2, 3 and 4 of the present thesis.

Numerical weather prediction (NWP) models represent a major research tool to investigate precipitating-producing mechanisms given their encouraging performance to reproduce and predict the main observed rainfall features (see e.g. Chow et al., 2013 for a recent discussion). However, the large number of involved nonlinear processes occurring at vast ranges of spatio-temporal scales drastically handicaps the ability of NWP models to provide with accurate quantitative predictions of precipitation and clouds (Randall et al., 2013; Macilwain, 2014). In particular, several deficiencies have been identified in terms of initiation, timing, intensity, location and structure of simulated convective features (Kain et al., 2013). Despite the considerable advances in computational power over the past decades, the allowed resolutions in NWP forecasts (typically around 1 km) can only partially represent individual convective elements and are altogether unable explicitly resolve very small-scale processes such as turbulence and cloud microphysics, which can have large impacts on the dynamical evolution of the atmosphere. Such fine resolutions as those required for resolving these effects will not be attained for operational weather forecasts, at least over the next 10-20 years. In fact, physical barriers might cause considerable issues in achieving such resolutions, for example power consumption and hardware-related reliability of massively parallel computation (Wedi, 2014; Macilwain, 2014). Consequently, the development of sub-grid parameterization strategies to represent the effect of the unresolved scales on the solution represents a very active research topic, posing a challenging problem because coarse and fine-scale fields are not mutually dependent, since the knowledge of the resolved field does not imply the knowledge of the sub-grid scale information, although the reverse is true. Despite the intensive efforts, the current sub-grid representations are oversimplified and often nonphysical representations based on bulk empirical formulas, with important impacts on the obtained solutions (e.g. Gianotti and Eltahir, 2013; Randall et al., 2013; Erlingis and Barros, 2014; Sun and Barros, 2014). Convective orographic precipitation events are particularly problematic due to their sensitivity to perturbations spanning over a wide range of scales introduced directly and indirectly (e.g. by radiation processes) by numerous physical mechanisms associated with interactions between atmosphere and terrain. In this sense, there is an urgent need to understand not only the physical mechanisms involved, but also the relationships between atmospheric variables at different spatial and temporal scales in order to obtain more realistic sub-grid scale parameterizations and downscaling schemes, capable of bridging the gap in resolution between the typically available

observed and simulated rainfall fields and the high-resolution requirements of many hydrometeorological applications, including water management and forecast of mountain hazards such and flashfloods, landslides and debris flows (e.g. Barros and Lettenmaier, 1994; Bindlish and Barros, 2000; Harris et al., 2001; Rebora et al., 2006, Tao and Barros, 2013, 2014a).

The present investigation aimed to improve the current limited understanding of orographic rainfall processes, particularly the transition between stratiform and convective regimes, traditionally used to classify orographic precipitation processes depending on the static stability of the air masses impinging upon the topographic obstacle (Cotton and Anthes, 1989). The presence of convective features can change the precipitation pattern and amount considerably, and can lead to localized extreme values of rainfall responsible for mountain hazards including landslides, debris flows and flashfloods. Additionally, three fundamental questions that currently present a great challenge for modelers and forecasters are addressed:

i) how can the structure of different orographic precipitation events be characterized based on the available knowledge of the dynamical atmospheric states?
ii) how is the transition between convective and stratiform regimes represented in such characterization, and what is the respective impact of these regimes on the structures of different atmospheric fields?
iii) how can this knowledge be used to improve the predictability of extreme events associated with orographic convective rainfall and also for applications of downscaling and sub-grid parameterization of rainfall and clouds fields?

This investigation was based on observations and high-resolution numerical simulations, both under idealized and real case setups in which linear stability analysis and, particularly, multifractal analysis are undertaken. Statistical multifractal analysis represents an important tool to understand the relationships between the statistics of orographic precipitation fields at different scales, with obvious importance and potential for sub-grid parameterization and downscaling applications. While the scaling behavior does in fact seem to be a ubiquitous property of atmospheric and geographical fields, the properties of such scaling behavior are poorly understood. Notoriously, whether scaling parameters characterizing the multifractal behavior of a given atmospheric field are universal (constant) as predicted by the classical

turbulence theory, or instead a transient property, is an important scientific question that remains open. Furthermore, if the transient hypothesis is assumed, then the dynamical dependencies of the scaling parameters must be investigated. Both these questions are thoroughly addressed in Chapters 2, 3 and 4 of the present thesis. Particular emphasis is given to the investigation of the possible differences between the statistical structure of stratiform and convective orographic events.

This thesis is organized into five main chapters, where Chapters 2, 3 and 4 are presented as self-contained scientific papers, published or submitted to publication. Chapter 5 summarizes the main overall conclusions of this investigation and gives an outlook to future research topics.

In Chapter 2 a linear stability analysis was used to gain insight on triggering, growth and structure of orographic rainfall and cloud fields generated by a population of three-dimensional fully nonlinear idealized cloud resolving numerical simulations under different climatological setups. The limitations of such simplified linearized theories and the extent to which they can be used to fully understand, predict and quantify nonlinear orographic convective circulations is investigated. The spatial scaling behavior of the simulated fields was also investigated, under a transient multifractal framework. The linkages between the scaling parameters and the particular atmospheric and terrain forcing were investigated, focusing on the transitions between stratiform and convective regimes.

In Chapter 3 advantage was taken of high spatial and temporal resolution rainfall estimates based on the dense weather radar network over the southern Appalachians. The effect of large zero fractions in heavily thresholded rainfall fields on the spatial scaling behavior was investigated and cluster analysis was used to characterize the scaling behavior of rainfall structures. Fractal methods were used for downscaling applications taking explicitly into account the transient nature of the scaling behavior. The resulting high-resolution rainfall products were tested as forcing for hydrological models to obtain ensemble stochastic forecasts of streamflow.

Chapter 4 presents a case study of fully realistic high-resolution numerical simulations of deep convective events under rainy season conditions and also dry winter conditions over the central Andes region. The spatial scaling behavior of wind and atmospheric water content fields were investigated, with particular focus on the non-convective/convective transition. Additionally, the

NWP effective resolution and sub-grid parameterization issues were investigated based on the spectral scaling behavior. Finally, the application of transient scale-invariant behavior for stochastic sub-grid parameterization of clouds is investigated.

2 Multifractal properties of embedded convective structures in orographic precipitation: toward subgrid-scale predictability*

Abstract

Rain and cloud fields produced by fully nonlinear idealized cloud resolving numerical simulations of orographic convective precipitation display statistical multiscaling behavior, implying that multifractal diagnostics should provide a physically robust basis for the downscaling and sub-grid scale parameterizations of moist processes. Our results show that the horizontal scaling exponent function (and respective multiscaling parameters) of the simulated rainfall and cloud fields varies with atmospheric and terrain properties, particularly small-scale terrain spectra, atmospheric stability, and advective timescale. This implies that multifractal diagnostics of moist processes for these simulations are fundamentally transient, exhibiting complex nonlinear behavior depending on atmospheric conditions and terrain forcing at each location. A particularly robust behavior found here is the transition of the multifractal parameters between stable and unstable cases, which has a clear physical correspondence to the transition from stratiform to organized (banded and cellular) convective regime. This result is reinforced by a similar behavior in the horizontal spectral exponent. Finally, our results indicate that although nonlinearly coupled fields (such as rain and clouds) have different scaling exponent functions, there are robust relationships with physical underpinnings between the scaling parameters that can be explored for hybrid dynamical-statistical downscaling.

* Nogueira[(1,2)], M., Barros[(2)], A. P., and Miranda[(1),] P. M., 2013: Multifractal properties of embedded convective structures in orographic precipitation: toward subgrid-scale predictability. Nonlinear Processes in Geophysics, 20 (5), 605-620.

(1) CGUL-IDL, University of Lisbon, Portugal.

(2) Duke University, Durham, North Carolina, U.S.A.

2.1 Introduction

It is often observed that air masses impinging upon a mountain range lead to the development of an orographic cloud with shallow embedded convective structures, which change the rainfall pattern and amount considerably, and can lead to localized extreme values of rainfall. These localized extremes present a great challenge for forecasters and are responsible for mountain hazards including landslides, debris flows and flashfloods.

The notion that embedded convective structures are the result of exponential growth of small-scale disturbances in an unstable stratified layer (Kuo, 1963) motivated the application of linear stability analyses to gain insight on the dynamics of orographic convective precipitation, including the estimation of the unstable growth rate, ω, for each small-scale disturbance mode of wavenumber $k = (k_x, k_y, k_z)$ (Fuhrer and Schär, 2005):

$$\omega = \sqrt{-N_m{}^2 \frac{k_x{}^2 + k_y{}^2}{k_x{}^2 + k_y{}^2 + k_z{}^2}} \tag{2.1}$$

$$N_m{}^2 = \frac{1}{1+q_w}\left\{\Gamma_m \frac{d}{dz}\left[\left(c_p + c_l q_w\right) ln(\theta_e)\right] - \left[c_l \Gamma_m ln(T) + g\right] \frac{dq_w}{dz}\right\} \tag{2.2}$$

where N_m is the moist Brunt-Väisälä frequency of the saturated layer (as defined by Emanuel, 1994), which has a negative value in the moist unstable case. In this inviscid formulation, the linear model predicts maximum growth for infinitesimally small horizontal wavelengths. Admitting that small-scale disturbances are ubiquitous in the real atmosphere, this does not agree with the observed finite spacing between bands observed in nature, for example: in western Kyushu in Japan (Yoshizaki et al., 2000), in the Cévennes region in southern France (Miniscloux et al., 2001; Cosma et al., 2002) and the Oregon Coastal Range (Kirshbaum and Durran, 2005b; Kirshbaum et al., 2007b). Kirshbaum et al. (2007a) developed a new (also inviscid) linear model that includes an upstream stable region where stationary small-scale lee waves are triggered and subsequently used as the initial disturbances for the convective region. Their model agrees with the results from numerical simulations that showed that such lee waves play a dominant role in triggering and organizing banded convection with finite spacing (Kirshbaum and Durran, 2005a; Fuhrer and Schär, 2007). Using both linear stability analysis and idealized numerical simulations, additional factors were also found to be important such as: (i) cloud depth (which

determines the minimum value of k_z allowed in Eq. 2.1) (Kirshbaum and Durran, 2004); (ii) the advective timescale, i.e. the in-cloud residence time of air parcels which can be controlled by mean wind speed and mountain width (Furher and Schär, 2005); (iii) dry stability outside the cloud layer (Kirshbaum and Durran 2005a); and (iv) cloud base height (Kirshbaum et al., 2007a).

A different approach to the problem has gradually developed concurrent but separately in the last thirty years, where the (statistical) scaling behavior of physical processes is explored. In these processes the statistical properties of a field at different scales are related by a scale-changing operation (generally a power law) that involves only the scale ratio and a scaling exponent, the simplicity of which is very appealing for statistical downscaling applications. In geophysical fields it is usually found that that the scaling is determined not by one, but by infinity of scaling exponents given by the scaling exponent function, i.e. they are multiscaling. Schertzer and Lovejoy (1987) proposed a functional form for this function, the Universal Multifractal (UM) model, briefly presented in Section 2.4. There are a number of publications reporting multiscaling behavior in various geophysical fields, including cloud and rain fields, over various temporal (see e.g. de Lima and de Lima, 2008 for a review) and spatial ranges, e.g. Schertzer and Lovejoy (1987). Nykanen (2008) found scaling on horizontal maps of radar rain reflectivity; Gupta and Waymire (1990) found scaling on spatial fields of oceanic rainfall; Tessier et al. (1993) and Barros et al. (2004) found scaling in satellite-based fields of cloud radiances. Recently, Lovejoy et al. (2008a) looked at TRMM product 2A25 near surface reflectivity from rain measurements and found evidence of multiplicative cascades from planetary scales down to a few kilometers (~4 km, the data set resolution) in the ensemble averaged scaling statistics. Also, note that the 2A25 product is an orbit based product with limited dimensions in the direction perpendicular to eh satellite movement. They argued that the UM model with well posed fixed values of the scaling parameters is a good approach when considering the entire range of scales. Stolle et al. (2009) showed that data from global models (including ERA40 reanalysis and NOAA GFS) also accurately follow cascade statistics from nearly 20,000 km down to around 100 km, where there was a cut off by hyper viscosity of the numerical model linked to grid resolution.

However, there is no consensus on the specific values of the scaling exponents (and associated UM parameters) and scaling ranges in the literature, although some of the differences might be

attributed to sample size or differences in measurements (sensors, measurement methods or measurement errors, etc.). Another view is that the scaling exponents vary depending on contextual environmental conditions, and therefore the observed variations can be attributed in part o physical processes. Over and Gupta (1994) also used 2-dimensional oceanic rainfall fields from GATE (GARP Atlantic Tropical Experiment), and proposed a relation between a scaling parameter and large-scale average rain (argued to be an index of synoptic-scale weather conditions); Perica and Foufoula-Georgiou (1996) related scaling parameters computed from horizontal rainfall radar fields to the Convective Available Potential Energy (CAPE) of the pre-storm environment over the same area; Deidda (2000) and Deidda et al. (2004) also found a dependency in one of their scaling parameters computed from radar reflectivity on the large-scale mean rainfall rate; and more recently Nykanen (2008) linked the variation in the values of the multiscale statistical parameters computed from radar rainfall fields to the underlying topographic elevation, predominant orographic forcing and storm location, and movement relative to the orographic cross-sections. These results suggest that UM parameters vary from event to event, or case-study to case-study as a function of atmospheric conditions, and local terrain parameters. If this behavior can be translated into robust relationships between UM parameters of particular states (e.g. precipitation) and the specific physical processes that determine the space-time evolution of these states (e.g. moist convection), then inference and induction modeling approaches can be used to develop quantitative dynamical models of the state of interest relying on knowledge of the specific physical processes alone. For instance, to predict precipitation fields over a wide range of spatial scales knowing atmospheric stability conditions and precipitation at one (coarser) scale. This type of modeling could be used to formulate parameterizations of unresolved processes in numerical weather and climate prediction models, and to predict states at spatial resolutions much finer than those resolved by models, or observations; that is, downscaling. In practical terms, this requires investigating possible relationships between physical properties and statistical parameters that would allow statistical downscaling from coarse to fine resolutions.

In the present work scaling analysis is performed on the output of highly idealized numerical simulations, in particular on surface accumulated rainfall fields and horizontal cross section of cloud water mixing ratio at several vertical levels. This gives us the opportunity to investigate horizontal scaling at several vertical levels at the same time instant, obtaining a horizontal

scaling regime for 3-dimensional physically consistent fields, instead of 2-dimensional fields used previously in the literature (see above). The behavior of the scaling parameters for varying configurations of small-scale terrain and upstream profiles is investigated under different idealized climatological regimes (presented in section 2.2), aiming to find physically based relationships between scaling parameters and atmospheric and terrain properties that can be estimated systematically from coarser resolution simulations. The paper is organized as follows: Section 2.2 presents the numerical setup; a summary interpretation of the simulation results in light of the linear theories is presented in Section 2.3; and the empirical scaling analysis is presented in Section 2.4. The multifractal analysis based on the statistical moments and the UM model is briefly presented in Section 2.4.1. These methods are then applied to the simulations results and the variation of the scaling properties with simulation parameters is investigated for both 2-dimensional rain and cloud fields (Sections 2.4.2) and 3-dimensional cloud fields (Sections 2.4.3). The scaling in different fields is compared in Section 2.4.4. In Section 2.4.5, scaling analysis based on Fourier power spectra is performed on the 3-dimensional cloud fields. The final section (Section 2.5) presents a summary and discussion of the main results.

2.2 Numerical Simulations

The numerical model advanced Weather and Research Forecasting (WRF) version 3.1 (Skamarock et al., 2008) is used to perform idealized cloud resolving simulations of conditionally unstable moist flow impinging upon a Gaussian shaped ridge (defined by Eq.2.3), elongated on the cross-flow direction, y, and with a maximum terrain height $h_m = 600\ m$. When the flow is lifted by orography, it saturates and releases latent heat generating an unstable orographic cloud where the embedded convective structures will develop.

$$h(x,y)=\begin{cases} h_m \exp\left[-\left(\left(\frac{x-x_c}{2\sigma_x}\right)^2+\left(\frac{y-y_c-4\sigma_y}{2\sigma_y}\right)^2\right)\right], & y-y_c<-4\sigma_y \\ h_m \exp\left[-\left(\left(\frac{x-x_c}{2\sigma_x}\right)^2\right)\right], & |y-y_c|\le 4\sigma_y \\ h_m \exp\left[-\left(\left(\frac{x-x_c}{2\sigma_x}\right)^2+\left(\frac{y-y_c-4\sigma_y}{2\sigma_y}\right)^2\right)\right], & y-y_c>4\sigma_y \end{cases} \quad (2.3)$$

Decay parameters σ_x and σ_y are 12.5 and 5 km respectively, and the center of the ridge is defined at $(x_c, y_c) = (80,60)km$. The resulting modified Gaussian ridge is represented in Fig. 2.1a. In all simulations the horizontal resolution is 250 m and there are 70 vertical terrain-following levels, unequally distributed over the 15 km of the domain, with vertical spacing stretching from lower to higher levels in order to have better resolution in the region where orographic clouds will develop. A Rayleigh damping layer is introduced in the top 5 km to reduce spurious reflections at the top. To simplify the problem, the parameterizations for radiation or surface and boundary layer are turned off, and the effects of earth's rotation are also neglected. The 3-dimensional Smagorinsky scheme is used for sub-grid turbulence closure.

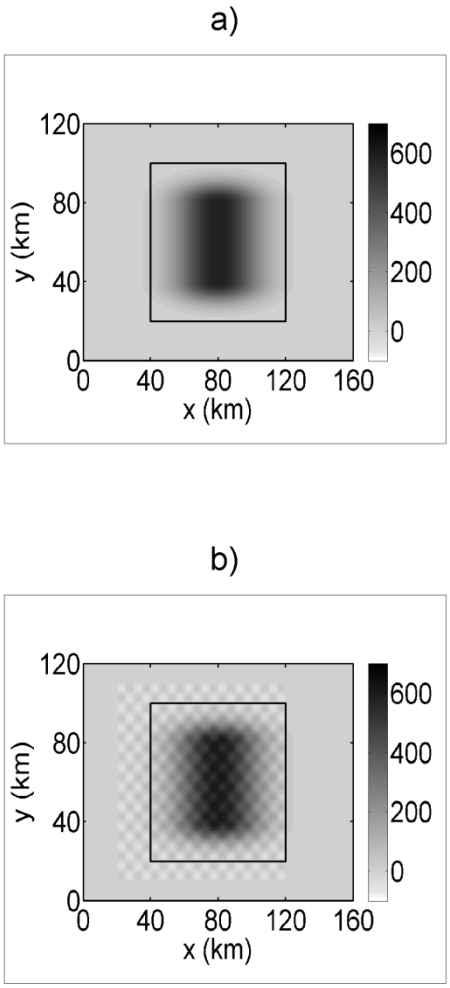

Figure 2.1. *Horizontal maps of topographic elevation (in meters) for simulations: a) CTL and b) Sst10km. The inner black square represents the domain of interest where the scaling analysis computations are performed.*

These highly idealized simulations are based on previous works of Kirshbaum and Durran (2005a,b) and Kirshbaum et al. (2007a,b) where the authors showed that they reproduce essential features of observed convective bands in the Oregon Coastal Range. The model resolution is fine enough to resolve the convective scale (see e.g. Fuhrer and Schär, 2007), and thus it is assumed that these simulations represent the appropriate convective structures. However, there are two important differences between the present simulations and previous work: i) the Thompson et al. microphysics scheme (available in WRF 3.1) including cold microphysics is used in this study instead of warm rain schemes, which may be difficult to justify in the case of orographic precipitation simulations; ii) the large-scale orography is a finite length ridge and open boundary conditions are used in this study for all lateral boundaries instead of a quasi-1-dimensional ridge with periodic boundary conditions in the y boundaries. Periodic boundary conditions used in previous studies would reintroduce small-scale disturbances in the domain reinforcing certain wavelengths, and would not allow the upstream stable flow to flow around the ridge, eventually forcing it all to transpose the orographic barrier.

The upstream profiles are also highly idealized, initially being horizontally homogeneous. In order to constrain the parameter space, they are defined in a very simple manner by a background flow in the *x*-direction ($V = W = 0$) without shear ($U(z) = const$), a constant stable dry Brunt-Väisälä frequency ($N_d = 0.01\ s^{-1}$), a constant surface temperature,T_S, and a relative humidity profile defined by three separate layers: $RH = 90\%$ from the surface to 2500 m, followed by linear decay from 90% to 1% from 2500 m to 3500 m, and then $RH = 1\%$ above 3500 m. Small-scale topography is added by superposing a 2-dimensional sinusoidal field with a maximum amplitude of 50 m (which is less than 10% of h_m), and the same wavelength in the x and y directions ($l_{sst_x} = l_{sst_y} = l_{sst}$) (Fig. 2.1b). The base case simulation, called Sst10km, has $l_{sst} = 10\ km$, $T_S = 285\ K$ and $U = 10\ ms^{-1}$. A population of simulations is built from the base case by varying one of the simulation parameters (l_{sst}, T_s and U) at a time, while keeping the other parameters constant (see Table 2.1 for a summary of the population of WRF simulations conducted in this study). The particular choice of parameters derives from the physical intuition given by linear stability analysis on embedded convection briefly presented above. In this simple setup ${N_m}^2$ is varied by varying T_s and the advective timescale, τ_{adv}, is varied by varying U. The control simulation CTL has no small-scale terrain. .

Simulation	l_{sst} (km)	U (ms^{-1})	T_s (K)
CTL	-	10	285
Sst10km	10	10	285
Sst4km	4	10	285
Sst5km	5	10	285
Sst8km	8	10	285
Sst12km	12	10	285
Sst15km	15	10	285
Sst10km_T272.5	10	10	272.5
Sst10km_T275	10	10	275
Sst10km_T276	10	10	276
Sst10km_T277.5	10	10	277.5
Sst10km_T280	10	10	280
Sst10km_T282.5	10	10	282.5
Sst10km_T287.5	10	10	287.5
Sst10km_T290	10	10	290
Sst10km_T292.5	10	10	292.5
Sst10km_U5	10	5	285
Sst10km_U12.5	10	12.5	285
Sst10km_U15	10	15	285
Sst5km_T275	5	10	275
Sst5km_T277.5	5	10	277.5
Sst5km_T280	5	10	280
Sst5km_290	5	10	290

Table 2.1. *Summary of WRF simulations population*

2.3 Dynamical interpretation: linear stability analysis

Simulation CTL shows weak and relatively disorganized banded structures with a spacing between them of the order of the minimum wavelength that can be represented by the model horizontal resolution (Fig 2.2a),consistent with the inviscid linear model in the absence of small-scale terrain. Here, the small-scale disturbances required for convective triggering should be introduced either by physical mechanisms (e.g. adjustment of the initial profiles to the large-scale terrain), or nonphysical numerical errors. This is not a particularly relevant case for the atmosphere where small-scale roughness is always present at the surface, triggering lee waves that will play a dominant effect in embedded convection as discussed above. This fact becomes clear by comparison of CTL with simulations that have small-scale terrain, the latter showing intense and well organized convective rain bands aligned parallel to the mean wind (Fig. 2.2b,c,d), with significant precipitation enhancement: total domain precipitation can be more than doubled and maximum local rainfall intensity can increase more than 17 times, depending on l_{sst} (Table 2.2). These results are qualitatively similar to Kirshbaum et al. (2007a) linear model predictions. However, for a single scale of terrain variability the analytical model predicts a band spacing equal to l_{sst}, whereas our simulations show banding with $l_{sst}/2$ spacing. The reason is that while the linear model assumes that the upstream cloud edge position is fixed, the numerical simulations show that bands can form at different x positions, generated by terrain features that are 90º out of phase, a nonlinear effect not captured by the linear model.

Although the idealized analytical models give interesting insights on governing parameters and physical mechanisms, they fail to predict the correct pattern except in particular idealized cases, and they are unable to produce realistic quantitative results. Besides different cloud edge positions, the linear models are also unable to capture other nonlinear effects observed in the numerical simulations such as decay of convective structures, different intensities between bands in the same simulation, and band narrowing (see Kirshbaum et al., 2007a). Furthermore, the linear models should only be valid (at most) in the initial stage of convective growth, while disturbance amplitudes are small. Thus, nonlinear models are necessary to improve our knowledge of embedded convection, and for quantitative predictions. In the next section, one particularly promising nonlinear model based on cascade scaling models from turbulence is introduced.

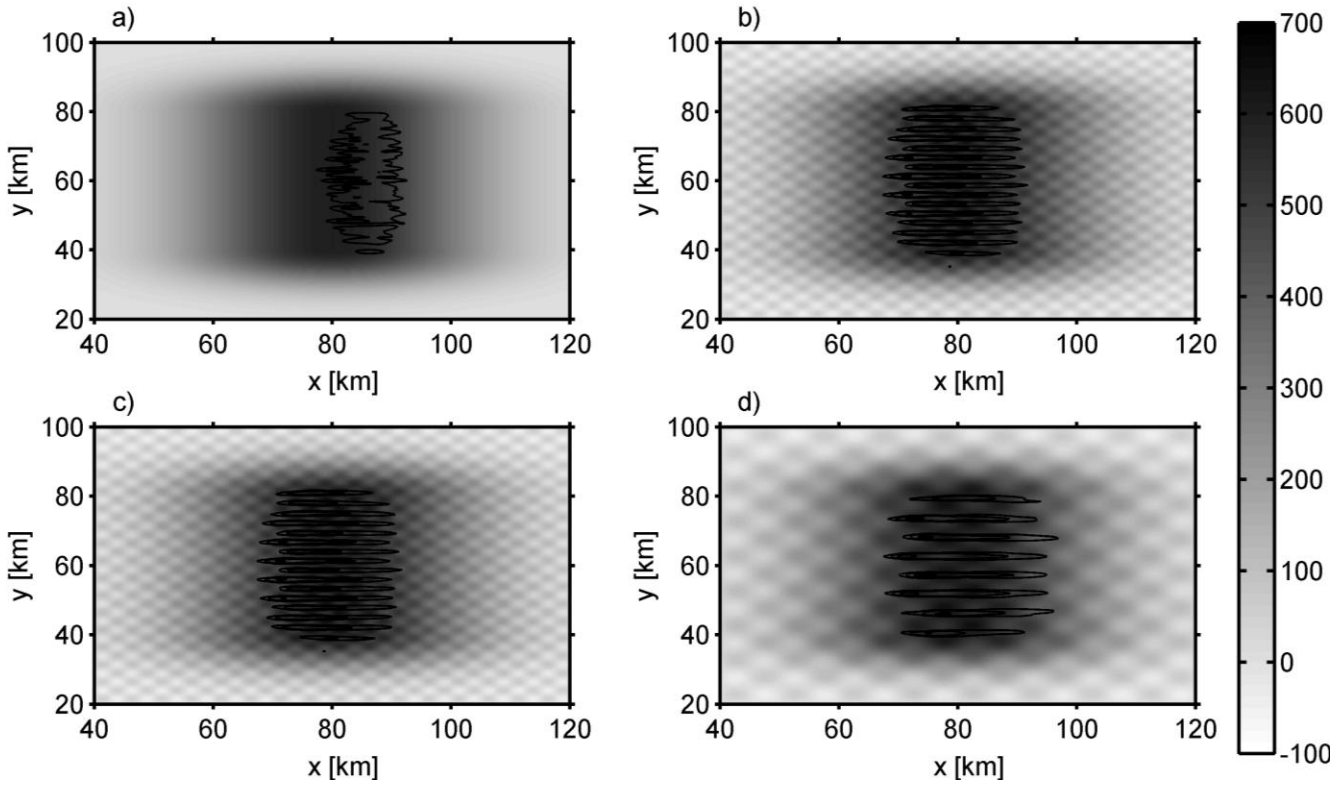

Figure 2.2. *Horizontal maps of P_{ac}^{5h} (black isolines at values 1, 10 and 50 mm/5h), and terrain height (gray scale, in m) for simulations a) CTL, b) Sst5km, c) Sst10km and d) Sst15km.*

Simulation	**Local maximum P_{ac}^{5h} (mm/5h)**	**Total domain P_{ac}^{5h} (mm/5h) x 10^4**
CTL	11.2	3.79
Sst4km	33.3	6.97
Sst5km	64.0	7.38
Sst8km	154.2	8.75
Sst10km	153.3	9.70
Sst12km	192.1	9.29
Sst15km	170.7	8.38

Table 2.2. *Local maximum and domain total of P_{ac}^{5h} field in simulations with different small-scale terrain wavelengths.*

2.4 Empirical scaling analysis

2.4.1 The Universal Multifractal model

The existence of scale invariance in atmospheric fields is often investigated by analyzing their statistical moments, which are expected to obey the generic multiscaling relation:

$$\langle {\varphi_\lambda}^q \rangle = \lambda^{K(q)} \tag{2.4}$$

where $\langle \cdot \rangle$ represents the statistical average, q is the moment order generalized to any positive real number, $\lambda = \frac{L_0}{l}$ is the scale ratio, L_0 being the outer scale of the cascade (the largest scale of variability) and l the scale of the observation, or simulation. φ_λ is a quantity that is on average conserved from scale to scale in a similar way to what happens in turbulence cascade models. The turbulent flux is non-dimensionalized and normalized, such that $\langle \varphi_\lambda \rangle = 1$. In general geophysical fields are multifractals, i.e. the exponent K is a function of q, and thus an infinity of exponents are required to characterize the scaling behavior. However, one can use the UM framework to model the variation of K with q for a conserved process, reducing the problem to two parameters (α and C_1; Schertzer and Lovejoy 1987):

$$K(q) = \begin{cases} \frac{C_1}{\alpha - 1}(q^\alpha - q), & a \neq 1 \\ C_1 \, \mathrm{qlog}(q), & a = 1 \end{cases} \tag{2.5}$$

The Levy index, α, defined in the interval [0,2], indicates the degree of multifractality ($\alpha = 0$ for monofractals); and the co-dimension of the mean singularity, C_1, describes the sparseness or non-homogeneity of the mean of the process. The moment order must be positive ($q > 0$) in this framework.

There is no physical basis to assume that a general observable, f, (e.g. wind, temperature, rainfall, etc.) should be conserved on a scale by scale basis. In analogy with turbulence models, we may expect that observable fluctuations, $\Delta f(l)$, over a distance l, are related to a general turbulent conserved flux, φ_l, by:

$$\Delta f(l) = \varphi_l^\eta l^H \tag{2.6}$$

A third Universal Multifractal parameter is introduced in Eq. 2.6: the Hurst exponent (or nonconservation parameter), H. In a conservative process $\langle \varphi_\lambda \rangle = cte$, and thus $H = 0$ and $K(1) = 0$. But in the general case, the mean has a dependence on scale, $< \Delta f > \sim l^H$. The other exponent, η, depends on the particular field being analyzed. Note that Eq. 2.6 is a generalization of the classical laws of turbulence. For example, in the Kolmogorov (1941) law for turbulent velocity fluctuations: $\Delta v(l) = \varepsilon^{1/3} l^{1/3}$, we have that $H = 1/3$, $\eta = 1/3$ and $\varphi_l = \varepsilon$. In this case the observable (turbulent wind field, v) is not the direct result of a multiplicative cascade, that role being reserved for the (cascade conserved) energy flux, ε. The cascade conserved flux can have more complex forms that include nonlinear interactions of different fluxes, e.g. the Corsin-Obukhov law for passive scalar advection (Obukhov, 1949; Corsin, 1951): $\Delta \rho(l) = \xi^{1/3} l^{1/3}$, where $\xi = \varphi_l = \chi^{3/2} \varepsilon^{-1/2}$, χ being the scalar variance flux. In these classic turbulence cases, the laws relating the observable fluctuations and conserved turbulent fluxes can be obtained from the governing dynamical equations, assuming isotropy, and via dimensional analysis. For rain and cloud processes (which generally cannot be assumed to behave as passive scalars), the values of η and H are unknown, and so is the physical nature of the conserved flux. However it is still possible to perform scaling analysis. We start by taking the simplifying assumption η=1, as usually done in similar previous works, noticing that if φ_λ is a pure multiplicative cascade then that is also true for φ_λ^η, although with different C_1 values (e.g. Tessier et al., 1993; Stolle et al., 2009). The next step is to remove the influence of the l^H term. One method used for this purpose is to rely on the absolute value of a finite difference gradient to compute the fluctuations at the highest resolution available, $\Delta f(l_{res})$ (see e.g. Lavallée et al., 1993; Tessier et al., 1993):

$$\varphi_\lambda{}^\eta = \Delta f(l_{res}) = \left\{ [f(x + l_{res}, y) - f(x, y)]^2 + [f(x, y + l_{res}) - f(x, y)]^2 \right\}^{1/2} \quad (2.7)$$

The flux estimates given by Eq. 2.7 are systematically degraded to lower resolutions (lower values of λ) by spatial averaging. The Double Trace Moment (DTM) technique (e.g. Lavallée et al, 1993) can be used subsequently to estimate α and C_1. Notice that the values of the UM parameters estimated from data generated by numerical models are not the same as the ones obtained from observations due to cascade cutoff by model resolution and model domain, but it is possible to convert between them (Stolle et al., 2009). Nevertheless, incorrect representation of physical processes in the models cannot be corrected. In the present work we aim only to

investigate the variation of the UM parameters in numerical simulations with similar setup, so no conversion is required.

Spectral analysis can also be used to investigate the behavior of a field over a wide range of scales. The spatial Fourier power spectrum, $E(k_x, k_y)$, is computed by multiplying the 2-dimensional fast Fourier transform of a field by its complex conjugate, where k_x and k_y are the wavenumber components. The power spectrum is then averaged angularly about $(k_x, k_y) = (0,0)$ to yield what is usually called isotropic power spectrum $E(k)$, with $k = \sqrt{{k_x}^2 + {k_y}^2}$. Spatial scaling invariance manifests itself as log-log linearity of the power spectrum in space:

$$E(k) \sim k^{-\beta-1} \tag{2.8}$$

Where β is the spectral exponent and the addition of -1 in the exponent is required due radial averaging is phase space (e.g. Turcotte, 1992; Lovejoy et al., 2008b). Least square regression is used to estimate β from a log-log plot of $E(k)$ against k.

The spectral exponent is related to the UM parameters by (Tessier et al., 1993):

$$\beta = 1 + 2H - K(2) \tag{2.9}$$

Finally we estimate H from the slope of the log-log plot of the first order structure function against the lag, as described by Harris et al. (2001), Nykanen (2008) and Lovejoy et al. (2008a,b).

2.4.2 Scaling in simulated 2D fields

The empirical scaling analysis described above is applied to surface accumulated precipitation spatial fields over 5 hour simulations, P_{ac}^{5h}. Here the constant value $80\ km$ (domain length) was used for the cascade outer scale, L_0. Changing the chosen value of L_0 has no effect on the estimated value of the slope of the fitted lines, i.e. on $K(q)$ and respective UM parameter estimation. Fig. 2.3a-c shows log-log plots of M_q against λ for P_{ac}^{5h} fields for three different simulations. The lines are only fitted to the range of scales that are well resolved by the model, i.e. larger than $5\Delta x (= 1.25\ km)$ and smaller than about $L_0/4 (= 20\ km)$. For $q \leq 2$ the linear fits are good implying that statistical scale invariance predicted by Eq. 2.4 is a good

representation, and that there are no characteristic scales or scale breaks for the considered ranges of q and λ (from ~1 to ~ 20 km). This range of q is similar to the ones found in literature for similar analysis (e.g Douglas and Barros, 2003; Lovejoy et al., 2008a,b; Nykanen, 2008; de Lima and de Lima, 2009). Some simulations show ersistent deviations from linear behavior at particular scales, but the relation between these scales and l_{sst} varies between simulations, suggesting that the small-scale terrain wavelength is not (statistically) a characteristic scale in the rain fields. The same spatial scaling analysis was repeated for the P_{ac}^{5h} fields resulting from all simulations in Table 2.1, all of them showing the same robust scaling behavior (linear relations).

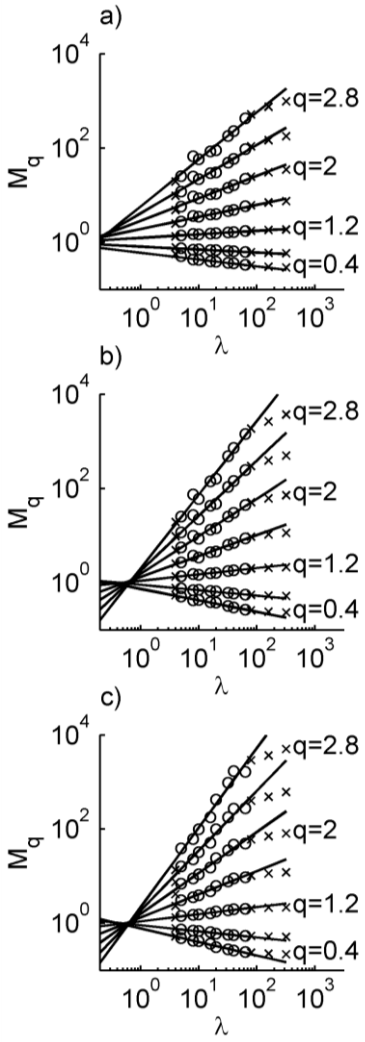

Figure 2.3. *Relationship between M_q and λ for different values of q. M_q is computed from P_{ac}^{5h} from simulation a) Sst5km, b) Sst10km, c) Sst15km. The scales considered on the analysis are marked by 'o' while 'x' marks the ones not considered. The plots are on a log-log scale.*

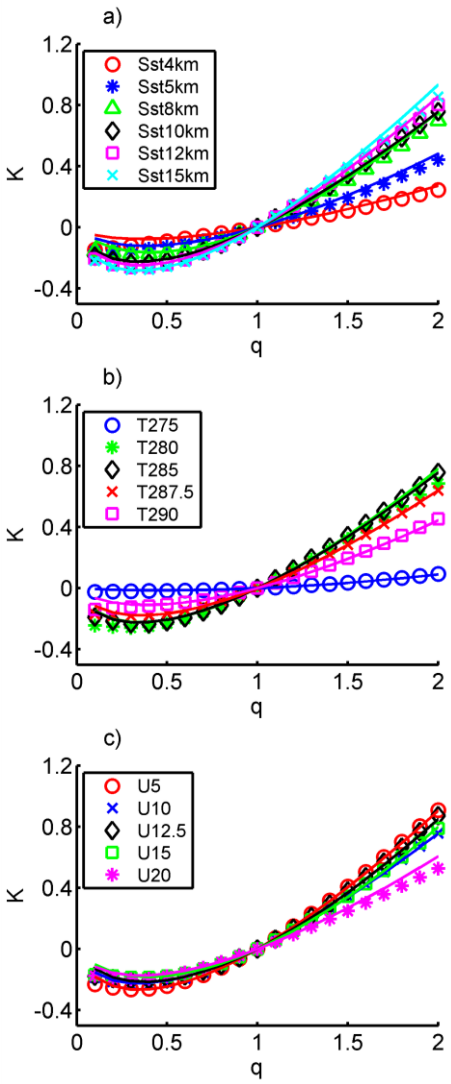

Figure 2.4. *The scaling exponent function, $K(q)$ for a) varying l_{sst}, b) varying T_s with $l_{sst} = 10\ km$ and c) varying U with $l_{sst} = 10\ km$. The empirical estimated $K(q)$ is showed with markers and the UM model fit is represented by full line.*

The scaling exponent function, $K(q)$, and respective UM parameters can be used to quantify the multifractal behavior. Fig. 2.4 shows that for q<2 there is a very robust match between empirically estimated scaling exponent function, $K(q)$, (i.e. slopes of the fitted lines in log-log plots of M_q against λ) from P_{ac}^{5h} fields for the different simulations and the UM model curves (solid lines), computed from Eq. 2.5 with the UM parameters obtained from DTM technique, which is consistent with the literature (e.g. Nykanen, 2008; Lovejoy et al. (2008a), Stolle, 2009, among others). It is also important to notice the variation of $K(q)$ with varying simulation

attributes (l_{sst}, T_s and τ_{adv}). This variation is quantified in Fig. 2.5 (black line) using C_1 and α, which display a complex nonlinear variation with simulation attributes. A particularly remarkable feature is the abrupt transition in both UM parameters for T_s between 275K and 285K. The transition has a physical correspondence when interpreted against the spatial rainfall patterns (red lines in Fig. 2.6), capturing the evolution from terrain-following (more stratiform) and less intense rainfall fields in the colder simulation cases to well organized and intense bands for simulations at intermediate temperatures. For warmer simulations the rainfall pattern changes again to more intense but less organized (more cellular) convective features (Fig. 2.6d), and the UM parameters also show variation (Fig. 2.5c and d). These differences in convective dynamics have important effects in rainfall intensities and patterns leading to high localized rainfall accumulation values (Table 2.3, and see also Kirhsbaum and Durran, 2005b and Fuhrer and Schär, 2007).

The same analysis was performed on instantaneous horizontal cross sections of cloud water mixing ratio, q_c, at two different levels (the height of q_c maximum intensity, $z_{q_c max}$ and z=1100 m) after 3, 4 and 5 hours of simulation, corresponding to the mature stage when the convective structures are fully grown. Fig. 2.7 illustrates the robust scaling of moments of q_c fields at $z_{q_c max}$ for three different simulations. The same behavior is found for cloud fields in all simulations in Table 2.1, at all the analyzed times and heights. The UM parameters computed from q_c also display complex nonlinear variation with simulation properties (red line at $z_{q_c max}$ and blue at z=1100 m in Fig. 2.5). In particular the transition between colder and warmer cases is again clear. Both α and C_1 show similar values at the different times, due to the quasi-stationary state of the convective structures that is attained in these simulations. Comparison of the scaling parameters computed from q_c fields at different vertical levels shows vertical variation of both UM parameters, although the shape of the curve is largely preserved. Notice that the $z_{q_c max}$ level varies between simulations and with time, and it can sometimes capture different structures and cause significant variations of the parameters. This explains some values that seem to fall outside the curves: for example the value of C_1 for Sst15km at 0500h computed from q_c at $z_{q_c max}$ is quite different from the one at 0400h, which is easily understood by examining Fig. 2.8: in Sst10km the $z_{q_c max}$ level crosses the core of the cloud band, the same happening for Sst15km at 0400h, while at Sst15km at 0500h it is actually crossing a region of instabilities that has formed

on the top region of the band, resulting in a different horizontal pattern and associated scaling parameters. The large variation in C_1 for the largest advective timescale τ_{adv} at different times has a similar explanation.

Simulation	**Local maximum of P_{ac}^{5h} (mm/5h)**	**Total domain P_{ac}^{5h} (mm/5h) x 10^4**	**Local maximum of q_c (g/kg)**	**Local maximum of q_i (g/kg)**
Sst10km_T272.5_WR	0.00	0.00	0.53	-
Sst10km_T272.5	1.90	4.79	0.24	0.11
Sst10km_T275	1.75	3.63	0.27	0.13
Sst10km_T276	1.80	3.05	0.33	0.13
Sst10km_T277.5	0.33	0.07	0.71	0.00
Sst10km_T280	23.77	1.20	1.10	0.00
Sst10km_T282.5	83.72	2.83	1.34	0.00
Sst10km	153.28	4.68	1.49	0.00
Sst10km_T287.5	143.06	9.20	1.57	0.83
Sst10km_T290	214.45	31.59	1.79	2.13
Sst10km_T292.5	258.87	76.43	2.18	5.25

Table 2.3. *Local maximum of P_{ac}^{5h}, q_c and q_i fields and domain total P_{ac}^{5h} for simulations with different temperature profiles.*

The cumulative rainfall field analyzed here is viewed as representative of the entire simulated convective rain event. It is important to stress that a time integrated quantity will depend on the evolution of the system during the integration interval and the specific quantitative values of scaling parameters should change during this period due to the transient nature of the interactions among various physical processes. Presently, at this stage of the research, the analysis is focused on the spatial properties of the accumulated precipitation fields for a specific time of integration in a manner consistent with standard rainfall observations that consist of rainfall accumulations

over a measurement time-scale. Downscaling is critical to obtain robust spatial distributions of rainfall for use in hydrological studies and applications.

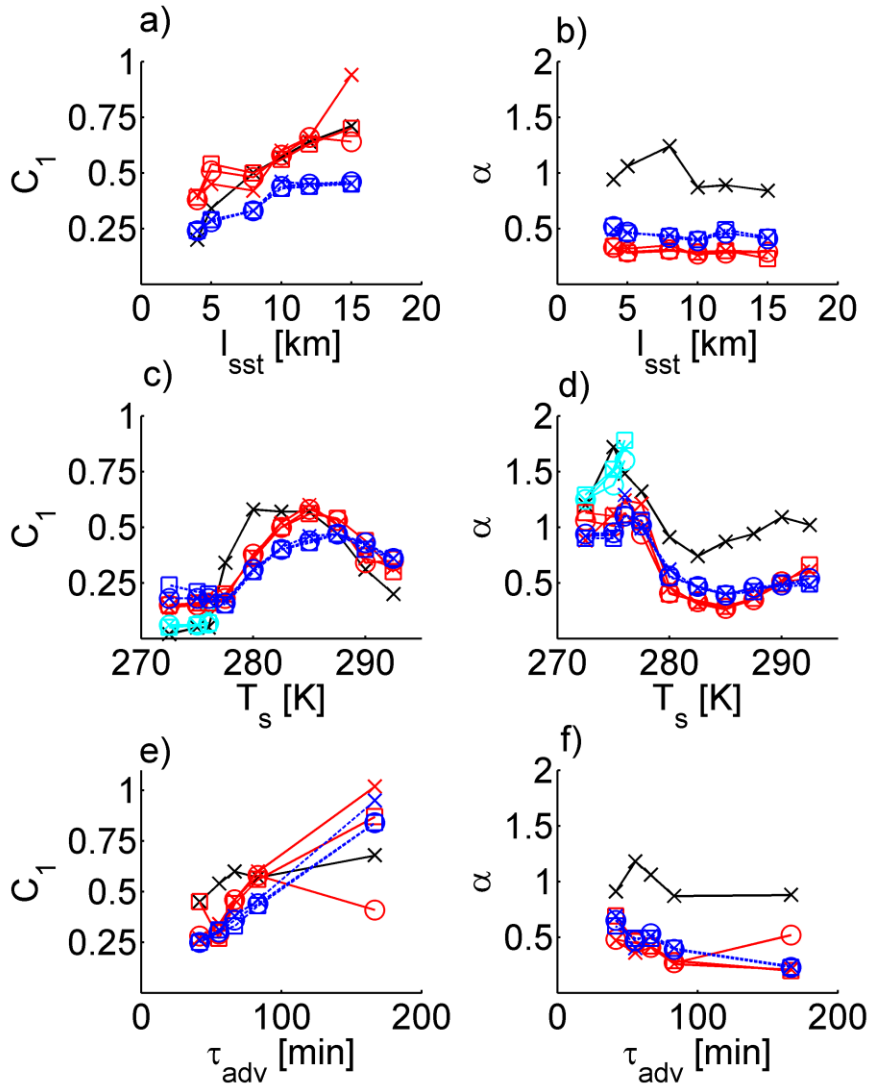

Figure 2.5. *Relationship between UM parameters (C_1 and α) and: a, b) l_{sst}; c, d) T_s ; and e, f) τ_{adv}. Black lines represent values computed from P_{ac}^{5h}, red and blue lines are computed from q_c at $z_{q_c max}$ and z=1100 m respectively. Light blue markers are computed from ice mixing ratio fields at the level of their maximum intensity. 'x', 'o', '□' markers represent simulation times 0500h, 0400h and 0300h respectively.*

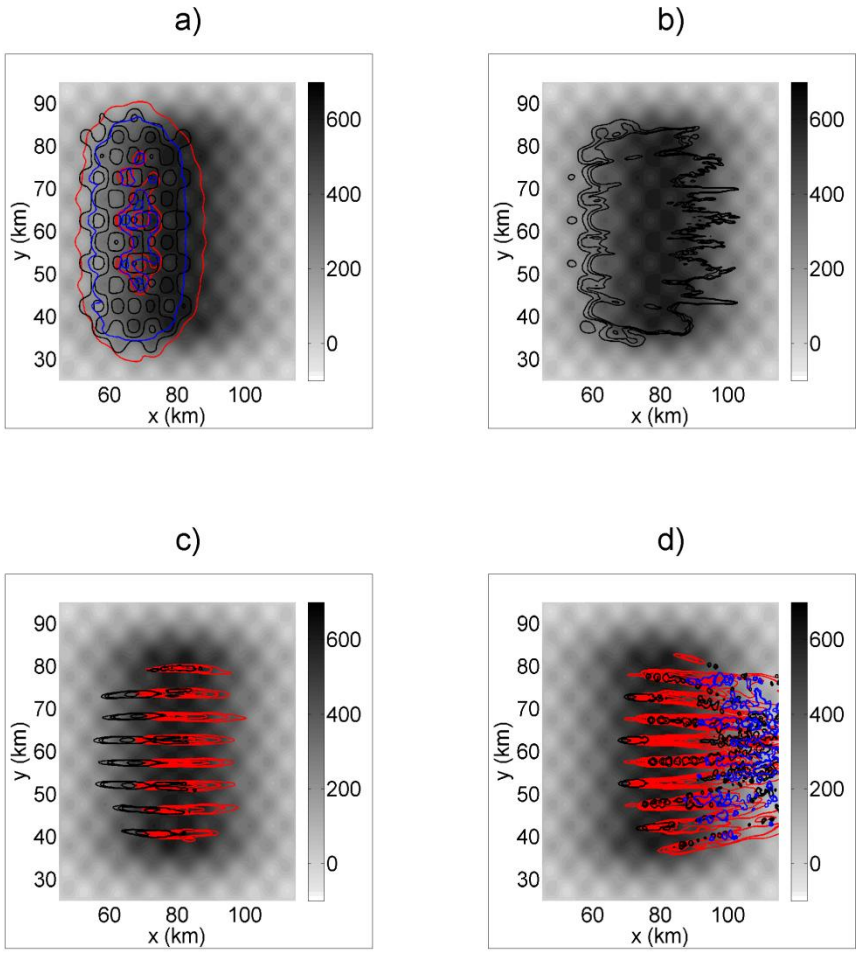

Figure 2.6. *Horizontal cross sections of P_{ac}^{5h} (red isolines), q_c fields at $z_{q_c max}$ at 0400h (black isolines) and q_i at the level of its maximum intensity at 0400h (blue isolines) from simulations a) Sst10km_T272.5, b) Sst10km_T277.5, c) Sst10km and d) Sst10km_T290. Grayscale represents topographic elevation (in meters)*

2.4.3 Scaling in cloud simulated fields – 3D analysis

The previous section showed a vertical variation of 2-dimensional horizontal UM parameters. One possibility to avoid the complex problem of knowing the vertical variation of horizontal scaling exponents is to consider each horizontal level (different height) as a realization of the field and average over these several realizations, obtaining a single set of horizontal UM parameters representative of the horizontal scaling for the entire volume. The moments averaged over several vertical levels show improved linear fits as compared to the 2-dimensional cases for all simulations (Fig. 2.9), and in particularly for higher order moments, which should be

explained by the larger data sample size considered. Like in the 2-dimensional case, some persistent deviations are identifiable but they have smaller amplitudes, and the particular scales for each simulation between 2- and 3-dimensional cases are different, providing support to the notion of absence of characteristic scales. The presence of scaling behavior for the entire volume implies that concurrent spatial structures (e.g. band core region, instabilities at the top of the bands, clouds that form downstream of the large scale orography, among others, Fig. 2.8) fall in the same average horizontal scaling regime. The scaling behavior in the vertical direction is not investigated here due to data limitations associated with the limited number of vertical levels in the model (see section 2.2) together with the fact that we are looking at instantaneous realizations of fields rather than ensemble average statistics. But in other cases it could be investigated using a different set of UM parameters to describe anisotropy between horizontal and vertical directions (see e.g. Lovejoy et al., 1987, Lazarev et al., 1994; Radkevich et al., 2007).

As in the 2-dimensional case, the UM parameters vary with mean atmospheric and terrain properties (Fig. 2.10). Fig. 2.10a shows C_1 decreasing with l_{sst} while Fig. 2.10b shows there is little variation of α with l_{sst}. Figs. 2.10c and d show the abrupt transitions in both scaling parameters with changes in T_s, further providing support for this result. Recall that in these idealized simulations the temperature profiles and cloud layer stability are determined by T_s. However, in more realistic profiles this will not generally be true. Linear stability analysis suggests that a good alternative is to characterize the atmospheric environment using a (spatial) average ${N_m}^2$ value. This average is computed at each time instant and only from points that exceed a fixed (arbitrary) q_c threshold (e.g. 0.01 g/kg) as it is defined only in saturated regions. Figures 2.11a and 2.11b show that the abrupt transition corresponds to the transition between the stable (${N_m}^2 > 0$) and unstable (${N_m}^2 < 0$) cases. For larger negative values, ${N_m}^2 < -2.5 \times 10^{-6} s^{-2}$ there is a break in variability of the UM parameters for small changes in ${N_m}^2$, particularly clear in C_1. This behavior poses an intriguing question as to the character of the underlying physics and of this flow transition for highly unstable flows, not unlike the transition to high Reynolds numbers in the case of fully-develepod turbulence turbulence . The fields with the strongest instability values are not necessarily the warmer ones as defined by the initial conditions, as the average ${N_m}^2$ value can be significantly altered by the release of latent heating or due to the presence of downstream stable clouds and other features.

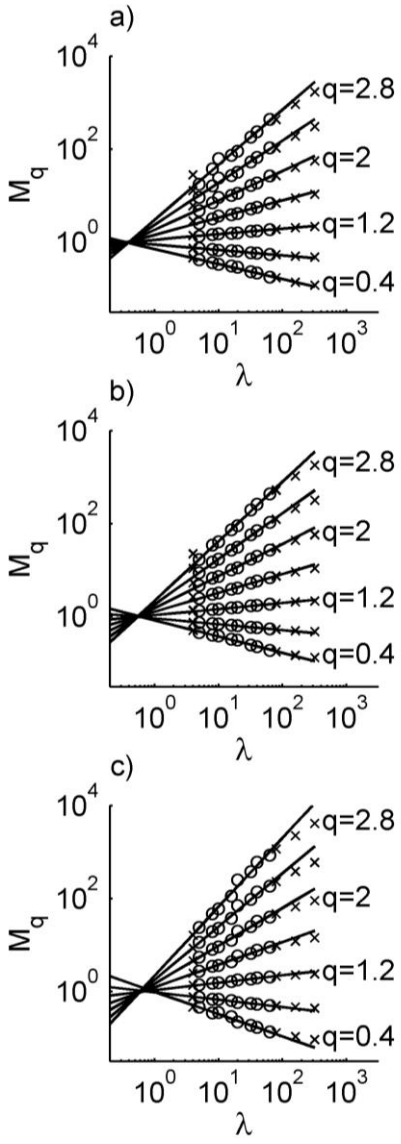

Figure 2.7. *Relationship between M_q and λ for different values of q. M_q is computed from $q_c$at $z_{q_c max}$ at 0400h for simulation a) Sst5km, b) Sst10km and c) Sst15km. The scales considered on the analysis are marked by 'o' while 'x' marks the ones not considered. The plots are on a log-log scale.*

To capture the effect of space-time co-localization of moist instability release and moist processes, $N_m{}^2$ can be multiplied by a measure of the cloud fraction, cf, defined here by the ratio of number of grid points that exceed the chosen q_c threshold to the total number of points. This transformation gives a measure of the overall realized moist instability at a given point in time, and provides a physically-based framework to arrange the simulations in the order of

colder (more stable, higher $cf \times {N_m}^2$) to warmer profiles (more unstable, lower $cf \times {N_m}^2$), consequently yielding more robust relationships (Figs. 2.11c and d). Indeed, this result holds for different values of the threshold, and the transition between stable and unstable cases becomes clearer in these plots. The stable region shows nearly constant UM parameters, with lower values of C_1 associated with a more space filling mean component in stratiform clouds as compared to more localized convective structures; the region of low realized instability corresponds to simulations that produce quasi-stationary rainbands, in agreement with the numerical experiments of Kirshbaum and Durran (2005a) who found that marginal potential instability and moderate wind speeds were the most favorable atmospheric conditions for convective bands to develop. This region displays complex variation of the scaling parameters that might be associated with the presence of different regimes due to competition between buoyancy and mechanical generation/dissipation of turbulence. Further investigation, with a larger population of simulations in this specific region of instability values, is necessary for further confirmation of this finding. In particular, the role of wind shear (usually understood as a mechanical turbulence generator) in band generation is not clear and requires more detailed analysis. The bands form in the absence of any basic-state vertical shear (as it is seen in our simulation and also in Kirshbaum and Durran, 2005a; and Kirhsbaum et al., 2007b), although wind shear will dynamically develop in these simulations eventually due, for example, to adjustment to terrain or formation of localized convective circulations. Kirshbaum and Durran (2005a) also found that is some cases, wind shear can actually suppress rainbands. Figs. 2.11c and 2.11d also suggest that for higher instability conditions, when free convection dominates, and corresponding to the more cellular and disorganized patterns, the parameter variation becomes less complex.

The quantity $cf \times {N_m}^2$ is transient, depending on the dynamical evolution of the system. In particular, besides varying with upstream temperature profile, it also varies with τ_{adv} and l_{sst}. Thus we investigate its potential utility as a single predictor for the UM parameters for all the simulated q_c fields analyzed here. Figures 2.11g and 2.11h show the UM parameters for all analyzed simulations. For α, all the points seem to fall into a single curve, suggesting $cf \times {N_m}^2$ might be used potentially as a single predictor. However C_1 shows variability with l_{sst} (green and pink markers) and τ_{adv} (red markers), particularly in the region of low instability (stable cases). Also the pink curves in Figs. 2.11c, 2.11d, and 2.11g and 2.11h show that, for the same

initial temperature profiles but l_{sst}=5 km instead of 10 km, different values of C_1 are obtained. Thus $cf \times {N_m}^2$ alone can't be used as a single predictor for both UM parameters, and variation with l_{sst} and τ_{adv} has to be considered separately.

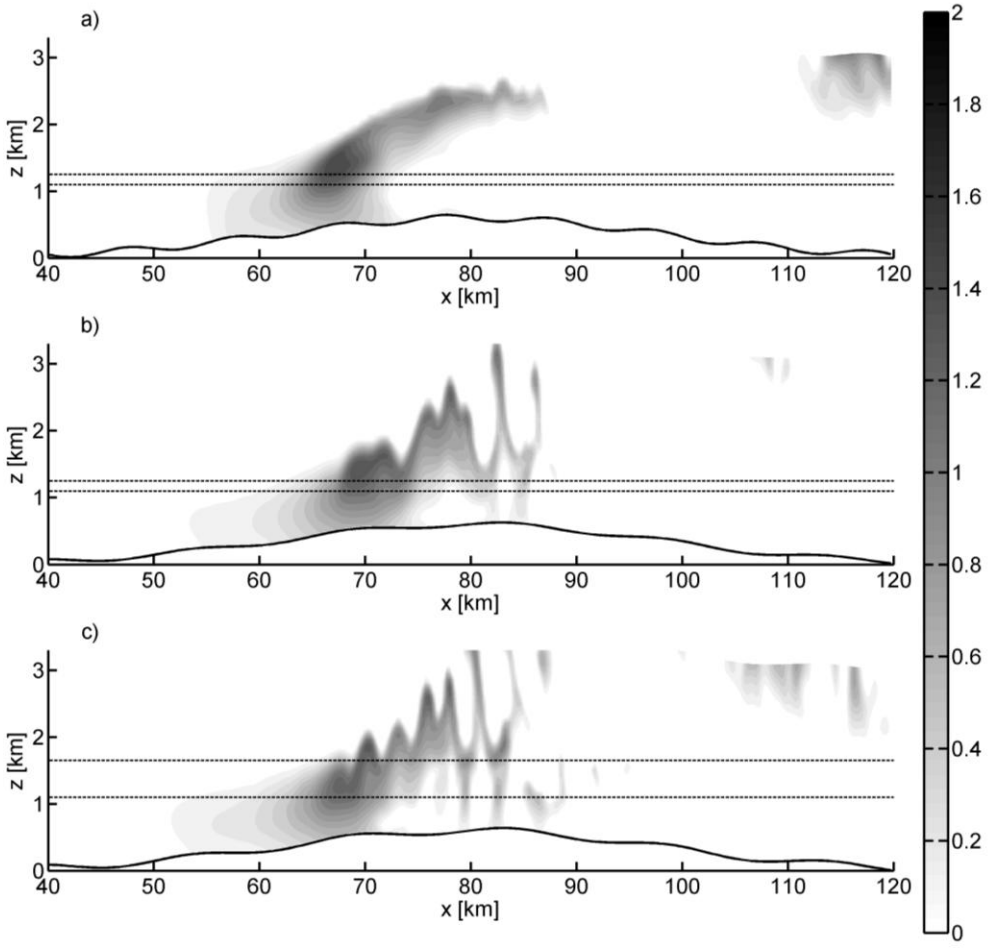

Figure 2.8. *Cross sections (xz) of q_c at the y position of its maximum intensity for simulations a) Sst10km at 0400h, b) Sst15km at 0400h and c) Sst15km at 0500h. The solid black line represents topography. The upper and lower black dashed lines represent the levels $z_{q_c max}$ and $z =$ 1100 m respectively.*

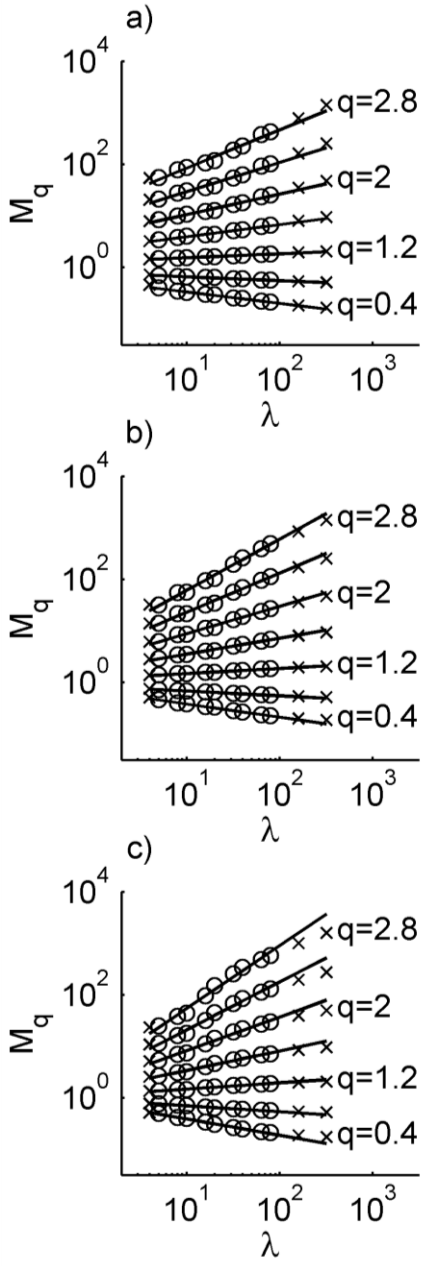

Figure 2.9. *Relationship between M_q and λ for different values of q. M_q is computed from q_c at 0400h for simulations a) Sst5km, b) Sst10km, c) Sst15km. The scales considered on the analysis are marked by 'o' while 'x' marks the ones not considered. The plots are on log-log scale.*

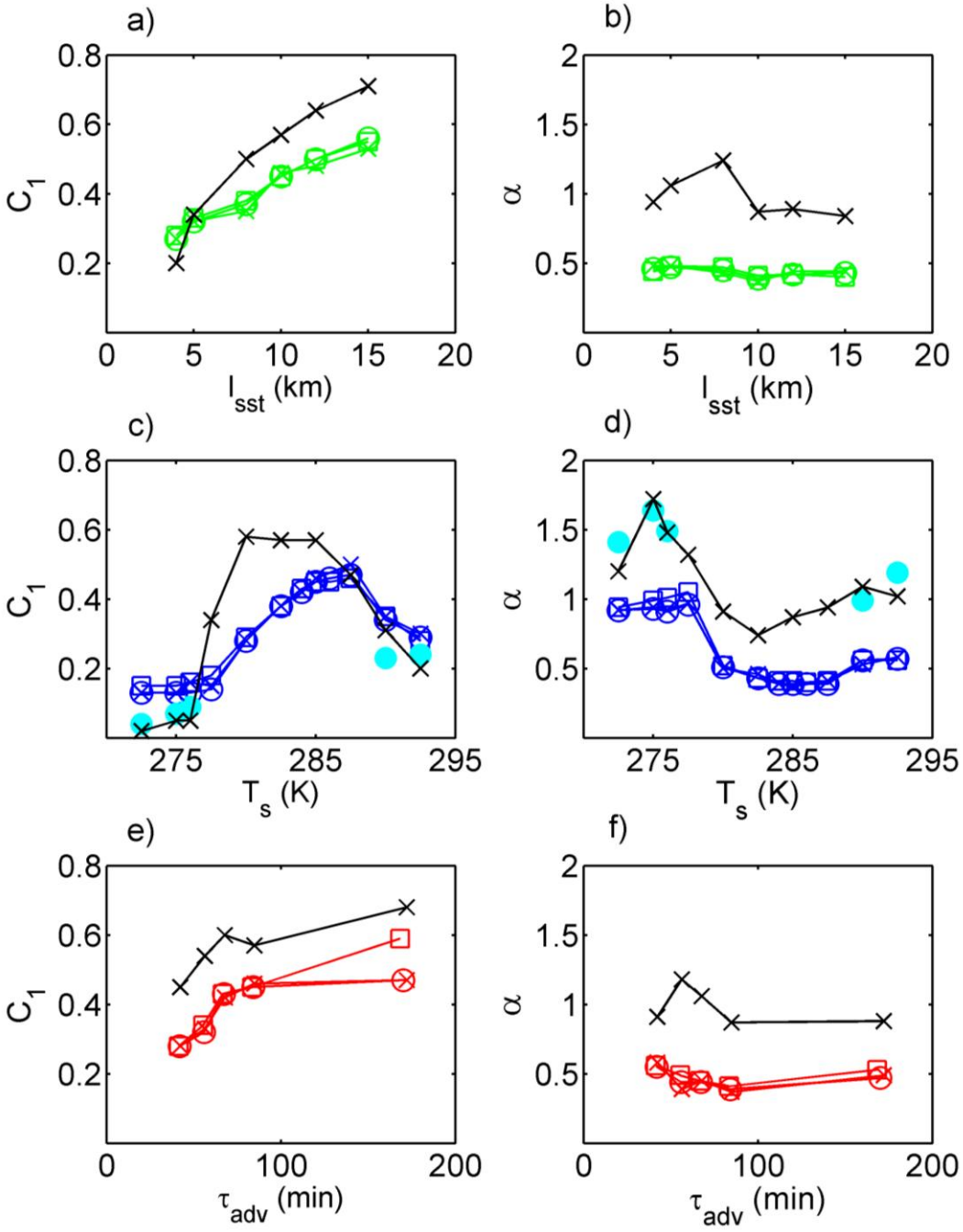

Figure 2.10. *C_1 and α computed from 3-dimensional averages of q_c horizontal fluctuations against: a, b) l_{sst}, c, d) T_s and e, f) τ_{adv}. Black lines represent values computed from P_{ac}^{5h}. Green, blue and red lines are computed from q_c. The light blue markers lines are computed from q_i. 'x', 'o' and '□' markers represent simulation times 0500h, 0400h and 0300h, respectively.*

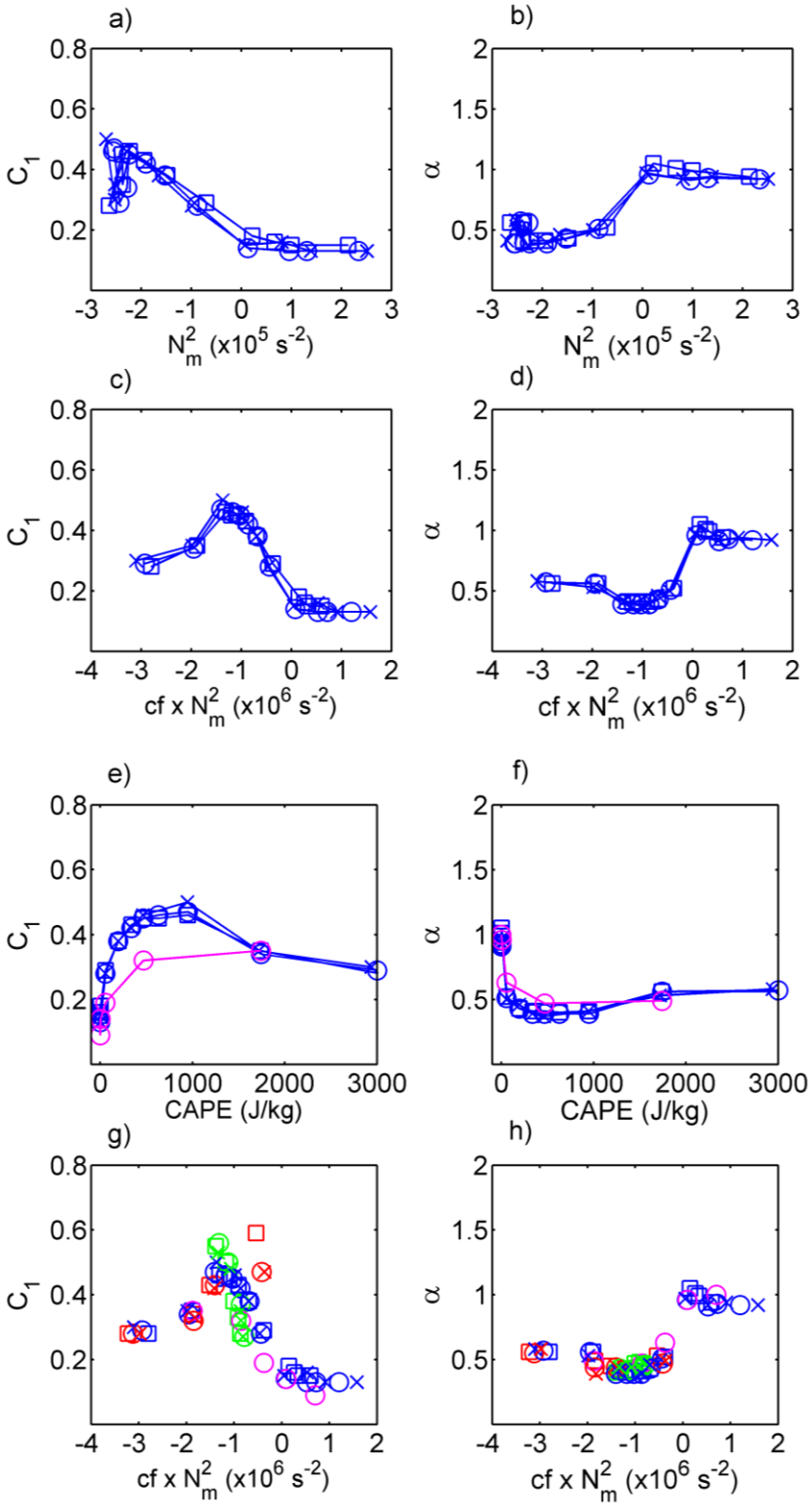

Figure 2.11. *C_1 and α computed from 3-dimensional averages of q_c horizontal fluctuations against: a, b) ${N_m}^2$; c, d) $cf \times {N_m}^2$; and e, f) CAPE. Blue lines and markers are computed from*

simulations with varying T_s and l_{sst}= 10 km, pink from simulations with varying T_s and l_{sst}= 5 km, red for varying τ_{adv} and green for varying l_{sst}. Plots g, h) show C_1 and α against $cf \times {N_m}^2$ for all simulations. Black markers in plots g) and h) represent simulation Sst10km (i.e. the base case). 'x', 'o' and '□' markers represent simulation times 0500h, 0400h and 0300h respectively.

As mentioned earlier, Perica and Foufoula-Georgiou (1996) found a linear dependency of statistical scaling parameters on another atmospheric stability measure, the Convective Available Potential Energy (CAPE), for a small number of rainfall fields of selected convective storms over relatively flat topography. This result was tested in our simulated fields which have a wider range of $CAPE$ values, and a more complex nonlinear relation was obtained (Fig. 2.11 e and f). Compared to ${N_m}^2$, the use of $CAPE$ has the disadvantage that the stable range of the profiles is ambiguous ($CAPE = 0$ for all stable cases), which presents a problem unless UM parameters were shown to be constant for all stable cases. Nevertheless, note that the unstable/stable transition of the parameters is still clear as $CAPE$ goes to zero, as well as the complex nonlinear behavior for the small magnitude instability values - the banded cases - and again less complex behavior for higher magnitude instability values - cellular disorganized cases. This is consistent with Kirshbaum and Durran (2005b) who proposed that the distinction between more banded and cellular cases is related to enhanced susceptibility to free convection, with larger CAPE implying more cellular structures. They suggest that Convective INhibtion (CIN) could be an important parameter as well, but all our simulations have very small values of CIN and are not suitable for such analysis.

2.4.4 Relations between different scaling fields

In both 2- and 3-dimensional analysis, UM parameters computed from P_{ac}^{5h} and q_c show clear relations for certain ranges of simulation properties, either in the shape of the variation curve in Figs. 2.5a,c,d and Figs. 2.10ac,d,e, or for the exact values of the parameter, as can be seen for example in Fig. 5a for C_1 computed from q_c at $z_{q_c max}$ for $l_{sst} \geq 8$ km and C_1 computed from z=1100 m for smaller l_{sst} (also in Fig. 2.5c, see the C_1 computed from q_c at $z_{q_c max}$ for $T_s \geq 285\ K$, and in Fig. 2.11c for $T_s \geq 287.5\ K$). For the 2-dimensional analysis these relationships depend on the chosen vertical level, sometimes best relating to the level of maximum intensity,

sometimes to some other level, which makes its use difficult in practical applications, further supporting the 3-dimensional analysis.

Figs. 2.5c,d and 2.10c,d show that for colder simulations ($T_s \leq 277.5\ K$) both UM parameters computed from P_{ac}^{5h} are very similar to the ones computed from ice phase (snow+ice+graupel) mixing ratio fields, q_i, which is particularly remarkable in the 3-dimensional analysis. The role of cold microphysics on precipitation processes is also clear in simulation Sst10km_T272.5_WR (which is exactly the same as in Sst10km_T272.5, except that the Kessler warm rain scheme is used in WRF and ice microphysics is turned off). The simulation with warm rain processes only produces a cloud pattern similar to the one including cold microphysics, but it yields zero P_{ac}^{5h} (Table 2.3). This result is strengthened by the fact that below $277.5\ K$ the values of precipitation intensity and q_i increase with decreasing temperature (Table 2.3). Finally, it is also apparent in Fig. 6a that for the colder case there is a clear relation between the P_{ac}^{5h} (red line) and q_i (blue line) patterns, while the q_c(black line) seems to be more closely related to the underlying topography (grey scale). If the temperature is slightly raised, both q_i and P_{ac}^{5h} go to zero (Fig. 2.6b and Table 2.3). If the temperature is raised further, well organized cloud bands form with a clearly associated P_{ac}^{5h} pattern and no ice phase (Fig. 2.6c). Besides varying ${N_m}^2$, changing T_s also changes the amounts of water in each phase and the vertical structure of the clouds, particularly the cloud depth (Fig. 2.12), which the linear theory also predicts as being an important parameter in embedded convection. For the warmer cases considered here, the cloud depth growths enough so that ice processes become important again (blue lines in Fig. 2.6d and Table 2.3), but the precipitation pattern now seems to be more related to q_c (Fig. 2.6d). In these warmer cases, the parameter C_1 from P_{ac}^{5h} seems to relate better to q_c while α seems to relate better to q_i (Fig. 2.10c,d). Overall, these results suggest that scaling of the simulated total precipitation fields is a complex function of the scaling of several other fields including water mixing ratio in the different phases, and probably also small-scale terrain spectra and τ_{adv}. That is, the scaling of the integral precipitation fields reflects the underlying governing physical processes, which change with time and space as weather systems evolve and propagate over complex terrain.

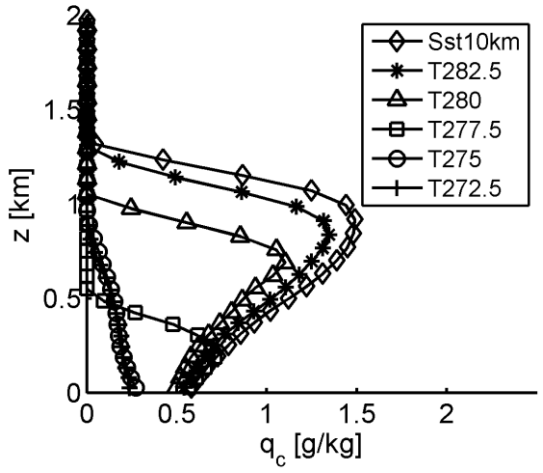

Figure 2.12. *Vertical profiles of q_c at the position of their maximum intensity at 0400h, for simulations with $l_{sst} = 10\ km$ and varying T_s.*

2.4.5 Spectral Analysis

The isotropic power spectra, described in Section 2.4.1, can also be used to investigate the spatial scaling of horizontal fields. Here we average the spectra of instantaneous q_c fields over several vertical levels, similar to what was done in Section 2.4.3 for moment scaling analysis. Figure 2.13 shows three examples of log-log power spectra (black lines) computed at simulation hour 0400: at the bottom for a colder stable case (Sst10km_T275), in the middle for an intermediate banded case (Sst10km), and at the top for a warmer more disorganized convective case (Sst10km_T292.5). Only the scales well resolved by the model are considered (and represented), assumed here to be larger than $5\Delta x$ (limited by model resolution). It is important to keep in mind that Fourier analysis has the implicit requirement (assumption) of an infinite domain, and clearly here, as in general in all applications of Fourier analysis to digital data, we are limited by the domain size of the grid, to which the analysis is quite sensitive. It was found that the scale range we considered above $L_0/4$ is too large based on the lack of symmetry of the domain, and the upper boundary of the range was reduced to a value $L_0/8$. Outside this range, we do not have enough information on the power spectrum of the field.

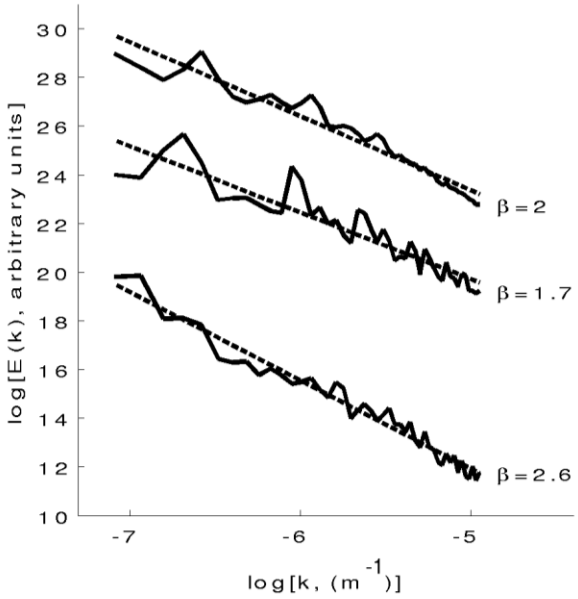

Figure 2.13. *Log-log plots of isotropic power spectra computed from horizontal q_c field at 0400h averaged over several vertical levels, from simulations: Sst10km_T292.5 (top), Sst10km (middle) and Sst10km_T275 (bottom). Only the range of scales between $5\Delta x$ and about $L_0/8$ is represented. The black dashed lines are least square fits to the spectra.*

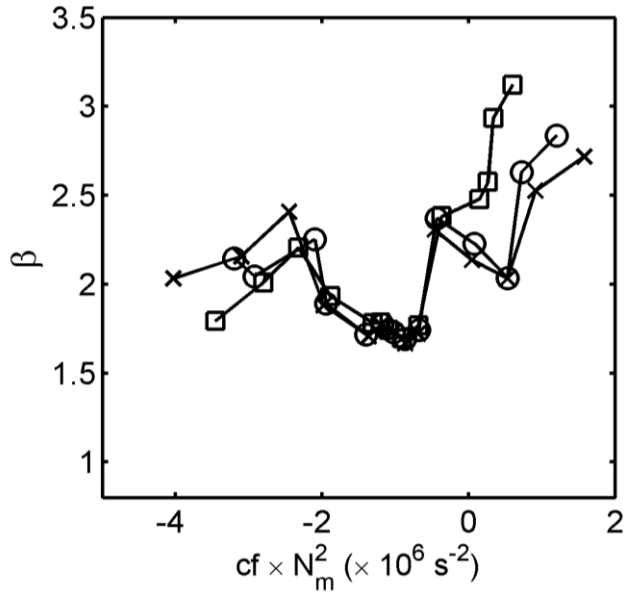

Figure 2.14. *Relationship between β (computed from horizontal q_c field averaged over several vertical levels) and $cf \times {N_m}^2$ $(\times 10^{-5} s^{-2})$. 'x', 'o', '□' markers represent simulation times 0500h, 0400h and 0300h respectively.*

The black dashed lines in Fig. 2.13 are least-square fits to the considered range of scales (wavenumbers) of the power spectrum. There is a clear mean linear trend (scaling) in the log-log power spectra, with R^2 values for the least-square fits always above 0.90. Peaks in the power spectra, particularly evident in the intermediate banded case spectrum (middle spectra in Fig. 2.13), are consistent with harmonics resulting from the banded pattern. This behavior is expected when analyzing single realizations of cloud fields (e.g. Harris et al., 2001), and more so for events over complex terrain when orographic forcing is dominant (e.g. see scaling analysis in Barros et al. 2004). The scaling analysis was repeated here for all the simulations with $l_{sst} = 10\ km$ and varying T_S, all of them showing a mean linear trend in the log-log power spectra. Fig. 2.14 shows that the variation of fitted values of β with $cf \times {N_m}^2$ displays similar transitions to the ones found for UM parameters, between stable/unstable cases and banded/disorganized convection. The location of the stable/unstable transition now seems to have been shifted to values slightly lower than ${N_m}^2 = 0$. For numerical modeling parameterizations or downscaling, the exact location of this transition should be determined using a large data base of realistic simulations. Yet, the existence of such transition alone, which is supported by both spectra and moment scaling analysis and agrees with expected physical behavior such as for example the Richardson number criteria in boundary layer stability analysis, is an important finding in itself. The colder stratiform cases show some spread in β values that was not found in the UM parameters, including an unphysical $\beta > 3$ value. It should be taken into consideration these cases have shallower clouds (Fig. 2.12), which imply fewer levels of data for computation, along with low intensities of cloud fields, making them susceptible to computational uncertainty in the spectral exponent, adding to the limitations in the spectral analysis. The highly idealized topography with a superposed 2-dimensional sinusoidal field used in the simulations here was designed to replicate and build upon previous works that used linear theory to investigate the development of orographic convection, and is not scaling. The structure of stratiform (terrain following) and orographically triggered convective fields is very influenced by the properties of the topographic elevation (e.g. Barros and Lettenmaier, 1994; Kirshbaum and Durran, 2004; Barros et al., 2004), and therefore a linkage between their scaling properties should exist. Follow up work, with realistic terrain should give further insight into this question.

Theoretically (isotropic) wind speed and passive scale advection in turbulent processes has $\beta = 5/3$ for 3-dimensional turbulence, and 3 for 2-dimensional turbulence. However cloud fields in convective turbulence should not be treated as passive scalars due to strong nonlinear effects such as latent heating release, entrainment, and active thermodynamics and microphysical processes, and therefore these theoretical results cannot be expected to hold. Additionally these theories assume isotropy between horizontal and vertical directions which is not the case in the atmosphere.

2.5 Summary and discussion

Linear stability analysis reveals that embedded convective structures are the result of unstable growth of small-scale disturbances, which should be very important in determining the predictability of orographic precipitation. They also suggest the governing role of parameters such as atmospheric stability, advective timescale, small-scale terrain spectra and cloud depth. The results from idealized numerical simulations of orographic convective precipitation qualitatively agree with these predictions. Particularly, they show that the representation of small-scale terrain (and associated lee waves) plays a very important role for these events, controlling the band spacing and significantly enhancing the convective intensity and rainfall amounts. But these simple models are unable to do any quantitative predictions or even predict the correct pattern (except in very particular cases) due to the presence of nonlinear effects, and alternative nonlinear models are required.

As pointed out by Schertzer and Lovejoy (1992), the contributions of small-scale activity to much larger scales are non-negligible, and indeed the corresponding variability has the most extreme behavior which explains in part the reason why multifractals have been successful on the study of extreme events. In fact several previous works reported statistical multiscaling behavior to be a very general property of geophysical fields (including rain and clouds), providing a convenient alternative framework due to its theoretical simplicity, its ability to handle nonlinear dynamics over very wide range of scales, its potential for downscaling applications and the fact that the convective events studied here are a particular kind of turbulent flow and hence a statistical approach to the problem is appropriate. This multiscaling behavior holds for statistical moments and isotropic power spectra of the simulated rain and cloud fields in

the considered range of scales (~1km to ~ 20 km). The Universal Multifractal model reproduces quite well the empirical estimates of the horizontal scaling exponent function, $K(q)$, and can be used to quantify the multiscaling behavior of the fields. Analysis of single horizontal sections of cloud fields revealed variation of the scaling parameters with vertical position. We argue that if we use an average over several horizontal sections at different vertical levels, we obtain estimates for the horizontal parameters of the entire volume, while the vertical structure should be represented by a different set of (vertical) scaling parameters. This transient 3-dimensional anisotropic scaling framework seems to be a promising starting point to investigate relations between the statistical and physical properties and perform downscaling for mesoscale events. Results from both 2- and 3-dimensional approaches revealed significant variations of $K(q)$ and respective UM parameters with small-scale terrain spectra, atmospheric stability and advective timescale. Therefore, the representation of sub-grid scale variability of cloud and rainfall fields using statistical multifractal diagnostics would intrinsically depend not only on the properties of the field itself, but also on particular geographic location and atmospheric conditions, bringing the necessity of developing relationships to predict the scaling parameters from coarse grid atmospheric data and terrain spectra. However, the results also suggest that the development of such relationships is far from being trivial because they appear to involve complex nonlinear behavior.

A particularly robust behavior found here is the abrupt transition in the UM parameters between stable and unstable cases, which has a clear physical correspondence as a transition from a more stratiform to a more organized (banded) convective regime. This behavior is also found in the spectral exponent β. Another instability measure, CAPE, also seems to be a good predictor, but it is unable to distinguish between the different stable cases and CIN might have to be used in conjunction. ${N_m}^2$ also has the advantage of allowing a linkage with the analytical models where it appears explicitly, which is not so clear for CAPE. It was also found that the scaling of the surface accumulated precipitation field (usually an important field to be parameterized and downscaled) is a complex function of the horizontal scaling of several other fields such as water mixing ratios in the different phases and probably l_{sst} and τ_{adv}.

The scaling of the power spectrum can be taken advantage to perform stochastic spatial downscaling (disaggregation) of instantaneous rain and cloud field (see e.g. Bindlish and Barros,

1996 and 2002; or Rebora et al., 2006). The present work suggests that scaling parameters could be computed from known large scale measures (such as stability and terrain spectra). Although the focus of spectral analysis is on second order statistics, and hence the scaling behavior at other orders is neglected by this type of downscaling approach, the time dependency of the scaling parameters is introduced by the temporal evolution of the atmospheric conditions, and the usually small time step used in numerical simulations can be advantageous to achieve a high temporal representation. Further improvements could include scaling constraints using higher-order moments.

Finally, it is important to point out some limitations of our study. In order to investigate the dependence of the multifractal properties on mean properties, a limited range of highly idealized simulations are used where we can control the mean atmosphere with a small number of simulation parameters. Because our work suggests a transient dependence of the scaling on mean properties, the analysis is performed on instantaneous fields, rather than ensemble averages, which increases the volume of data necessary for analysis. Horizontal isotropy is assumed, and it is important to stress that the issue of existence of horizontal anisotropy must be tackled in the future. The solutions show robust horizontal scaling even though the only external forcing is a very simple terrain with poor scaling and the initial conditions are horizontally homogeneous. In realistic cases, the atmosphere and terrain forcing will themselves be scaling, which might influence the scaling of the solutions. Models such as WRF involve many subgrid scale parameterizations which vary among model configurations. Here we use parameterizations only for subgrid turbulence closure and microphysical processes. Whether these parameterizations introduce unphysical scaling behavior in the models at resolved scales, and whether the scaling depends on the particular chosen parameterizations are legitimate questions. Furthermore, in the real atmosphere there are many other effects not considered here such as radiation, earth rotation, surface and boundary layer effects which might introduce further complications and influence the scaling. In this study, however we spell out unambiguously what processes are resolved or not, and there is general a body of literature that shows that the resolution adopted can resolve explicitly dominant convective structures (see for example Fuhrer and Schär, 2007). In fact, as pointed out in Section 2.2, our simulations are based on previous work where the authors showed that they reproduce the essential features of the observed convective structures in the Oregon Coastal Range. Harris et al. (2001) compared the scaling observed and model produced

precipitation fields at 3-km resolution, finding an encouragingly similar behavior at scales above 5 times the resolution (i.e. 15 km). Although they simulated realistic cases with different model and parameterizations than here, the model is based on the same governing equations. Our assumption here is that our simulations, based on nonlinear, compressible and non-hydrostatic Navier-Stokes equations coupled with the thermodynamics equations in the WRF model under the specified forcing conditions represent the key physical processes of interest and that the multifractal parameters can be used to describe the behavior of the simulated system in the explicitly well resolved scales. It is important to stress that the fields resulting from numerical simulations should reproduce the scaling in geophysical observations if they are to be realistic. Furthermore, we apply multifractal analysis not as means to find universal parameters that will exhibit consistency, though that could be a result, but rather as a mathematical model can capture, any given scale, variability that reflects a large dynamical range of the phenomena determined by the long range dependencies. Thus, what is consistent is the model used to describe variability; we then make use of the multifractal model parameters as metrics that can help interpret model dynamics and thermodynamics in a systematic way. The presence of an underlying multifractal behavior is robustly supported by the evidence presented: a clear mean linear trend in the spectral analysis in conjunction with the robust scaling in the moment analysis, which is less sensitive to the data limitations and reveals robust scaling behavior up to orders of about 2, as it is typically found in atmospheric fields and reported in literature consistent with the scope of the present manuscript.

Although much insight was gained into scaling dependencies, particularly the presence of transient dependence of scaling parameters on mean conditions found here, an investigation on observational atmospheric data and realistic numerical simulations is warranted, along with further support to whether numerical weather prediction models are able to reproduce, at least to some extent, the multifractal properties of simulated fields and what is the effect of the particular parameterizations chosen on the scaling. This is currently ongoing work.

Acknowledgements

The authors would like to thank three anonymous referees for their comments and suggestions which helped to significantly improve the manuscript. This research is supported by the Portuguese Foundation for Science and Technology (FCT) under grants SFRH/BD/61148/2009

and PTDC/CTE-ATM/119922/2010, and NASA grant NN1010H66G and NSF grant EAR-0711430 with the second author.

3 Transient Stochastic Downscaling of Quantitative Precipitation Estimates for Hydrological Applications[†]

Abstract

Rainfall fields are heavily thresholded and highly intermittent resulting in large areas of zero values. This deforms their stochastic spatial scale-invariant behavior, introducing scaling breaks and curvature in the spatial scale spectrum. To address this problem, spatial scaling analysis was performed inside continuous rainfall features (CRFs) delineated by applying cluster analysis. The results show that CRFs from single realizations of hourly rainfall display ubiquitous multifractal behavior that holds over a wide range of scales (from ≈ 1 km up to 100's km). The results further show that the aggregate scaling behavior of rainfall fields is intrinsically transient with the scaling parameters explicitly dependent on the atmospheric environment. These findings provide a framework for robust stochastic downscaling, bridging the gap between spatial scales of observed and simulated rainfall fields and the high-resolution requirements of hydrometeorological and hydrological studies.

Here, a modified fractal downscaling algorithm is presented and applied to generate 7 years of stochastically downscaled hourly rainfall products from radar derived StageIV (~4km grid resolution) quantitative precipitation estimates (QPE) over the Integrated Precipitation and Hydrology Experiment (IPHEx) domain in the southeast USA. The methodology can produce large ensembles of statistically robust high-resolution fields without additional data or any calibration requirements, conserving the coarse resolution information and generating coherent small-scale variability and field statistics, hence adding value to the original fields. Moreover, it is computationally inexpensive enabling fast production of high-resolution rainfall realizations

[†] Nogueira[(1,2)], M. and Barros[(2)], A. P., 2014: Dynamical Downscaling of Quantitative Precipitation Estimation for Hydrological Predictions in the Southern Appalachians. Submitted to J. of Hydrology

(1) CGUL-IDL, University of Lisbon, Portugal.

(2) Duke University, Durham, North Carolina, U.S.A.

with latency adequate for forecasting applications. When the transient nature of the scaling behavior is considered, the results show a better ability to reproduce the statistical structure of observed rainfall compared to using fixed scaling parameters derived from ensemble mean analysis.

The value of the downscaled products is demonstrated through hydrological simulations of two distinct storm events in the Southern Appalachians, a winter storm that caused multiple landslides and a summer tropical event that caused flashfloods. The simulations are forced by the entire span of plausible fractally downscaled rainfall fields at two distinct resolutions (1km and 250m). The results show very good skill against the observed streamflow, especially with regard to the timing and peak discharge of the hydrograph, and the accuracy is enhanced by increasing the target downscaling resolution from 1 km to 250 m. Probabilistic simulations of both events capture the observed behavior indicating that the proposed CRF-based stochastic fractal interpolation provides a generalized framework for producing fast and reliable probabilistic forecasts and their associated uncertainty for extreme events and risk management of hydrometeorological hazards , as well as long-term hydrologic modeling.

3.1 Introduction

Heavy rain events over mountainous terrain present a great challenge for forecasters and are the leading cause of natural hazards including flashfloods, shallow landslides and debris flows. Predictability of these events depends on access to precipitation products at spatial and temporal resolutions finer than the scales currently resolved by the Numerical Weather Prediction (NWP) models, or the observations used to produce Quantitative Precipitation Estimates (QPE) (e.g. ground-based radar). Consequently, rainfall downscaling methodologies are of primary importance for many hydrometeorological applications. Rainfall fields are the result of several nonlinear interactions among physical processes occurring over a wide range of scales, posing a considerable challenge for deterministic interpolation methods to represent the resulting complex rainfall structure. Thus, stochastic downscaling raises as a natural alternative, capable of producing a large span of plausible solutions over a short time period, a crucial requirement for operational forecasts.

Various stochastic interpolation strategies have been developed aiming to reproduce the sub-grid scale rainfall variability by adding (statistically) realistic high-frequency heterogeneity, hence increasing the information content of coarser commonly available datasets that do not meet the high resolution requirements of hydrological modeling and risk assessment and hazard prediction. Ferraris et al. (2003) undertook a comparison of several such methods and found similar ability over all alternatives to generally reproduce the statistics of precipitation fields, but significant errors in their ability to reproduce the statistics of particular fields. While significant efforts have been made over the last 10 years, stochastic downscaling of rainfall fields is still largely an open problem (e.g. Kim and Barros, 2002; Rebora et al., 2006; Barros and Tao, 2008; Brussolo et al., 2009; Tao and Barros, 2010; Ebtehaj et al., 2012; Foufoula-Georgiou et al., 2014). The present work aims to address this issue focusing on stochastic downscaling methodologies based on modified fractal interpolation performed in the Fourier spectrum framework, which has been previously shown to preserve the spatial and temporal structure in the coarse resolution information while enhancing variability in the smaller unresolved scales (Bindlish and Barros, 1996, 2000; Kim and Barros, 2002; Rebora et al., 2006; Barros and Tao, 2008; Brussolo et al., 2009; Tao and Barros, 2010).

A large number of investigations over the past 30 years reported spatio-temporal stochastic scale-invariant behavior of rainfall fields (and other geophysical quantities) across scales (see Lovejoy and Schertzer, 2007 for a review). This scaling behavior implies that statistical properties of rainfall fields at different scales are related by power laws, and physically based models and downscaling algorithms should reproduce this scaling behavior if they are to generate realistic fields.

Bindlish and Barros (1996) developed and applied a fractal interpolation method to map digital elevation maps at different spatial resolutions using a modified fractional Brownian surface (fBs) to match the correct spectral scaling as the interpolating surface. While such approach preserves well the spatial structure of the data, the generation of the fBs introduces a random component at the sub-grid scales where the Fourier phase is unknown. To tackle this problem Bindlish and Barros (2000) modified the fractal interpolation scheme to include the spatial properties of regional topography and NWP simulated hourly winds to add physical constraints to the fBs generation. Subsequently Kim and Barros (2002) and Barros and Tao (2008) used fields of

variables at higher spatial resolutions to estimate the sub-grid scale variability of fields at coarser scales conditional on the underlying conceptual physical model of precipitation processes. While this strategy circumvents the need to estimate the random phase component by providing deterministic physically-based constraints to precipitation variability, it requires high-resolution fields with scaling behavior closely linked to rainfall, thus severely restricting the application and target resolutions of the downscaling schemes, in particular for forecasting applications that require short latency times.

Rebora et al. (2006) presented a rainfall downscaling algorithm similar to Bindlish and Barros (1996) but including the time dimension and assuming that the exponents remained constant throughout the chosen period. More recently, Tao and Barros (2010) also applied a method similar to Bindlish and Barros (1996) to downscale TRMM 3B42 quantitative precipitation estimates (QPE) without using high-resolution ancillary data that are generally unavailable. Their results showed that fractal interpolation methods are limited by the quality of the coarse resolution information content, and by the ability to determine the correct scaling properties for each particular storm. Despite these limitations, fractal methods generally performed consistently better in downscaling rainfall fields than other widely used interpolation methods, which are unable capture the correct sub-grid scale statistical structure.

A further source of complexity comes from the fact that some geophysical fields, such as rainfall and clouds, exhibit very strong physical thresholds, and thus intermittency, that result in large fractions of zero values both in time and space. Moreover, any measurement no matter how precise has an associated minimum detection threshold that contributes to increasing the fraction of zeroes in measured fields, and thus distinguishing between measurement and physical zeroes becomes virtually impossible for most applications and datasets. It has been known for some time that large fractions of zeroes influence scaling behavior (Harris et al., 1996; Schmitt et al., 1998), but this fact has received little attention in rainfall field analysis until recent work of Montera et al. (2009) reporting that the presence of numerous zero rainfall values in the data is associated with deformations of temporal scaling behavior, causing scaling breaks and biasing the estimation of scaling parameters. Verrier et al. (2011) reached a similar conclusion using high temporal resolution disdrometer data over France, while Verrier et al (2010) and Gires et al. (2012) found that the presence of large portions of zeros also deformed the spatial scaling

behavior in high-resolution radar data and multifractal synthetic simulations. Verrier et al. (2010) suggested that single universal parameters could be found only when looking at near space filling events, though Gires et al. (2012) found clearly distinct scaling parameters between two different rainfall events even after explicitly taking the zero problem into account.

The question of whether the spatial (and temporal) scaling parameters of rainfall are universal properties estimated from ensemble analysis, or dynamical quantities that depend on the particular system state and forcing remains open. The dynamical scaling scenario is supported by the widespread range of values for the scaling parameters for rainfall fields that can be found in the relevant literature. Furthermore, several investigations found evidence that scaling behavior holds to a very good approach in single realizations over considerable ranges of scales with dynamically variable scaling parameters that have been linked to underlying atmospheric properties such as mean rainfall rate (Over and Gupta, 1994; Deidda et al, 2004), atmospheric stability (Perica and Foufoula-Georgiou, 1996; Nogueira et al., 2013), mean wind speed (Nogueira et al., 2013) and underlying terrain forcing (Barros et al., 2004; Nykanen, 2008; Nogueira et al., 2013). Nevertheless, *a priori* determination of the correct scaling parameters faces many challenges due to the highly transient and nonlinear nature of the linkages among different atmospheric fields.

In the present work, we take advantage of an existing QPE dataset at 1-km resolution over the Southeastern US at hourly time intervals rate during a period of 3 years, which we take as reference to perform spatial scaling analysis on numerous realizations of rainfall fields, each with enough data points to produce robust statistics and encompassing a wide variety of different precipitation events over the IPHEx domain (Barros et al., 2014). This presents a unique opportunity to investigate the transient character of the multifractal parameters toward characterizing regional rainfall scale-invariance, and the effect that zero-values have on this scaling behavior. In particular, to the best our knowledge, this study reports for the first time results from spatial scaling analysis inside continuous rainfall features (hereafter CRFs) isolated by cluster analysis, rather than using space filling images to remove the zero effect. The zero-nonzero distribution of rainfall is then characterized using a binary fractal analysis. The insights obtained from the scaling analysis are used to perform transient fractal downscaling in the Fourier domain, specifically to downscale the NCEP StageIV QPE product at 4-km resolution

(Baldwin and Mitchell, 1998; Lin and Mitchell, 2005) to 1km and 250m resolutions required for the hydrological applications during the Integrated Precipitation and Hydrology Experiment (IPHEx, http://iphex.pratt.duke.edu, see Barros et al., 2014). In particular, 7 years (2007-2013) of ensembles of 50 hourly rainfall fields were generated and are publicly available.

The manuscript is organized as follows: a description of the datasets and scaling analysis framework is given is Section 2 and the results of spatial scaling analysis of hourly rainfall fields at 1km resolution over the SA region are presented in Section 3, taking into account the rainfall zeroes problem. In Section 4 the fractal behavior of the binary rain support is investigated and related to the fraction of zero values. Two downscaling schemes based on modified fractal interpolation are presented in Section 5, and the main conclusions are summarized in Section 6.

3.2 Data and Methodology

3.2.1 Datasets

The analysis of the scaling behavior of rainfall is performed for hourly rainfall fields at 1 km spatial resolution available during a three year period (starting in June/15/2008) over the Southern Appalachian region (delimited by black line in Fig. 3.1a), representing a 530×420 km^2 sub-region of the Integrated Precipitation & Hydrology Experiment (IPHEx) core domain (corresponding to the full area in Fig. 3.1a). The National Mosaic and Multi-sensor QPE (NMQ) project at the National Oceanic and Atmospheric Administration (NOAA) National Severe Storms Laboratory (NSSL) high-resolution QPE fields are derived from the radar-based and local gauge-corrected providing hybrid scan Reflectivity products (Vasiloff et al., 2007).

The National Center for Environmental Prediction (NCEP) Stage IV dataset of gridded QPE at 4 km resolution, derived from the Next Generation radar network (NEXRAD) over the US and corrected with raingauge information (Baldwin and Mitchell, 1998; Lin and Mitchell, 2005) is the highest resolution dataset available with the spatio-temporal coverage required for IPHEx. These data are used as coarse scale forcing for the stochastic downscaling procedures used to generate 1-km resolution QPE fields required for hydrological application during the IPHEx project. Prior to downscaling, the QPE fields are re-projected to a UTM17N (WGS84) grid at $4 \times$

4 km resolution over the IPHEx study region focusing on four major SA river basins - the Upper Tennessee, Catawba-Santee, Yadkin-Pee Dee and Savannah River (Fig. 3.1) .

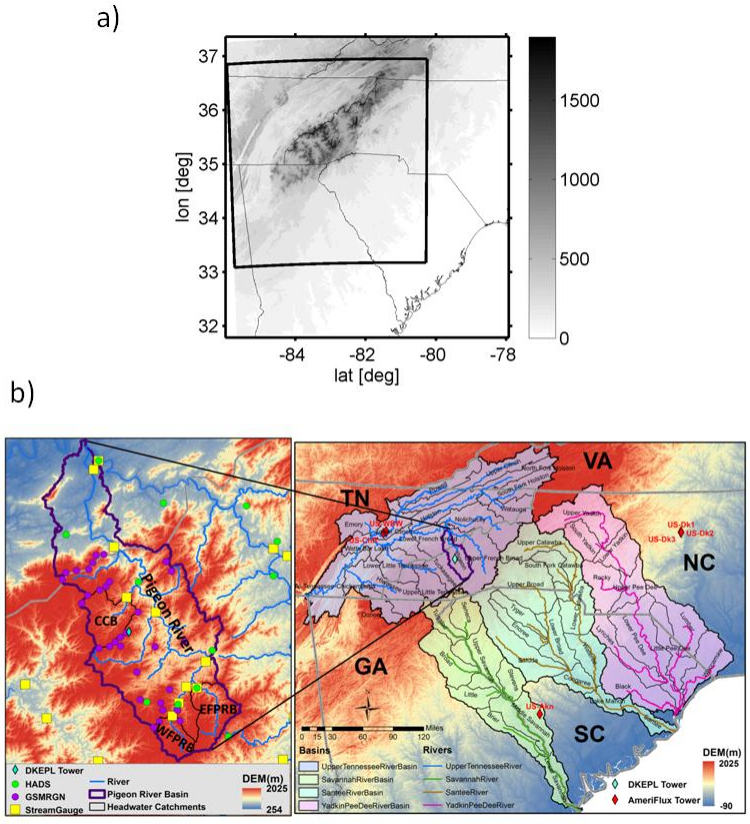

Figure 3.1 *a) The IPHEx domain topographic elevation and the NMQ Q2 data sub-domain (delimited by black line). b) The four drainage basins of interest in this project (shown on the right), namely Upper Tennessee River Basin, Savannah River Basin, Santee River Basin and Yadkin-Pee Dee River Basin. The Pigeon River Basin (shown on the left), is the domain for the conducted hydrological verification at three sub basins that are not limited by dam operation in the Pigeon River Basin, including the Cataloochee Creek Basin, the West Fork Pigeon River Basin (WFPRB) and the East Fork Pigeon River Basin (EFPRB).*

The Pigeon River Basin (PRB) in the Upper Tennessee (Fig. 3.1b) and in particular one of its tributaries the West Fork Pigeon River Basin area (WFPRB), was chosen as the test-bed for the hydrological simulation experiments presented in Section 3.5, a small (about 70 km^2) headwater catchment that provides a good reference to evaluate the precipitation products without

introducing the spatial integration artifacts of the simulations at large scales. The hydrological model and simulation setup were described in detail in Tao and Barros (2013, 2014a).

3.2.2 Scaling Analysis

Based on cascade phenomenology models, the spatial scaling behavior of statistical scale invariant fields is often investigated by analyzing their statistical moments, which are expected to obey the generic multiscaling relation (Lavallée et al., 1993):

$$M_q = < \varphi_\lambda{}^q > \approx \lambda^{K(q)} \tag{3.1}$$

where < > represents the statistical average, q is the moment order generalized to any positive real number, $\lambda = L_0/l$ is the scale ratio, L_0 being the outer scale of the cascade (the largest scale of variability) and l the scale of the observation, or simulation. Here, φ_λ is a quantity that is on average conserved from scale to scale, analogous to turbulent flux in cascade models. This quantity is non-dimensionalized and normalized, such that $< \varphi_\lambda >= 1$. For a multifractal quantity the moment scaling exponent function, K(q) is a convex nonlinear function of q and thus infinite number of scaling exponents are necessary to fully characterize the scaling behavior. Based on multiplicative cascade processes and the stability properties of cascade generators, Schertzer and Lovejoy (1987) showed that K(q) can be modeled by Eq. 2 reducing the problem to the determination of two parameters, α and C_1.

$$K(q) = \begin{cases} \frac{C_1}{\alpha-1}(q^\alpha - q), & \alpha \neq 1 \\ C_1 \, \mathrm{qlog}(q), & \alpha = 1 \end{cases} \tag{3.2}$$

The Levy index, α, is defined in the interval [0,2] and indicates the degree of multifractality, with $\alpha = 0$ for monofractals. The co-dimension of the mean singularity, C_1, describes the sparseness or non-homogeneity of the mean of the process such that the higher the C_1 value the more intermittent the field, with more sparse peaks of higher amplitude (Sun and Barros, 2010).

Because there is no physical basis to assume that rainfall fields should be conserved on a scale by scale basis, and in fact most geophysical fields are found to behave as non-conservative quantities, a third multifractal parameter must be introduced, the non-conservation parameter, H,

which represents the degree of smoothness of the process. In the canonical non-conservative case, the mean exhibits scale dependence, $< \Delta f > \sim l^H$, while for a conservative process (where H=0) it is found that $< \varphi_\lambda >= cte$. The non-conservation parameter can be easily estimated from the slope of the log-log plot of the first order structure function against the lag (Harris et al., 2001; Lovejoy et al., 2008):

$$S_1 = |\Delta F| \approx \varphi_\lambda |\mathrm{l}|^{\mathrm{H}} \tag{3.3}$$

where $\Delta F = F(x + l) - F(x)$ is a fluctuation in the field F over a distance l. When H is nonzero, an additional fractional integration of order H is needed to obtain the fractionally integrated flux (FIF), corresponding to the conserved quantity. However, in practice, taking normalized absolute value of the finite difference gradient at the highest resolution available, l_0, provides a good approximation of the underlying conservative cascade (Lavallée et al., 1993):

$$\Delta f_{l_0} = \{[F(x + l_0, y) - F(x, y)]^2 + [F(x, y + l_0) - F(x, y)]^2\}^{1/2} \tag{3.4}$$

The FIF estimates given by Eq. 3.4 are normalized and systematically degraded to lower resolutions (lower values of λ) by spatial averaging to obtain φ_λ used to compute the statistical moments in Eq. 3.1. Linear relations in log-log plots of the q-order moments against λ indicate the presence of underlying multifractal behavior in the rainfall fields, the slopes being estimates of K(q). The parameters α and C_1 can be estimated using the simple relationships (e.g. Lovejoy et al., 2008; Verrier et al., 2010): $K'(1) = C_1$ and $K''(1) = \alpha C_1$. Alternatively more sophisticated methods such as the Double Trace Moment (DTM) technique described by Lavallée et al. (1993) can be used to obtain estimates of the UM parameters.

Spectral analysis can also be used to investigate the presence of scale-invariant behavior over a wide range of scales in rainfall fields. Spatial scaling invariance manifests itself as log-log linearity of the power spectrum in space:

$$E(k_i) \approx {k_i}^{-\beta_i - 1} \tag{3.5}$$

where k_i represents the wavenumber in the x_i direction. Consequently, the spectral exponent β_i that describes the variability of the rainfall field as a function of scale can be estimated using least square regression in log-log plots.

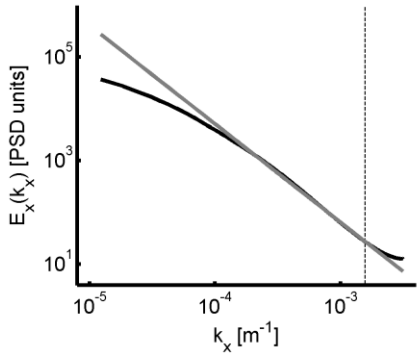

Figure 3.2 *Ensemble x-direction log-log power spectrum for the 3 year period. The gray line represents the ensemble spectral exponent* $\beta_{Ens} \approx 1.9$ *estimated from cluster analysis. The vertical black dashed line represents* $4\Delta x$ *scale.*

3.3 Scaling behavior of rainfall fields

3.3.1 Ensemble scaling analysis

First the spatial scaling behavior of rainfall fields is investigated by considering ensemble statistics over the available 3 years of NMQ. Figure 3.2 shows the log-log 1-dimensional Fourier power spectra in the x-direction. Note the scale break at $4\Delta x$ length (vertical black dashed line), with increased variability and decreased slope at lower scales associated with instrumental noise and difficulties in Fourier analysis applied to finite data samples. Thus, these scales are not taken into consideration here. At larger scales, the spectrum displays curvature with decreasing slope, suggesting the existence of a scaling break separating two different regimes: one extending from the smaller scales up to $\approx 20 - 30$ km with steeper spectral slopes, and a second regime at the larger scales displaying non-linear (curvature) and hence non-scaling behavior, or a less steep linear scaling behavior.

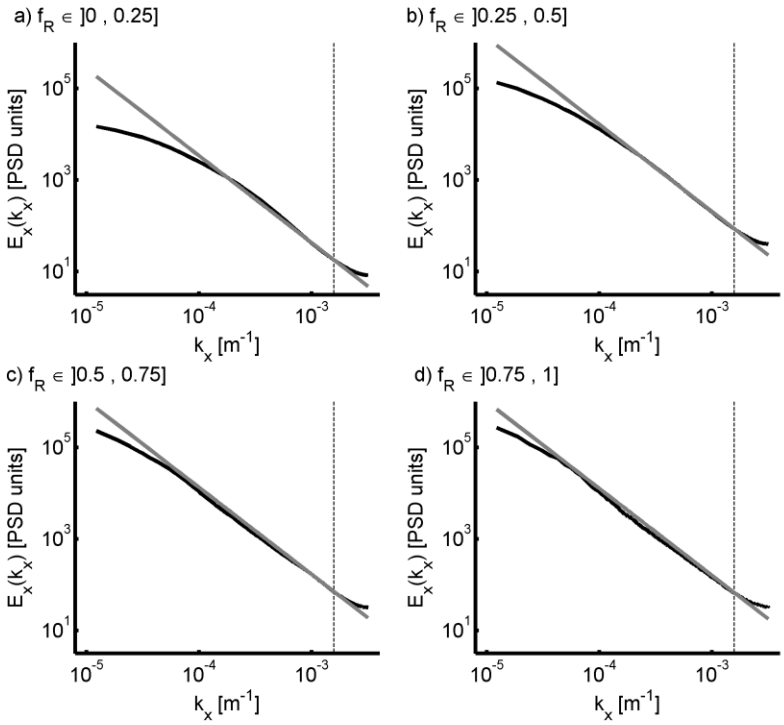

Figure 3.3 *Ensemble x-direction log-log power spectrum computed the 3 year period for different rain fraction, f_R, categories. The gray line represents the ensemble spectral exponent $\beta_{Ens} \approx 1.9$ estimated from cluster analysis. The vertical black dashed line represents $4\Delta x$ scale.*

The rain fraction, f_R, defined as the number of pixels with nonzero rainfall rate values (R>0) divided by the total number of pixels, is computed for each hourly rainfall field and classified into one of four f_R categories: i) $f_R \in]0,0.25]$, ii) $f_R \in]0.25,0.5]$, iii) $f_R \in]0.5,0.75]$or iv) $f_R \in]0.75,0.1]$. The ensemble spectra computed for each category (Fig. 3.3) shows a clear association between the curving of the spectra and the presence of zero values, with deformation from linear behavior decreasing for increasing f_R (decreasing number of zero values) and a tendency of the slope to approach a value of $\beta_{Ens} \approx 1.9$, represented by the gray lines in Fig. 3.2 and Fig. 3.3. Over large domains, at high-resolutions, realizations close to space filling ($f_R \approx 1$) are very rare - only 8 cases with $f_R \geq 0.975$ out of 26,320 fields (corresponding to $\approx 0.03\%$) in the three year database examined here. Consequently the highest f_R category considered (iv) is as low as 0.75 allowing up to 25% of zero pixels in order to keep ensemble statistics robust with a considerable amount of realizations. This fact can explain the presence of deformation in the largest scales in this category (Fig. 3.3d). Spectral analysis in the y-direction (Fig. 3.4) shows the

same decreasing curvature and tendency to $\beta_{Ens} \approx 1.9$ as f_R increases, providing further robustness to the results.

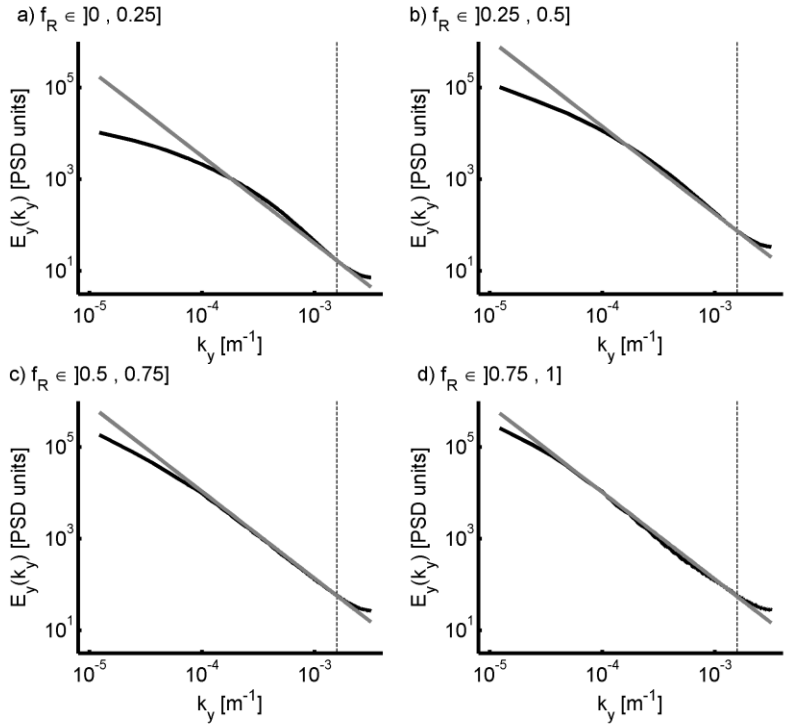

Figure 3.4 *Same as Fig. 3.3 but in the y-direction.*

Using the same f_R classification, similar deformation associated with the presence of zero values is found for the ensemble first order structure function (Fig. 3.5), with more pronounced curvature at the larger scales for decreasing f_R and associated decreasing slope. As f_R increases there is a tendency towards an ensemble linear scaling behavior, characterized by $H_{Ens} \approx 0.5$. The scales smaller than $4\Delta x$ are not considered for the same reasons enunciated for the spectral analysis. Figure 3.6 shows the log-log plots of ensemble x-direction statistical moments against the scale ratio, λ (see Eq. 3.1). The statistical moments, M_q, were computed for different f_R categories and different moment orders q (from bottom q=0.5 at 0.5 steps to q=2.5 at the top). As commonly reported in the relevant literature for spatial scaling analysis, we restrict our study to orders only up to q=2.5 due to sample size limitations and divergence of moments at orders greater than critical order $q_D \approx 3$ (e.g. Lovejoy et al., 2008; Nykanen, 2008). Consistent with the results of spectral and structure function analysis, M_q also shows curvature and break of the

scaling behavior at the large scales (small λ) for low f_R cases, but approaches linear scaling behavior as f_R increases. The gray lines in Fig. 6 are obtained by linear fit between $4\Delta x$ and the domain length scale, and the slopes are estimates for the moment scaling function exponent K(q). As f_R increases, α increases approaching 1.8 while C_1 decreases approaching 0.1. These hold for the ensemble structure function and moment scaling analysis in the y-direction with similar scaling parameters (not shown).

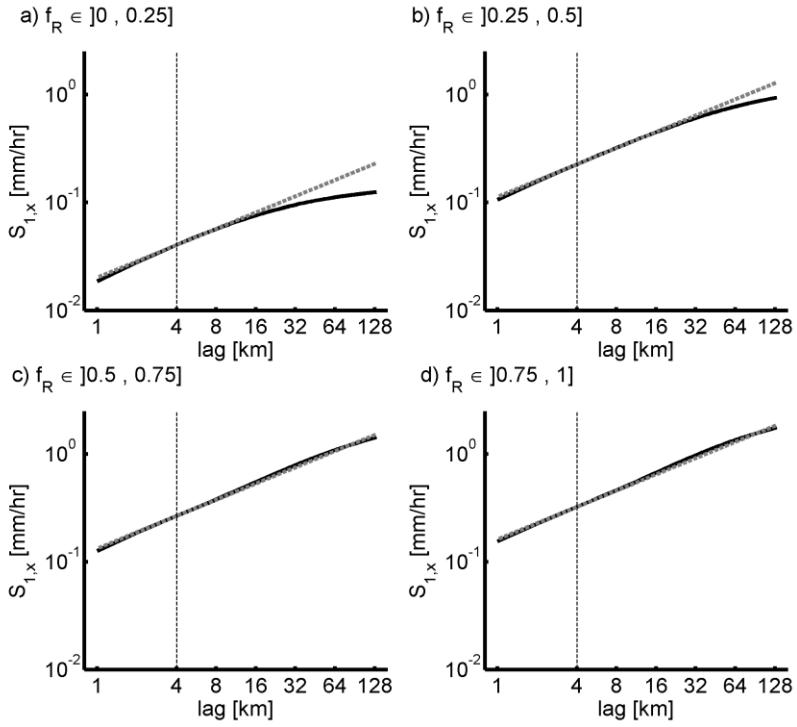

Figure 3.5 *Log-log plot of the first order structure function, S_1, against the scale lag, Δx for different f_R categories. Gray dashed lines represent fitted ensemble slopes obtained from high f_R cases, corresponding to $H \approx 0.5$.*

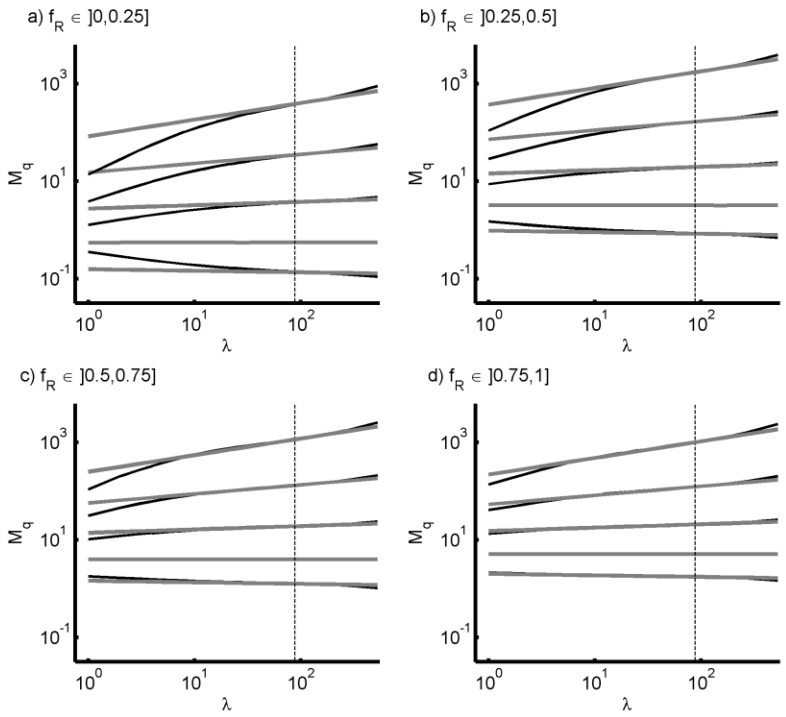

Figure 3.6 Log-log plot of statistical moments, M_q, against the scale ratio, λ, for different f_R categories. Black lines represent M_q for q= 0.5, 1, 1.5, 2 and 2.5 from bottom to top in ascending order. Gray lines represent fitted ensemble slopes obtained from cluster analysis.

3.3.2 Cluster Analysis

The spatial scaling analysis is repeated for nonzero rainy regions alone by using cluster analysis to identify and isolate CRFs. A CRF is defined as a cluster of contiguous pixels with rainfall larger than zero, i.e. each pixel in a cluster of size greater than 1 pixel has at least one adjacent rainy pixel with nonzero intensity. All clusters are identified in each hourly realization during the three year period of data availability. Scaling analysis is performed by finding all possible non-overlapping segments of l consecutive nonzero rain pixel in each horizontal direction for each CRF. This methodology has three main advantages over the use of a very high $f_R \approx 1$ criteria to remove the influence of zeros on the spatial scaling: i) the rain fraction inside clusters is space filling (i.e. $f_R = 1$) rather than approximately so; ii) for a large spatial domain there are very few realizations (here only 8 events in 3 years) with very large rainfall fraction (e.g. $f_R \geq 0.975$); and more importantly iii) such choice of large f_R would bias the analysis towards large scale events,

such as large mesoscale convective systems (MCS) or large synoptic-systems. Consequently, the scaling behavior would not capture the scaling behavior of smaller structures such as summer and/or orographic convective events, which are critical to this region. The ensemble Fourier 1-directional spectra is computed over all segments from all CRFs in the dataset. The analysis is performed for segment length, l, values of l=64 and l=128 pixels. The results show strong scaling (Fig. 3.7), extending from 4 to 128 km with consistent average slopes $\beta_{Ens} \approx 1.9$. The curvature problems in scaling remain at small scales (below about $4\Delta x$) for the same reasons explained above.

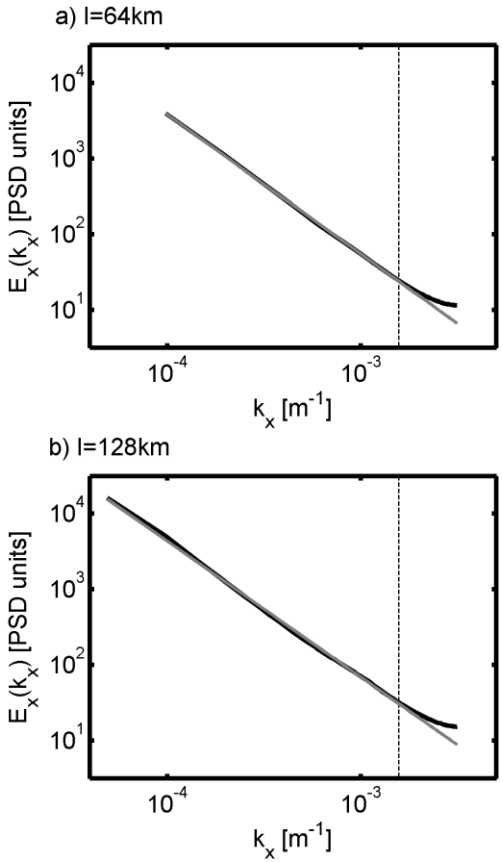

Figure 3.7 *Ensemble x-direction log-log power spectrum for the 3 year period computed inside rain clusters only, for segment lengths a) l=64 km and b) l=128km and corresponding least-square fit (gray). The vertical black dashed line represents* $4\Delta x$ *scale.*

Ensemble moment scaling analysis from rain cluster segments with l=64 and 128 km, also show remarkable scaling with $C_1 \approx 0.1$ and $\alpha \approx 1.9$ for both segment lengths (Fig. 3.8), remarkably

close to the previously found ensemble values when f_R is increased. Notice that because we are looking at nonzero values only, the present C_1 parameter is not associated with on-off intermittency but with intermittency within the (nonzero) rain structures. The ensemble scaling analysis in the y-direction shows results very similar to the x-direction, supporting the average horizontal isotropy approximation. The structure functions are not computed for rain clusters due to severe difficulties in their computation over narrow ranges of scales. However, taking into account the Wiener-Khintchine theorem, H can be related to β and K(q) by: $\beta = 1 + 2H - K(2)$ (see e.g. Tessier et al., 1993) resulting in $H \approx 0.55$ for both segment lengths, which is similar to the value estimated for high f_R cases.

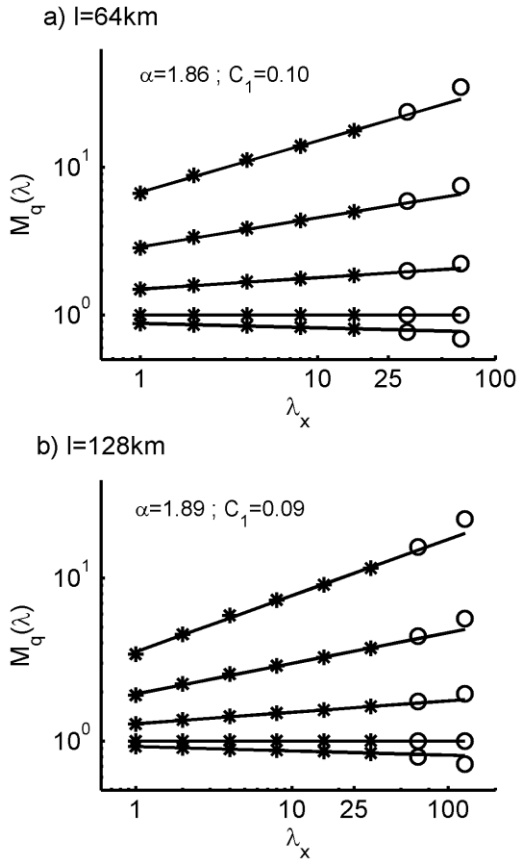

Figure 3.8 *Log-log plot of ensemble statistical moments M_q against λ computed inside rain clusters (rainy pixels) only, with a) l=64 km and b) l=128 km. From bottom to top the lines represent respectively q=0.5, 1, 1.5, 2 and 2.5. Star markers represent scales $> 4\Delta x$ and `o' markers scales $\leq 4\Delta x$. Black line represents least square fit.*

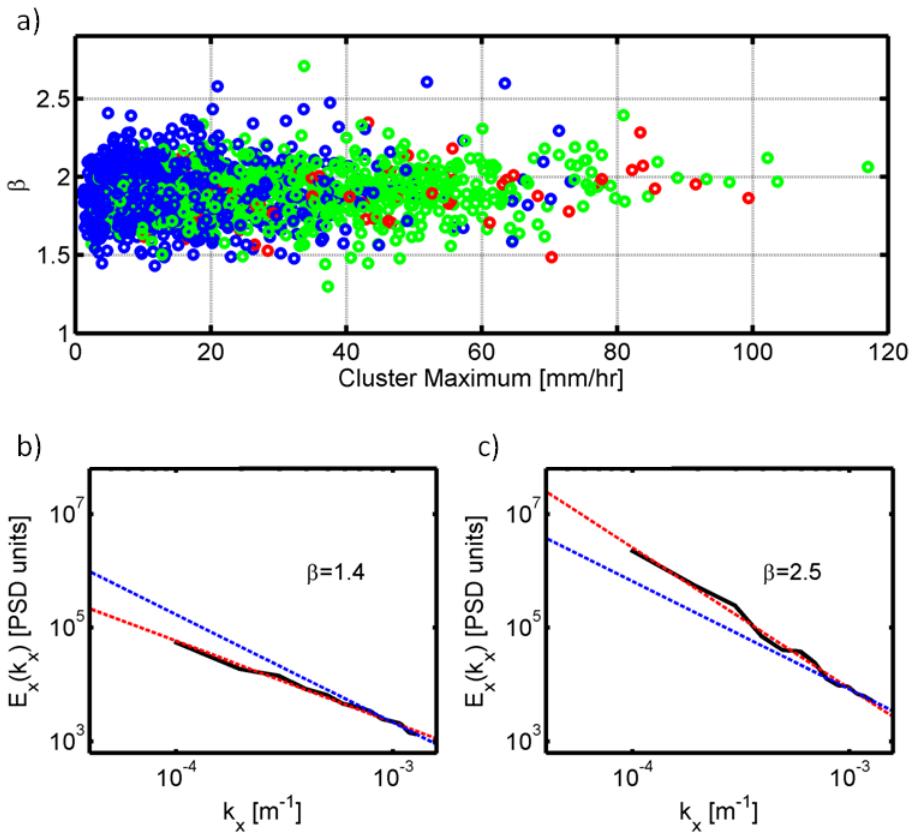

Figure 3.9 *a) β against the cluster maximum intensity value. Stratiform, convective and mixed cases are respectively identified by blue, red and green markers. Log-log power spectrum example for single realization field with b) $\beta \approx 1.4$ and c) $\beta \approx 2.5$. Red dashed lines represent least-square linear fit to the spectrum and blue dashed line corresponds to $\beta_{Ens} \approx 1.9$. The power spectra are computed inside rain clusters (rainy pixels only) considering l=64 km.*

The transient nature of the scaling parameters is investigated by repeating the analysis for each realization of hourly rainfall, using the same CRF identification procedure to take into account the scaling deformation associated with zero values. There is clear variability of the parameters characterizing the aggregated scaling behavior with time, with most β values in the range [1.5, 2.5] (Fig. 3.9a). To eliminate the variability introduced by poor linear fitting, only cases with very high least-square regression coefficient (R^2>0.99) are considered, or in other words only cases where linear log-log behavior holds to a very good degree of approximation in the power spectrum are considered, as exemplified in Fig. 3.9b and Fig. 3.9c for high and low β values. For these two examples with very distinct β values, the power-law behavior is observed to a very

good approximation, displaying clearly distinct spectral slopes from the ensemble 1.9 value (represented by blue dashed line). However, Fig. 3.9a shows that this complex variability of the scaling parameters does not exhibit any clear dependency to CRF maximum intensity or rain type, the latter identified by the marker colors - convective (red), stratiform (blue) and mixed convective-stratiform (green). These classes were established using co-located (in space and time) infrared brightness temperature imagery from NCEP/CPC Global IR Dataset at 4km resolution, following the methodology presented by Evans (1996). Other properties such as CRF area, rainfall variability inside the cluster or mean topographic elevation underlying the cluster were also tested, but no clear simple relations were found. This result doesn't rule out the existence of linkages, but points out their complex dynamical nonlinear character, as suggested by Nogueira et al. (2013). Another important property of single realization analysis is the noisier character of the spectrum with the possibility of occurrence of localized peaks at certain frequencies, despite a clear mean linear tendency. It is possible that these peaks have important physical meaning being associated with dynamical interactions at play for the particular atmospheric conditions and regional topography, thus representing actual physical effects and not spurious variability caused by poor data sampling and measurement noise.

The UM parameters also display considerable variability among different realizations (Fig. 3.10). As for the spectral analysis, only fits with high linear-regression (R^2>0.99) coefficient are considered. Most C_1 values are distributed between 0.05 and 0.2, with the exception of some higher values associated very low intensity clusters where estimation errors become large. The multifractal parameter α varies essentially between values 1 and 2, displaying outlier values associated with low intensity clusters. This is not surprising given the difficulty in estimating α as pointed out by Lovejoy et al. (2008). Even disregarding all the outliers, there is still relevant variability of the UM parameters, noticing for example that a variation of 0.1 in C_1 can have a large impact on the field statistics as shown in Sun and Barros (2010). Higher values of spatial intermittency reaching up to $C_1 \approx 0.5$ are often found in the relevant literature, but they should be associated with on-off (rain/no-rain) intermittency and hence not present here where only the scaling inside rainy regions is considered.

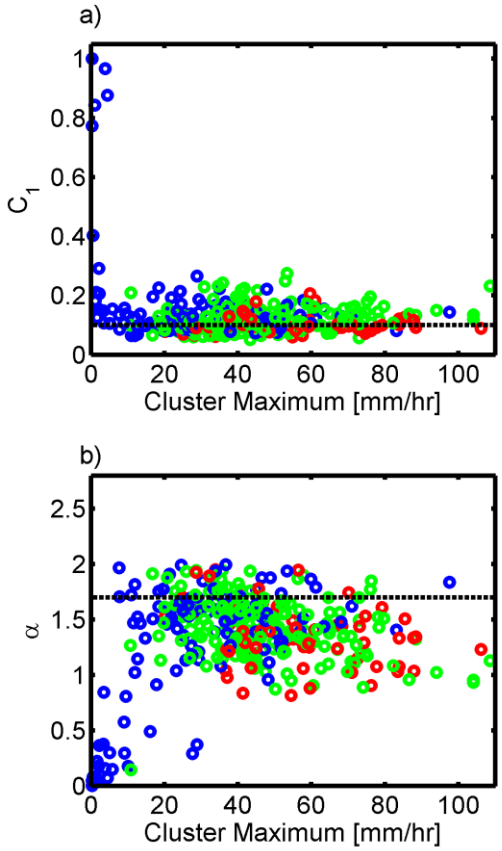

Figure 3.10 *UM parameters a) C_1 and b) α against the cluster maximum intensity value. Stratiform, convective and mixed cases are respectively identified by blue, red and green markers.*

3.4 Fractal dimension of the rain support

It was shown in the previous section that the presence of large portions of zero values in the rain fields deforms the scaling behavior, and consequently the scaling analysis should be performed inside CRFs. However, this analysis neglects the important question of the on-off intermittency that is crucial in rainfall. The rain support is a binary field and hence its scaling behavior can be evaluated using a simple box-counting method (e.g. Lovejoy et al., 1987). Recall that the measured zero values associated with the particular instrument and measuring technique are indistinguishable from the actual zero values in the rain fields, and hence they are treated equally

as field zeroes. For any given object embedded in a D-dimensional Euclidean domain of size L^D, the number of D-dimensional boxes of size l^D required to cover the object can be expressed as:

$$N = c_L \left(\frac{L}{l}\right)^{D_f} \tag{3.6}$$

where D_f is the fractal dimension of the object and c_L is an adimensional coefficient which depends on L and the shape of the object. Here we focus on the 2-dimensional embedding space case, D=2, but the results can be easily generalized to other dimensions. The area, A, of the structure can be estimated from the N associated with l^2 sized boxes:

$$A = \lim_{l\to 0} Nl^2 = \lim_{l\to 0} c_L L^{D_f} l^{2-D_f} \tag{3.7}$$

When the object is itself 2-dimensional, then D_f=2 and the expression reduces to $A = \lim_{l\to 0} c_L L^2$. It can be shown that this expression is valid for the usual (nonfractal) 2-dimensional shapes or linear compositions of them, as long as c_L is chosen appropriately depending on the size of the embedding space L and the geometrical shape[‡]. However, when the dimension of the object is a non-integer value ($1<D_f<2$) the area will depend on the measurement resolution. For a single scaling field the parameters D_f and c_L are constant with scale and consequently better suited to characterize the object geometry. These parameters can be estimated from the slope of the log-log plot of N against L/l:

$$\log[N] = -D_f \log(l) + D_f \log(L) + \log(c_L) \tag{3.8}$$

The rain fraction at resolution λ is the number of boxes necessary to cover the rain support divided by the total number of boxes in the domain ($N_T = \left(\frac{L}{l}\right)^2$) and can be related to D_f by:

$$f_R = \frac{N}{N_T} = c_L \left(\frac{L}{l}\right)^{D_f-2} \tag{3.9}$$

which can be re-written as:

[‡] For example for a square of side s we have $c_L=[s/L]^2$, which in the particular case s=L becomes $c_L=1$. If L is the side of the smallest bounding box for a triangle or a circle, then c_L is respectively 1/2 or $\pi/4$. For larger L values, c_L will be proportionally smaller.

$$D_f = 2 + \frac{\log(f_R) - \log(c_L)}{\log(L/l)} \tag{3.10}$$

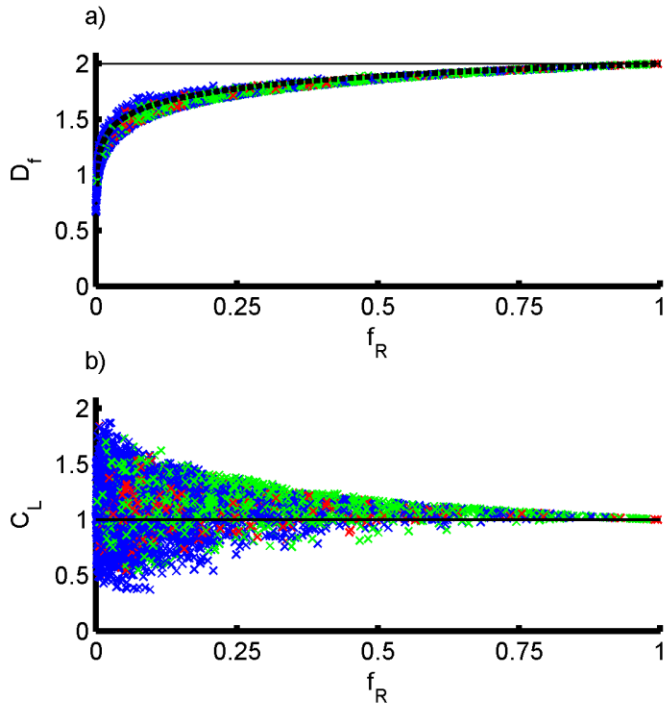

Figure 3.11 *a) Fractal dimension D_f and b) c_L of the rain support against the respective rain fraction f_R. Markers represent empirical estimates using box-counting methods and black line represents theoretical values obtained from Eq. 3.10 assuming c_L=1. Stratiform, convective and mixed cases are respectively identified by blue, red and green markers.*

This implies that f_R computed at a certain resolution will be a function of D_f and c_L. Consequently, for a rainfall field measurement at a particular resolution in a particular domain, there will be a corresponding value of D_f, which will be a good estimate as long as $L/l \gg 1$. This is illustrated in Fig. 3.11a that shows the estimated D_f values for each realization against the respective f_R at 1 km resolution. Red markers represent convective cases, blue represent stratiform, and green represent mixed cases, all falling under the same dependency curve. Fig. 3.11b shows the estimated c_L values for each realization against the respective f_R at 1 km resolution. For higher f_R values, i.e. domain filling rain supports, there is an expected tendency of $D_f \to 2$ and $c_L \to 1$, while for low f_R there is more variability in c_L. Recall that fractal constructions that are built starting from a space filling line, square or cube, such as the Cantor

set, the Sierpinsky carpet or the Menger sponge have c_L equal to unity[§]. Assuming that the support of surface rainfall is built by transformations (including thresholding) of space filling fields such as atmospheric water vapor, temperature and wind (although it has non-space-filling fields at intermediate steps, such as cloud water and rain water) one can hypothesize that for surface rainfall fields c_L=1. This hypothesis is grounded in the behavior illustrated by the thick black dashed line in Fig. 3.11a computed from Eq. 3.10 with c_L=1, that displays a very close fit to the empirically computed fractal dimensions. Hence, the large variability in c_L values can be attributed to estimation difficulties for small nonzero data amounts far from the $l \to 0$ limit. In summary, the rain support is itself fractal with a D_f value that depends on the concurrent atmospheric conditions and forcing. Theoretical *a priori* determination of D_f for particular atmospheric conditions and forcings has not been obtained yet.

3.5 Spatial downscaling

The fact that stochastic scale invariant behavior is a good approximation even when single realizations are considered makes it a very attractive and promising tool for constraining downscaling and sub-grid parameterization applications. In this section, we leverage this tendency to perform spatial downscaling of seven years of hourly Stage IV rainfall fields from their original 4 km resolution to the 1 km resolution grid of IPHEx. Based on previous works of Bindlish and Barros (1996) this can be achieved by generating a modified fractal Brownian surface (fBs) with the desired fine resolution, number of grid points and correct spectral exponent and use it as an interpolation surface. This methodology preserves the known coarse resolution portion of the power spectrum, extrapolating it to sub-grid scale wavenumbers using the correct spectral slope and amplitude. Thus, one can obtain a higher-resolution downscaled version of the field that preserves the spatial structure and correct scale invariant behavior, with coherent variability at the fine scales as schematically illustrated in Fig. 3.12. The preservation of the exact coarse resolution information can be obtained by normalizing the fBs by a coarse resolution version of itself at the same resolution as the original coarse data (see Rebora et al.,

[§] The Cantor set starts from a 1-dimensional space-filling line and has $[D_f \approx 0.63; c_L = 1]$, the Sierpinsky carpet starts from a space-filling square and has $[D_f \approx 1.89; c_L = 1]$, and the Menger Sponge starts from a space-filling cube and has $[D_f \approx 2.73; c_L = 1]$.

2006 for details). This approach requires *a priori* knowledge of the "correct" spectral slope β which is not a trivial problem due to the transient nature of the rainfall scaling parameters, as shown in Section 3. The simplest approach is to assume a universal ensemble scaling parameter, estimated as $\beta_{Ens} \approx 1.9$ from 3 years of hourly rainfall fields at 1 km resolution and over the Southern Appalachians region obtained in Section 3. This fixed (ensemble) spectral slope value assumption is applied to generate the downscaled product, hereafter referred to as StageIV_FF.

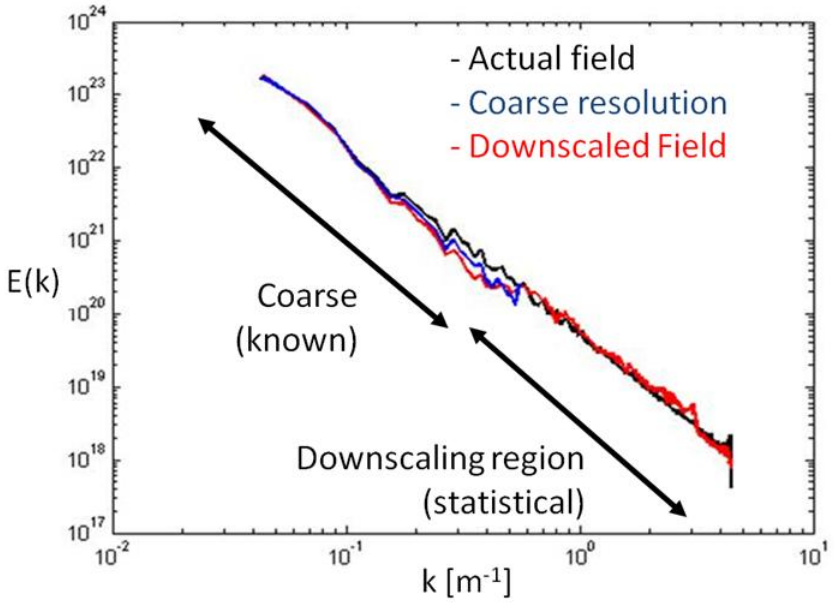

Figure 3.12 *Schematic representation of the modifield fractal interpolation. The blue line represent a coarse scale measure of the original field (black line). If the correct spectral slope is known, it is possible to generate sub-grid scale information that is statistically coherent with the original field to obtained a downscaled field (red line).*

Another downscaling product, StageIV_TF, is created taking into consideration the previously discussed transient nature of the scaling parameters of rainfall fields. Here we apply simple least-square regression on the log-log power spectra computed from the original coarse resolution Stage IV data to estimate β for each single realization to be downscaled, i.e. each hourly rainfall field, since well-defined quantitative expressions to determine the scaling parameters from system state and forcing haven't been established due to their complex nonlinear nature and dependencies on local weather and terrain conditions (as discussed above and in Nogueira et al.,

2013). The fact that Stage IV data corresponds to a large high-resolution grid (179 × 153 grid points at 4 km resolution) allows for robustness in these spectral slope estimates. For both StageIV_FF and StageIV_TF rainfall fields, 50 realizations of the downscaling fields are generated for each hourly rainfall field, from 50 different fBs (all with the same spectral slope).

Note that the described fractal interpolation methodology by itself does not create any new zeroes in the downscaled field, which is not realistic as shown if Section 3.4. A correction to generate new zeroes is to add a thresholding operation to the downscaled field, where all values below a certain threshold are set to zero. This method has been employed in the past with good performance in replicating the number of zeroes in the high-resolution fields (Perica and Foufoula-Georgiou, 1996; Rebora et al., 2006; Lovejoy et al., 2008; Verrier et al., 2010; Gires et al., 2012). Specifically a threshold value of 0.1 mm/hour which showed good performance in reproducing the number of zero pixels in high resolution fields on preliminary tests. A third downscaled dataset is obtained by simple bilinear interpolation of the hourly 4 km resolution StageIV rainfall fields into a 1 km grid, referred to as StageIV_Bilinear. Finally, StageIV_Ne product is generated using a nearest-neighbor search algorithm.

3.5.1 Error analysis

If a model is to generate realistic rainfall fields it should reproduce the observed scale invariant behavior. Based on this concept a possible verification of the downscaled datasets is to investigate the ability of interpolated fields to reproduce the expected scaling behavior according to the observations, assuming that the mean scaling behavior found in StageIV data 4 km resolution extends down to the 1km resolution, which is supported by relevant literature.

The intercomparison between the spectral exponents computed from downscaled products and from the 4km resolution Stage IV, β_{STIV} for five years of simulations is shown in Fig. 3.13. The smoothing introduced by the bilinear interpolation method causes a large drop in the variability at the smallest-scale, breaking the linear scaling behavior and causing an abrupt increase in the estimated spectral slopes, often reaching unphysical $\beta > 3$ values. The use of $\beta_{Ens} = 1.9$ at all times causes the downscaled spectra to display scaling exponents around this ensemble value, which is unrealistic in single realizations where the observations show clearly lower or higher slopes. The nearest neighbor results in spurious effects at the small scales that caused the spectral

slope to fluctuate mostly in the β~1-1.5 range of values, unable to reproduce the observed variability of the scaling behavior. The errors in the spectral slopes can be quantified by computing the Mean Absolute Error between downscaled and original Stage IV fields ($MAE = (1/N)\sum|\beta_{Dws} - \beta_{STIV}|$) resulting in values of 0.25 for StageIV_TF, 0.38 for StageIV_FF, 1.18 for StageIV_Bi, and 0.35 for nearest neighbor. These results are valid for cases where the linear regression coefficient estimation is R^2>0.98 for the original dataset, hence where variability should correspond to a physical transient behavior of the scaling exponents and not associated with problems in the estimation of the spectral exponent. It becomes clear that the use of β_{Ens} is not a good approach generally, and that the transient nature of the scaling exponent should be taken into account. Consequently, StageIV_TF product is a better approximation to the real scaling behavior of the observed rainfall fields and in fact the only product capable of capturing the observed variability of the scaling exponent.

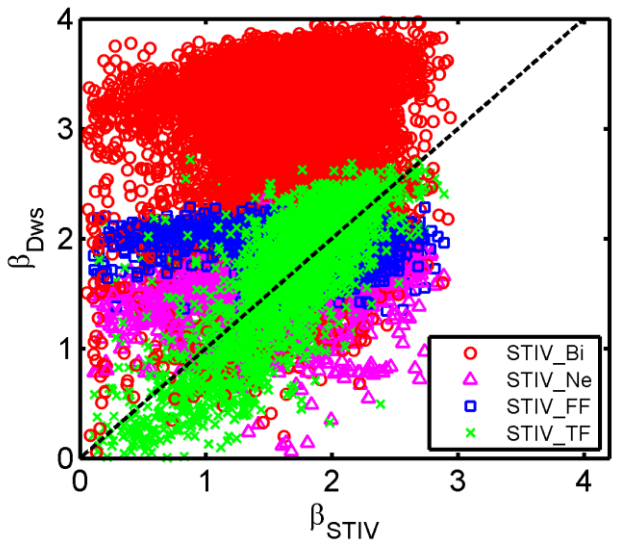

Figure 3.13 *Downscaled spectral exponent against observed (Stage IV) spectral exponent of hourly single-realizations of rainfall fields, red, blue and green markers represent respectively StageIV_Bi, StageIV_FF and StageIV_TF. Pink markers represent a nearest neighbor interpolation of original StageIV at 4 km resolution to 1 km resolution.*

The average probability density function (PDF) of the downscaled rainfall intensity during the five year period is evaluated against the empirical statistics determined for the raingauges in the Pigeon River Basin region (identified in Fig. 3.1b), using nearest pixel approximation to obtain

point values over the raingauge locations. All downscaling products show clear underestimation of the low intensity (< 5 mm/hr) precipitation frequency (Fig. 3.14) due to limitations in the algorithms used to estimate rainfall from radar measurements for StageIV products. Note that this is likely to cause problems for water budget studies as light rainfall represents a substantial part of the water cycle (Wilson and Barros, 2014). For intermediate intensities, all products show good reproduction of the raingauge observations, particularly considering that comparison is between point measurements and 1km resolution gridded data. The point-to-pixel scale gap should also be responsible for the general PDF underestimation at the highest intensities for all gridded products. Bilinear interpolation causes the largest underestimation as expected by its smoother character. Also, the smoothing introduced by the ensemble averaging operations in StageIV_FF and StageIV_TF products introduces a frequency decrease at the highest intensities, as it can be seen by comparing the results against a randomly chosen single realization out of the 50 realizations available at each time step (light blue and pink lines). The results for StageIV_TF show a slightly better ability to represent the probabilities of high intensity rainfall values than StageIV_FF, providing further support for the transient character of the scaling behavior.

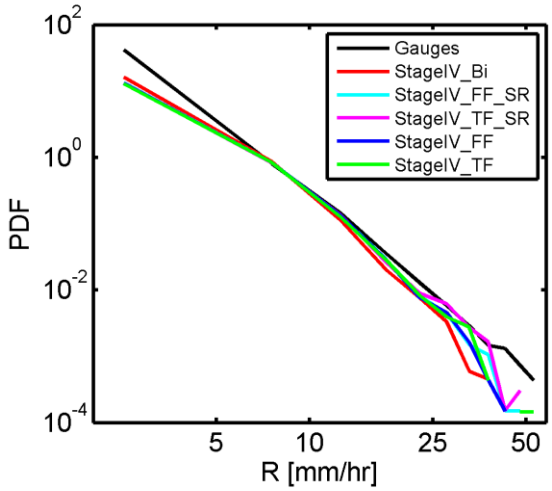

Figure 3.14 *Intercomparison of probability density function (PDF) over the PRB raingauges (identified in Fig. 1) point locations during the five year period. Black line is computed from local raingauge data and the other lines corresponded to 1km resolution downscaled products. StageIV_FF_SR (light blue) and StageIV_TF_SR (pink) represent the statistics for a randomly chosen single realization (out of the 50 available) at each time instant. For 1km downscaled products nearest pixel approximation is used to obtain point values over the raingauge locations.*

Finally, notice that considering only time instants when the rain fraction in the original StageIV data is greater than 10%, the StageIV_TF spectral slopes vary in the [1.6, 2.5] range with mean 2.0 for the winter 2009 event, while the β values were in the [1.2, 2.6] range with mean 1.7 for the summer 2008 tropical storm. The decrease of the spectral slope to values around 5/3 for a summer tropical convective storm compared to a stratiform winter case with spectral slope closer to 2 is in agreement with the findings of Nogueira and Barros (2014) on the transition of the scaling behavior between non-convective and convective situations, providing further evidence into the importance of considering the transient nature of the scaling behavior.

3.5.2 Hydrological Applications

To illustrate the utility of the fractally downscaled rainfall products in hydrologic studies, streamflow simulations were conducted in the PRB (Pigeon River Basin) using a physically-based fully-distributed hydrological model (3D-LSHM) forced by StageIV_TF, representing the fractal method that better reproduced the observed statistical structure, and also the bilinear product (StageIV_Bi), representing a commonly used method for rainfall downscaling in hydrological applications. Two particular events were selected for detailed analysis. One is Tropical storm Fay in August of 2008 which caused extensive flash floods in the basins and has been investigated in a previous study using the same hydrologic model at very high resolution (250m and 5min) (Tao and Barros, 2013). The other is a winter storm causing debris flow events in the Pigeon River Basin for which the initiation mechanism has been investigated using the same hydrological model (Tao and Barros, 2014a). Note that the 3D-LSHM is uncalibrated and without manual tuning against the observations, because our goal here is to demonstrate the uncertainty in hydrological simulations induced by rainfall input datasets. Detailed description of the hydrological simulations can be found in Tao and Barros (2014b,c).

Figure 3.15 shows streamflow simulations results in operational-like mode over the West Fork Pigeon River Basin (WFPRB, see Fig. 3.1b) for the two selected storm events forced by different rainfall products generated from the original StageIV QPE at 4 km resolution, including 50 realizations of StageIV_TF at 1 km resolution (blue lines in Fig. 3.15a and Fig. 3.15c), the corresponding ensemble average rainfall products (green lines), and also the bi-linearly interpolated rainfall product (red lines). Overall both hydrological simulations forced by the

fractally downscaled products exhibit good skill against the observed hydrograph (black lines in Fig. 15) especially with regard to the timing and magnitude of peak discharge. The performance of the fractal downscaled products quantified using the Nash-Sutcliffe efficiency (NSE) of the streamflow for both events is summarized in Table 3.1. The NSE scores are high for all simulations and substantially higher (closer to 1) for StageIV_TF, indicating better predictive power consistent with expectations based on the error analysis results in the previous section. For the winter storm case the fractal downscaling results in NSEs very close to unity with well captured time-to-peak and peak flow values of the hydrographs (Fig. 3.15c). For the Tropical Storm event (Fig. 15a), while the timing and shape of the stream flow peak are well reproduced by both fractal downscaling methods, the ensemble products underestimate peak intensity and overestimate the streamflow recession, explaining the decrease in NSE. The lack of skill in reproducing the falling limb of the observed hydrograph may be associated with the specified soil moisture and water table initial conditions and, or the uncalibrated parameters in the hydrological model, and not with the rainfall forcing per se (see discussion by Tao and Barros 2013, 2014a).

Simulation Period	**Basins**	**Rainfall dataset**	**NSE**
Aug. 25 – 28, 2008	WFPRB	StageIV_Bi	0.65
		StageIV_TF	0.77
Jan. 5 – 10, 2009	WFPRB	StageIV_Bi	0.78
		StageIV_TF	0.89

Table 3.1. *Summary of NSE for hydrological simulations.*

For the small resolution gain (4:1) between the original 4-km resolution and the IPHEx grid 1-km resolution, the resulting spread in the simulated streamflow ensemble is narrow (blue lines in Fig. 15a and Fig. 15c). Nonetheless the obtained variability is important since the single realization solutions are able to attain higher streamflow peaks, closer to the observations, due to the absence of the additional smoothing caused by ensemble averaging. The span of solutions does in fact extend closer to the streamflow peak in the 2008 summer storm than when the

ensemble product is used. A larger spread of hydrograph solutions was obtained when a larger resolution gain (16:1) was achieved by downscaling StageIV QPE from 4-km to 250m grid spacing (Fig. 15b and Fig. 15d). At this finer resolution, the observed streamflow peak is always within the 50 possible solutions obtained using both fractal products, while using the ensemble rainfall products results in underestimation of the streamflow peak for both winter and summer storms.

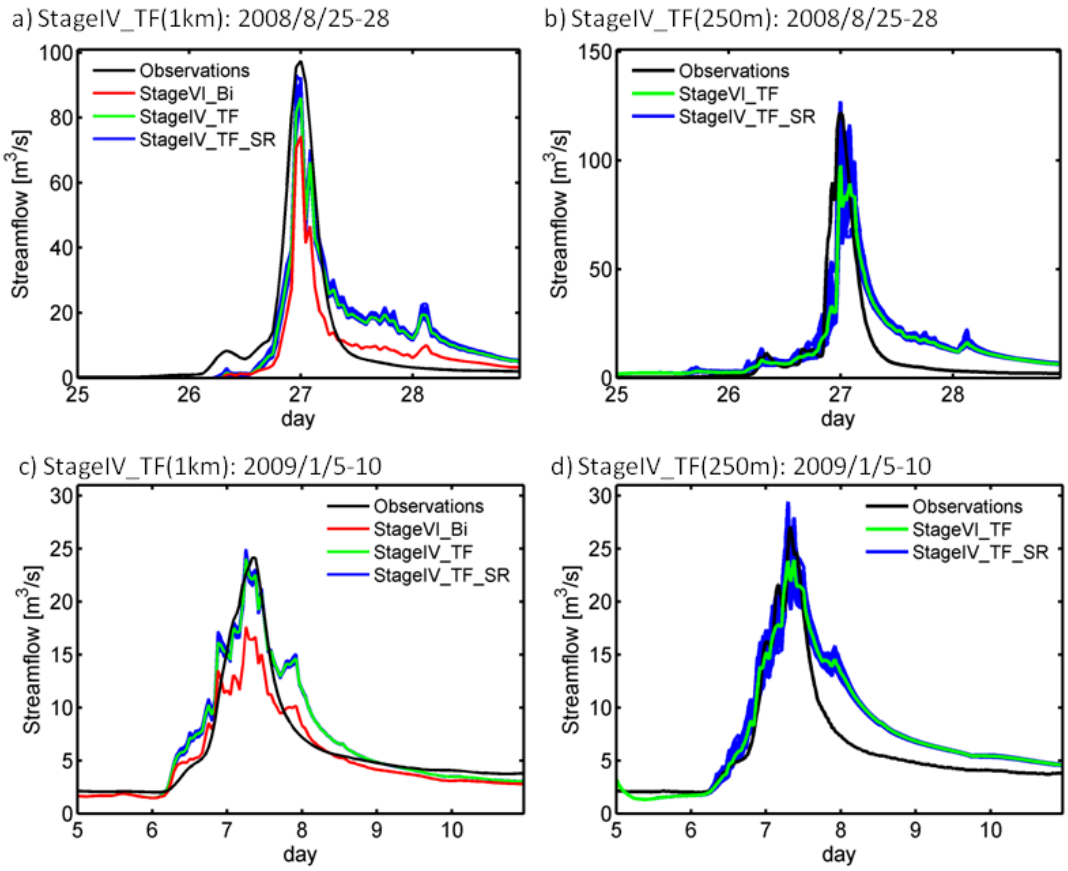

Figure 3.15 *Examples of streamflow simulation in the WFPRB forced by StageIV_TF at 1km resolution data for a) summer event (Tropical Storm Fay) in 2008 and b) winter storm in 2009, and forced by StageIV_TF at 250 m resolution for c) summer event (Tropical Storm Fay) in 2008 and d) winter storm in 2009. Black lines represent observed streamflow. Blue lines represent the span of plausible solutions generated by using each single member of the ensemble of fractally downscaled fields as rainfall forcing. Green lines represent solutions of simulations forced by the ensemble averaged rainfall field generated by fractal method. Redlines represent the solution forced by bilinear interpolated rainfall fields.*

Further evidence to the advantages of the fractal downscaling method presented here can be found in Tao and Barros (2014b and 2014c) who used StageIV_FF and StageIV_TF 1 km resolution products to force a 5-year (2007-2011) continuous simulation using the same uncalibrated hydrologic model over the PRB, with significant overall increase of the NSE for all types of rainfall events and various basins when fractal methods are used compared to bilinear and nearest neighbor interpolation. Additionally, the performance for the fractal downscaling results here is similar to results reported by Tao and Barros (2013, 2014a) using a locally optimized precipitation product by merging observations from a dense raingauge network, which is not included in the Stage IV products. This further gives credence to the robustness of the fractal interpolation methods.

3.6 Conclusions

Radar derived QPE fields display spatial stochastic (multifractal) scale-invariance over a wide range of scales (from ≈ 1 km up to 100's km). However, this scaling behavior is deformed by the presence of large fractions of zero rain values, causing breaks and curvature to the log-log linear spectral relations. One way to account for this deformation is to consider only rainfall fields with high f_R (low zero fractions). When the domains have large spatial extent, such as the IPHEx domain over the SE US considered here, choosing only high f_R cases can bias the analysis towards large MCSs and synoptic-scale systems, potentially neglecting more localized precipitation features such as summertime orographic convection. An alternative method is presented here that relies on a spatial cluster identification algorithm to isolate (nonzero) CRFs, inside which the spatial scaling behavior displays remarkable multifractal behavior, with ensemble scaling parameters $\beta \approx 1.9, C_1 \approx 0.1, \alpha \approx 1.9$ and $H \approx 0.5$, similar to the asymptotic parameters found here when $f_R \to 1$, also reported by Verrier et al. (2010).

When scaling analysis is performed on single realizations of hourly rainfall fields, the results show important deviations from the ensemble scaling behavior, with β values varying essentially in the [1.5, 2.5] range. This implies that the multifractal properties of rainfall fields are transient properties with variability that cannot be attributed to spurious effects associated with small nonzero data samples or zero, and deformation of the scaling by the presence of large portions of

zero rainfall values. Instead, there is a complex nonlinear interdependence on the particular atmospheric conditions and terrain forcing as argued by Barros et al. (2004), and in agreement with the conclusions of Nogueira et al. (2013). It is also important to note that this type of analysis on rain clusters circumvents the on-off intermittency in rainfall fields. Interestingly, it is shown that the binary rain support is itself fractal, with fractal dimension that is by definition tightly related to the fraction of rainy pixels, f_R.

The scaling behavior of rainfall fields is a promising path for stochastic downscaling required to bridge the gap between observed and simulated rainfall and the high-resolution requirements of many hydrometeorological applications. Here, this approach was investigated by downscaling 7 years of hourly Stage IV rainfall fields at 4 km resolution to the 1km resolution IPHEx grid using fractal interpolation methods in the Fourier domain. Two types of downscaled fractal products were generated: one considering a fixed value of the scaling exponent estimated from the ensemble analysis (StageIV_FF), and a second using a transient spectral exponent estimated from each coarse resolution realization of the rainfall field (StageIV_TF). Both methodologies are able to rapidly generate large ensembles of high resolution statistically robust fields without any additional data or calibration requirements, conserving the coarse resolution information and generating coherent small-scale variability and statistics, hence adding value to the original field. It is important to note that the cross-scale conservation of the original statistical structure from the coarse resolution information implies that the errors in these forcing datasets are propagated into the downscaled fields, such as the tendency of the radar derived StageIV QPE to underestimate low intensity rainfall or NWP (Numerical Weather Prediction) forecast errors for example. Such issues should be resolved prior to downscaling and not by the downscaling methodology itself.

The downscaled fields using transient estimation of the spectral scaling exponent result in better coherence between the subgrid scale statistical structure and the respective coarse resolution information when the scaling deviates significantly from $\beta_{Ens} = 1.9$ behavior. Additionally, StageIV_TF captures the high intensity rainfall statistics more accurately than StageIV_FF, providing further support to the transient nature of the scaling behavior. Consequently StageIV_TF was chosen as representing the best fractal downscaling method and used to force hydrological simulations over the Pigeon River Basin in the Southern Appalachians. The

hydrological simulations forced by the 1 km resolution ensemble averaged fractal downscaled fields overperformed the commonly used bilinear interpolation as expected. Non-fractal interpolation methods are unable to reproduce the subgrid-scale variability resulting in significant shortcoming in predicting extreme rainfall events associated with localized features, though the specific impact on skill metrics will necessarily depend on basin scale and geomorphic properties as well as the storm system proper. The results also show that the smooth character of the ensemble downscaled rainfall products resulting from averaging over several realizations cause an underestimation of the peak streamflow, particularly relevant for flashflood causing events extreme rainfall events such as the 2008 summer Tropical storm Fay case studied here. A more informative stochastic streamflow prediction was obtained by considering all the hydrological simulations forced by each of 50 single realizations of the fractal downscaled rainfall, that is an ensemble of hydrological simulations. The resulting spread of solutions was better capable of capturing the observed intense streamflow peaks. Further improvement to the streamflow solution spread was obtained by increasing the downscaling resolution to 250 m, clearly demonstrating the high-resolution requirements of hydrological applications and the utility of fractal downscaling to meet these requirements. At 250 m resolution the observed streamflow associated with both storms was captured by the 50 member ensemble of stochastic streamflow forecasts generated from StageIV_TF. Note that the generation of ensembles is computationally inexpensive and does not require human interference or judgment and the fractal downscaling can be ran fully automatically. The applications reported here and elsewhere (Tao and Barros 2014b,c) demonstrate that the stochastic fractal downscaled products have great potential to provide a reliable probabilistic forecast and associated uncertainty, especially for extreme events, yielding high resolution fields with short temporal latency that enables timely operational forecasts including uncertainty estimation.

Acknowledgements

The authors are grateful to Jing Tao for running the hydrological simulations used in this investigation. The work was supported by NASA grant NNX13AH39G and the first author was also supported during part of this investigation by Portuguese Foundation for Science and

Technology (FCT) under grant SFRH/BD/61148/2009. The 7 years fractal downscaled rainfall products in IPHEx domain (represented in Fig. 1) as well as original StageIV products are available at http://iphex.pratt.duke.edu.

4 The non-convective/convective structural transition in stochastic scaling of atmospheric fields**

Abstract

High-resolution (Δs =1.2 km, where Δs is the grid size) NWP (Numerical Weather Prediction) simulations are able to reproduce observed stochastic scale-invariant behavior of atmospheric wind and water fields down to the effective model resolution. Here, it is shown that the effective resolution is a process-dependent transient property that varies in space and time with the underlying dynamics. Generally, in the absence of convection, effective resolutions remain around 4-5Δs. However, when convection is active, the effective resolution decreases to scales around 10-15Δs where a transient scaling break emerges splitting the large-scale behavior in close agreement with observations from a small-scale regime with an abrupt (unphysical) steepening of the spectral slope. Consequently, the effective resolution gain in numerical downscaling of convective regimes is substantially smaller than the grid-size decrease (~2:5-fold difference in the simulations analyzed in this study) indicating that improvements in the model's capacity to resolve small-scale processes require consistent adjustments including both numerical formulation and physical (i.e. process-oriented) parameterizations.

Instantaneous realizations of simulated atmospheric wind and water fields exhibit robust multifractal properties with intrinsically transient scaling behavior depending on the underlying atmospheric state. In particular, a sharp transition in the scaling parameters between non-convective and convective conditions is found, which explains different scaling regimes often reported in the literature for atmospheric wind, temperature and moisture observations. Spectral slopes around 2-2.3 arise under non-convective or very weak convective conditions, tightly

** Nogueira[(1,2)], M. and Barros[(2)], A. P., 2014: The non-convective/convective structural transition in stochastic scaling of atmospheric fields. Submitted to J. Geophys. Res.

(1) CGUL-IDL, University of Lisbon, Portugal.

(2) Duke University, Durham, North Carolina, U.S.A.

related to the scaling behavior of the underlying topography. In convective situations the transient scaling exponents remain under 5/3 in agreement with the Kolmogorov turbulent regime accounting for the intermittency correction. The non-convective/convective transition is also unambiguously captured by the temporal evolution of the multifractal intermittency parameter. This finding has important implications for stochastic downscaling and the implementation of stochastic sub-grid scale parameterizations using fractal methods. Specifically, it is shown that, based on scaling arguments, sub-grid scale probability distributions of atmospheric moisture can be obtained from the coarse resolution information alone. Moreover, fractal methods directly generate an ensemble of distributions describing sub-grid scale statistics, and thus their associated uncertainty. Results obtained by imposing the 2.1 or 5/3 scaling in the fractal interpolation algorithm as a first approximation to the transient scaling parameters, depending on whether the downscaled field is respectively stratiform or convective, capture the sub-grid scale statistics of isotropic cloud fields well. This suggests that this approximation can be used for estimating regime-based sub-grid scale statistics in a computationally efficient manner, and in particular when the scaling cannot be derived from limited-area coarse resolution fields.

4.1 Introduction

The geometry and orientation of topographic features dynamically modulates synoptic-scale systems by a broad variety of physical mechanisms, including orographic uplift, blocking, differential heating, moisture convergence, convective triggering and gravity waves (see e.g. Barros and Lettenmaier, 1994; Roe, 2005; Smith, 2006; Houze, 2012 for reviews). Stationary orographic forcing has been shown to dominate the hydroclimatology over massive mountainous regions at climate scales and can give rise to some of the most extreme rainfall intensities and gradients at weather time-scales (e.g. Barros and Lettenmaier, 1994; Lang and Barros, 2002; Barros and Lang, 2003; Garreaud et al., 2003; Barros et al., 2004, 2006; Roe, 2005; Zipser et al., 2006; Bhusan and Barros, 2007; Giovanettone and Barros, 2009; Romatschke and Houze, 2010; Rasmussen and Houze, 2011; Houze, 2012). The resulting rainfall fields are modulated over wide ranges of spatial and temporal scales by numerous non-linear interactions giving rise to

complex orographic cloud and rainfall spatial patterns with variability over a wide scale spectrum (Harris et al., 2001; Barros et al., 2004, 2006; Nykanen, 2008; Nogueira et al., 2013).

Intensive research efforts undertaken over the past 30 years have yielded vast evidence of the presence of stochastic scale-invariant behavior over wide ranges of scales in different geophysical fields, including hydrometeorological variables such as rainfall, clouds, water vapor and soil moisture (see e.g. Veneziano et al., 2006; Lovejoy and Schertzer, 2007; Tuck, 2010 for reviews). Early works of Nastrom and Gage (1985) and Nastrom et al. (1986) documented the horizontal scaling behavior in atmospheric kinetic energy, temperature and humidity spectra derived from airborne observations, extending from lengths of a few kilometers up to 400-500 km, with spectral slopes close to the 5/3 prediction of Kolmogorov (1941) for turbulent wind fields and Corrsin-Obukhov (Corrsin, 1951) for passive scalars. Similar results were reported by several subsequent studies (see e.g. Tuck, 2010 for a review). However, while the scaling behavior does in fact seem to be a ubiquitous property of atmospheric and geographical fields, there are several reasons to question the universal 5/3 spectral slope predicted by classical turbulence theory for atmospheric wind and water fields. First, these theoretical models assume isotropic scaling behavior which is impossible in the real atmosphere across wide ranges of scales due to the strong vertical stratification caused by gravity (e.g. Schertzer and Lovejoy, 1985; Lovejoy and Schertzer, 2010b). Second, the water in the atmosphere should not often behave as a passive scalar since water transformations interact with atmospheric motions, and directly affect the energy balance playing an important role in heat transport, radiative processes and convective motions (e.g. Emanuel, 1994). Third, in many prior studies the spectral slopes estimates are based on visual comparison of the spectra against a reference 5/3 line, rather than explicitly computing scaling exponents. Finally, most of these observational studies are based on aircraft measurements covering an inherently limited range of spatial-temporal scales (i.e. the flight length), thus sampling a very small portion of the large continuously evolving atmosphere, and analyze the ensemble scaling behavior of different realizations neglecting the variability in the spectra in the dynamically evolving atmosphere.

Whether scaling parameters for a given atmospheric field are universal (constant) or instead dynamically dependent on the particular atmospheric and forcing conditions is an open scientific question. There is an increasing body of literature reporting significant deviations from the 5/3

scaling and significant dynamical variability on the estimated scaling exponents for kinetic energy, temperature and atmospheric water spectra. In particular β values around 2 are often reported over the mesoscales for high-resolution observations of wind, humidity and temperature (e.g. Lovejoy et al., 2004; Tuck et al., 2004; Tuck, 2008; Lovejoy et al., 2010a; Tuck, 2010), a scaling regime for which no satisfactory theoretical explanation is available. Furthermore, linkages among the scaling parameters to specific regions, forcing regime and atmospheric conditions generally have been reported for wind, water and temperature fields (e.g. Barros et al., 2004; Tuck, 2008; 2010; Khan and Teixeira, 2009; Khan et al., 2011; Pressel and Collins, 2012; Nogueira et al., 2013). For the particular case of rainfall fields, there is an even broader range of investigations not only documenting variability of the scaling parameters, but also unambiguous dependencies on the particular synoptic conditions (Over and Gupta, 1994; Douglas and Barros, 2003; Nogueira and Barros, 2014), underlying topography (Douglas and Barros, 2003; Barros et al., 2004; 2006; Nykanen, 2008; Nogueira et al., 2013), atmospheric stability (Perica and Fofoula-Georgiou, 1996; Nogueira et al., 2013), microphysical terminal velocity (Parodi et al., 2011) and mean wind speed (Nogueira et al., 2013). However, no universal relations among scaling parameters and geophysical properties have been established to model these dependencies, mostly due to the complex nonlinear interdependence of several atmosphere and land variables (e.g. Nogueira et al., 2013).

Numerical Weather Prediction (NWP) and global climate models (GCMs) should reproduce the observed scaling behavior if they are to realistically represent atmospheric fields and their dynamical evolution. This requirement provides a useful metric for evaluation of numerical models performance. Encouraging results were found for GCMs and NWP models in the reproduction of the ensemble kinetic energy scaling over broad ranges of scales (see e.g. Koshyk et al., 1999; Koshyk and Hamilton, 2001; Skamarock, 2004; Takashi et al., 2006; Hamilton et al., 2008; Stolle et al., 2009; Terasaki et al., 2009). Yet, despite the potential utility of the observation of scale invariance in numerical models, few studies have performed quantitative estimation of the simulated scaling parameters and the ability of numerical models to reproduce the observed scaling of atmospheric water content variables. Zepeda-Arce et al. (2000) investigated the scaling of quantitative precipitation forecasts from NWP and found a spatial multiscale structure similar to that observed. Harris et al. (2001) reported encouraging results comparing the scaling behavior from single realizations of NWP modeled precipitation fields at

3-km resolution against weather radar observations. Kahn et al. (2011) evaluated the scaling of water vapor in free-running GCMs in comparison with satellite observations and found that the simulated fields did show scaling behavior, but displayed steeper slope exponents. Finally, Parodi et al. (2011) and Nogueira et al. (2013) showed that cloud and rainfall fields in high-resolution idealized simulations of orographic convection were able to reproduce the main features of observed scaling, despite the design simplicity of the experimental design.

In the present work, transient scaling behavior and its implications for stochastic downscaling/parameterization is investigated by focusing on tropical deep convection events occurring over the central Andes in South America. The interaction of the incoming moist unstable flow with orography can bring the air parcels well above their level of free convection, hence creating the conditions for triggering and enhancement of deep convective orographic structures capable of generating large rainfall amounts (Virji, 1981; Paegle et al., 1987; Campetella and Vera, 2002; Ferreira et al., 2003; Wang and Fu, 2004; Liebmann et al., 2004; Vera et al., 2006; Romatschke and Houze, 2010; Barros 2013; Sun and Barros 2014, Mohr et al, 2014). The dynamical evolution of the multifractal properties of atmospheric wind and water fields, and in particular the transition between the statistical scaling behavior under convective and non-convective regimes is investigated, building on the previous findings of Nogueira et al. (2013) of an abrupt transition in scaling properties of cloud and rainfall in highly idealized simulations of orographic precipitation. Here this result is generalized to fully realistic simulations capable of reproducing the main features of the atmosphere, over a considerably large domain at high-resolution (1.2 km) over the central Andes region, under three different scenarios throughout 24 hour periods: a dry season non-convective case where no rainfall is produced and two rainy season deep orographic convective cases under South American Low-Level Jet (SALLJ) conditions, one giving rise to very large rainfall amounts and the other generating weaker less persistent convective structures (Sun and Barros, 2014). This setup allows a rare opportunity to investigate the poorly understood dynamical dependencies of the scaling behavior of kinetic energy and atmospheric water content at the mesoscale, with particular emphasis given to the diurnal cycle and the transition between non-convective and convective events, which has received little attention despite the evidence for clearly different statistics between the two types of events (e.g. Berg et al., 2013). Further, the transient stochastic scaling analysis framework considered here allows exploring whether the numerical models are able to

capture the response of atmospheric fields to the dynamical evolution of the atmospheric state, which is a key question for weather and climate prediction (Tao and Barros, 2008).

The sub-grid parameterizations of cloud fraction currently available in weather and climate models are generally based on simplified bulk empirical formulas, making use of large-scale predictors such as relative humidity, mean condensate mixing ratio, cloud depth or convective time-scale (see e.g. Xu and Randall, 1996; Bony and Emanuel, 2001; Zhang et al., 2011 and Gianotti and Eltahir, 2014 and references therein). Recent works have shown that such methods often fail to reproduce the correct sub-grid scale cloud variability, causing well-known shortcomings to the simulated fields (e.g. Zelinka and Hartman, 2012; Randall et al., 2013; Gianotti and Eltahir, 2014). In fact, a poor representation of the sub-grid cloud fraction was identified as primary reason for differences among model predictions in the 4th Intergovernmental Panel on Climate Change Fourth Assessment Report (Christensen et al., 2007).

Recently Skamarock et al. (2012) presented a variable resolution atmospheric model that allows for variable horizontal resolution, the Model for Prediction Across Scales (MPAS). By embedding high-resolution regions on the model grid, it is possible to properly represent small-scale features such as convective cells while keeping the model computationally efficient for weather or climate and global or regional predictions. A similar concept is being used for the "superparameterization" of clouds (see e.g. Randall et al., 2013 and references therein). However, explicit representation of processes representing clouds down to the smallest scales where interaction with radiation occurs remains a great challenge, which is further complicated by the turbulent processes that affect clouds down to viscous dissipation scales on the order of the millimeters. Consequently, sub-grid parameterization of clouds over a desired scale range (albeit model dependent) is an important topic of current research. The stochastic representations of atmospheric water sub-grid probability distribution function (PDF) presented by Bony and Emanuel (2001) represent a promising path towards this goal. In their approach, the PDF of total water mixing ratio is of primary importance for sub-grid parameterization of clouds, particularly due to its direct relationship to the sub-grid cloud fraction. They considered a log-normal distribution of total atmospheric water and obtained promising results in predicting the sub-grid cloud fraction over the tropical ocean. However, it has been shown that the observed statistical

scale-invariant behavior excludes the possibility of asymptotic log-normal distributions, principally because of the non-convergence of the statistical moments for orders higher than one (Schertzer and Lovejoy, 1987; Gupta and Waymire, 1991). More recently, Gianotti and Eltahir (2014) designed a simpler algorithm based on Bony and Emanuel (2001) scheme where the cloud fraction is directly related to the mean conditional PDF of cloud liquid water estimated a priori from observations, which limits its use for highly variable weather events where the variability at all scales significantly impacts the solution. Nonetheless this methodology represented an interesting alternative to be used particularly in climate models, without any assumption for the type of total water PDF and with the advantage of being computationally very efficient.

In the present work, an alternative method of stochastic parameterization of clouds is presented that explores the scaling behavior of atmospheric fields to derive the total water sub-grid scale PDF. The considered fractal interpolation methods have been successfully applied in the past to different geophysical fields, conserving the coarse resolution information and generating coherent small-scale variability and field statistics (e.g., Bindlish and Barros, 1996; 2000; Rebora et al., 2006; Tao and Barros, 2010; Nogueira and Barros, 2014). The manuscript is organized as follows: Section 4.2 describes the numerical experiments and multifractal analysis framework used in the present study. In Section 4.3, the ability of the simulations to reproduce the main features of deep convection over the central Andes under the considered synoptic conditions is investigated. Ensemble and transient scaling analysis is presented in Section 4.4, focusing on non-convective/convective transition. The scale distribution of variability is also used to evaluate the model effective resolution for different grid-spacing lengths. In section 4.5 the implications of the scaling behavior for sub-grid stochastic parameterization of atmospheric water are investigated and a scale-invariant based PDF is obtained under convective and non-convective scenarios. The main conclusions are presented in Section 4.6.

4.2 Data and methodology

4.2.1 Numerical simulations

The non-hydrostatic and compressible numerical model advanced Weather and Research Forecasting (WRF) version 3.4.1 (Skamarock et al., 2008) was used to perform numerical simulations over South America, using three nested domains represented in Fig. 4.1, with one-way coupling between the nested domains. While it has been shown that feedback between nested domains in NWP can have important impacts on the simulated fields (e.g. Erlingis and Barros, 2014), the results of the present simulations are capable for reproducing the main features and statistical structure in the observations, as shown by Sun and Barros (2014) and also discussed below in Section 3 and Section 4. Additionally, the use of one-way coupling allows for direct comparison between the deterministic dynamical downscaling and the stochastic fractal downscaling methods presented in Section 5. The outer domain (d01) had 315 × 495 grid points at 18 km resolution covering the entire South-American continent; the intermediate domain (d02) had 432 × 603 grid points at 6 km resolution covering the central Andes region; and the inner domain (d03) had 755 × 725 grid points at 1.2 km resolution focusing in a particular region of the central Andes extending over Peru, Bolivia and Brazil and including a section of the central Andes, reaching heights over 5000 m. A high-resolution domain, hereafter referred to as HRDI, defined as a sub-region of d03 with 512 × 512 pixels to facilitate Fourier analysis will be the core study domain in this manuscript. A minimum 20 pixel distance between the lateral boundaries of HRDI and d03 is imposed in order to avoid the well recognized problems in the lateral nested boundaries in WRF. All domains had 60 vertical terrain-following σ-levels unequally distributed over the 18 km of the domain, with vertical spacing stretching from lower to higher levels. A Rayleigh damping layer was introduced at the upper 5 km to reduce spurious reflections at the top. The sub-grid scale effects were parameterized by the Yonsey University (YSU) planetary boundary layer scheme, Lin microphysics scheme and Noah land-surface model. The rapid radiative transfer model and the Dudhia scheme were respectively used to represent longwave and shortwave radiation effects. Kain-Fritsch cumulus parameterization scheme was used in domains d01 and d02, while in the high-resolution inner domain convective effects were resolved explicitly by the model.

Three different case studies were considered – the first one representing extremely dry conditions (denoted EDRY) in the austral winter of 2003, starting on July/20/2003. The other two cases represent SALLJ synoptic conditions in the rainy season (coinciding with austral summer) of 2003, during the South-American Low-Level Jet Experiment (SALLJEx, Vera et al., 2006). One represented strong intensity SALLJ conditions starting at February/6/2003 (denoted S_SALLJ) and the other represented weak SALLJ conditions on January/15/2003 (denoted W_SALLJ). All simulations were run for 36 hours starting from 0000 UTC. The considered 24-hour time period starts 12 hours after the simulation starting time, hence removing the model spin-up effects from the results (see e.g. Skamarock, 2004). For a more detailed description of the numerical simulations the reader is referred to Sun and Barros (2014).

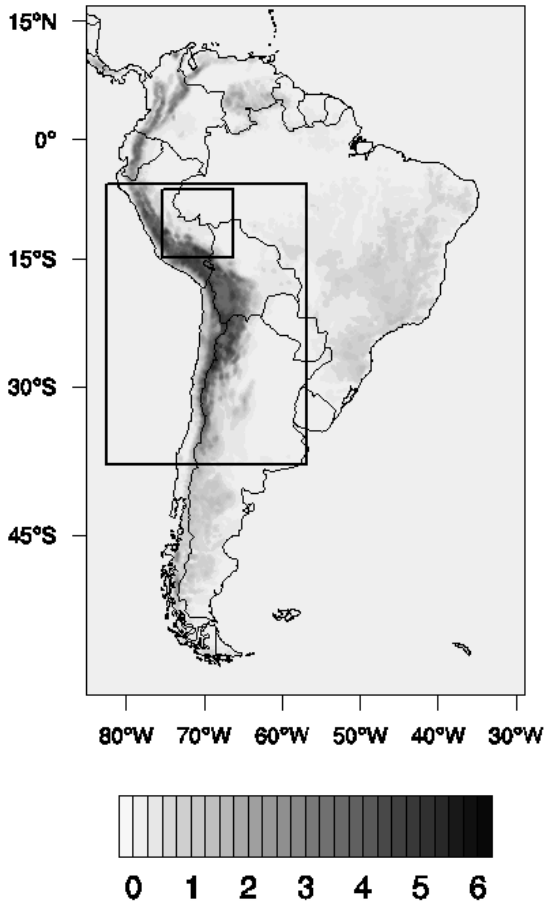

Figure 4.1 *WRF model domains with topographic height in meters (shading). The map represents the full outer d01 domain and the two inner rectangles represent the inner nested domains d02 and d03.*

4.2.2 Multifractal framework

Gravity causes strong stratification and large aspect ratio in atmospheric flows over the meso- and synoptic–scales of interest for weather and climate. This effectively rules out the existence of isotropic turbulence regimes (e.g. Lovejoy and Schertzer, 2010b) and consequently anisotropic behavior of the atmosphere must be considered with different scaling laws between the horizontal and vertical directions:

$$\Delta F(\Delta x) = \varphi_{\mathrm{H}} \Delta \mathrm{x}^{\mathrm{H_H}}$$
$$\Delta F(\Delta z) = \varphi_{\mathrm{v}} \Delta \mathrm{z}^{\mathrm{H_v}} \qquad (4.1)$$

Here, $\Delta F(\Delta x)$ and $\Delta F(\Delta z)$ represent fluctuations of a given scaling field respectively over distance lengths Δx and Δz in the horizontal and vertical directions. φ_{H} and φ_{v} are the corresponding conserved turbulent fluxes in the horizontal and vertical directions, and H_H and H_v are the respective non-conservation scaling parameter. Notice that the scale-by-scale conserved property is the turbulent flux φ rather than the field F itself, with the H values measuring the degree of non-conservation (H=0 for a conserved field). Based on classical turbulence theory, the anisotropic generalized scale invariance framework (Schertzer and Lovejoy, 1985; Lovejoy and Schertzer, 2010b) assumes that Kolmogorov (1941) scaling of turbulent velocity fluctuations holds in the horizontal direction, the conserved cascade property being the turbulent energy flux, $\varphi_{\mathrm{H}} = \varepsilon^{1/3}$ and consequently H_H=1/3. The assumption in the vertical direction is that gravitational influence on buoyancy fluxes is the dominant process, with the buoyancy variance flux being the conserved turbulent property following Bolgiano-Obukhov scaling (Bolgiano, 1959), $\varphi_{\mathrm{v}} = \phi^{1/5}$, and consequently H_v=3/5. This implies that vertical sections of structures become progressively flatter at larger and larger scales. The same H_H and H_v exponents are predicted for passive scalars, although the statistics should follow the Corssin-Obukhov scaling for passive advection where the conserved turbulent fluxes are given by $\varphi_H = \chi^{1/2}\varepsilon^{-1/6}$ and $\varphi_V = \chi^{1/2}\varepsilon^{-1/2}\phi^{1/5}$ (χ represents the passive scalar variance flux, Lilley et al., 2004).

A further source of complexity comes from the fact that the statistics of the conserved turbulent fluxes for atmospheric quantities are themselves scale dependent and exhibit multifractal behavior following the generic scaling relationship (Schertzer and Lovejoy, 1987):

$$\langle {\varphi_\lambda}^q \rangle = \lambda^{K(q)} \tag{4.2}$$

where the angle brackets represent the statistical average, q is the moment order generalized to any positive real number, $\lambda = L_0/l$ is the scale ratio, L_0 is the outer scale of the cascade and *l* the scale of the observation. φ_λ is the non-dimensional normalized turbulent flux measured at resolution λ, such that $\langle \varphi_\lambda \rangle = 1$. In multifractals, the scaling exponent function, K(q), is a nonlinear convex function of q, and thus an infinity of exponents are required to characterize the scaling behavior. This problem can be reduced to the determination of two parameters, α and C_1, by using the universal multifractal (UM) framework (Schertzer and Lovejoy, 1987) where K(q) given by:

$$K(q) = \begin{cases} \frac{C_1}{\alpha - 1}(q^\alpha - q), & a \neq 1 \\ C_1 \, \mathrm{qlog}(q), & a = 1 \end{cases} \tag{4.3}$$

The intermittency parameter, C_1, describes the sparseness or non-homogeneity of the mean of the process. The Levy index, α, defined in the interval [0, 2], indicates the degree of multifractality, with $\alpha = 0$ for monofractals. Both these parameters can be estimated using the Double Trace Moment technique (DTM) described by Lavallée et al. (1993).

The Fourier spectral analysis is an alternative way to investigate the presence of scale invariant behavior in atmospheric fields over a wide range of scales, manifested as log-log linearity of the power spectrum:

$$E(k_i) \sim {k_i}^{-\beta} \tag{4.4}$$

with k_i representing a 1-dimensional wavenumber. Eq. (4.4) has the advantage of representing a simple framework that is familiar to atmospheric scientists and is quite sensitive to presence of scaling behavior but also to scaling breaks and other types of deformations to the power law behavior. The spectral exponent, β, is related to UM parameters C_1, α and H (here it is assumed

that $H \equiv H_H$ since we are only interested in horizontal scaling behavior) by the following equation (e.g. Tessier et al., 1993):

$$\beta = 1 + 2H - K(2) \tag{4.5}$$

It can be seen from Eq. (4.5) that, neglecting the intermittency correction K(2), the Kolmogorov and Corrsin-Obukhov scaling with H=1/3 corresponds to $\beta = 5/3$, while the Bolgiano-Obukhov scaling with H=3/5 corresponds to $\beta = 11/5$.

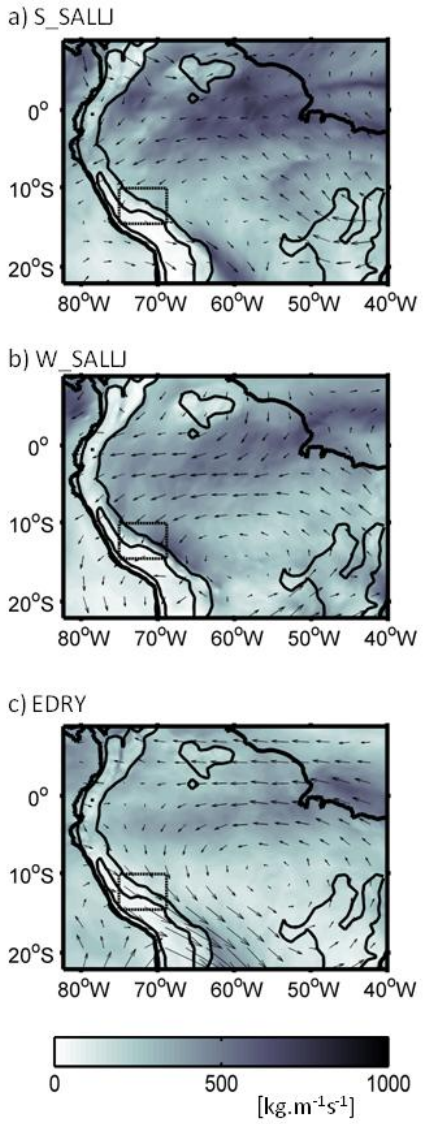

Fig. 2 *Vertically integrated moisture flux (shading) and low-level wind (arrows, computed in d01 over first 27 model layers) at 0100 LST for cases a) S_SALLJ, b) W_SALLJ and c) EDRY. Black lines represent topography at 0, 600 and 3500 m.*

Simulation	Daytime		Nighttime	
	P_{max} [mm/12hr]	$\sum P$ [mm/12hr]×10^5	P_{max} [mm/12hr]	$\sum P$ [mm/12hr]×10^5
EDRY	0.3	0.00	0.1	0.00
W_SALLJ	173.6	8.47	276.2	7.22
S_SALLJ	118.8	3.46	87.8	1.80

Table 4.1 *Local (pixel) maximum, P_{max}, and total domain surface rainfall accumulated over 12 hour period during daytime (7 to 19 LST) and nighttime (19 to 7 LST) over the HRDI for EDRY, W_SALLJ and S_SALLJ.*

4.3 Central Andes simulation results

The presence of the South-Atlantic subtropical high causes a large-scale counterclockwise low-level circulation transporting warm and moist unstable air from the tropical Atlantic Ocean and the Amazon basin towards the Andes, a large-scale north-south orographic barrier with elevations reaching 7 km. This westward moisture transport is verified in all three simulated cases (EDRY, W_SALLJ and S_SALLJ) as illustrated in Fig. 4.2 by the large-scale low-level flow (black arrows) together with the vertically integrated water vapor flux, $\Phi_v = -g^{-1}\int_{p_s}^{p_t} q_v V_H \, dp$ where g is the acceleration due to gravity, q_v is the water vapor mixing ratio, $V_H = \sqrt{u^2 + v^2}$ is the horizontal wind speed, and the pressure integral is taken between the surface and the top model grid level. However, there are important differences in the large-scale moisture flux patterns between the different cases with important consequences for orographic rainfall. Cases under SALLJ conditions during the rainy season (S_SALLJ in Fig. 4.2a and W_SALLJ in Fig. 4.2b) display much higher Φ_v values toward the central Andes compared to the dry season case EDRY (Fig. 4.2c). This pattern is maintained throughout the diurnal cycle as shown by the total amount of water vapor upstream of the mountains (Fig. 4.3a), resulting in very different total rainfall accumulations and local maximum rainfall over HRDI among the different case studies (Table 4.1). Case EDRY has low moisture availability (Fig. 4.3a), weaker upslope flows (Fig. 4.3b) and barely any CAPE (Fig. 4.3d) resulting in nearly zero atmospheric condensate production (Fig. 4.3c) and no surface rainfall accumulation throughout the diurnal

cycle (Table 4.1). In contrast, cases W_SALLJ and S_SALLJ produce complex surface rainfall accumulation patterns (Fig. 4.4) during day- (7 LST to 19 LST) and nighttime (19 LST to 7 LST). Several convective structures emerged along the eastern slopes and foothills of the Andes, where the orographic perturbations play a crucial role in triggering deep convective throughout the diurnal cycle together with the exponential decrease of saturation vapor pressure of the atmosphere which also contributes to the larger probability of finding greater precipitation values on the lower slopes of a high mountain (Houze, 2012). These results are in agreement with Romatschke and Houze (2010) previous observations of deep convective precipitation over the central Andes region under SALLJ conditions.

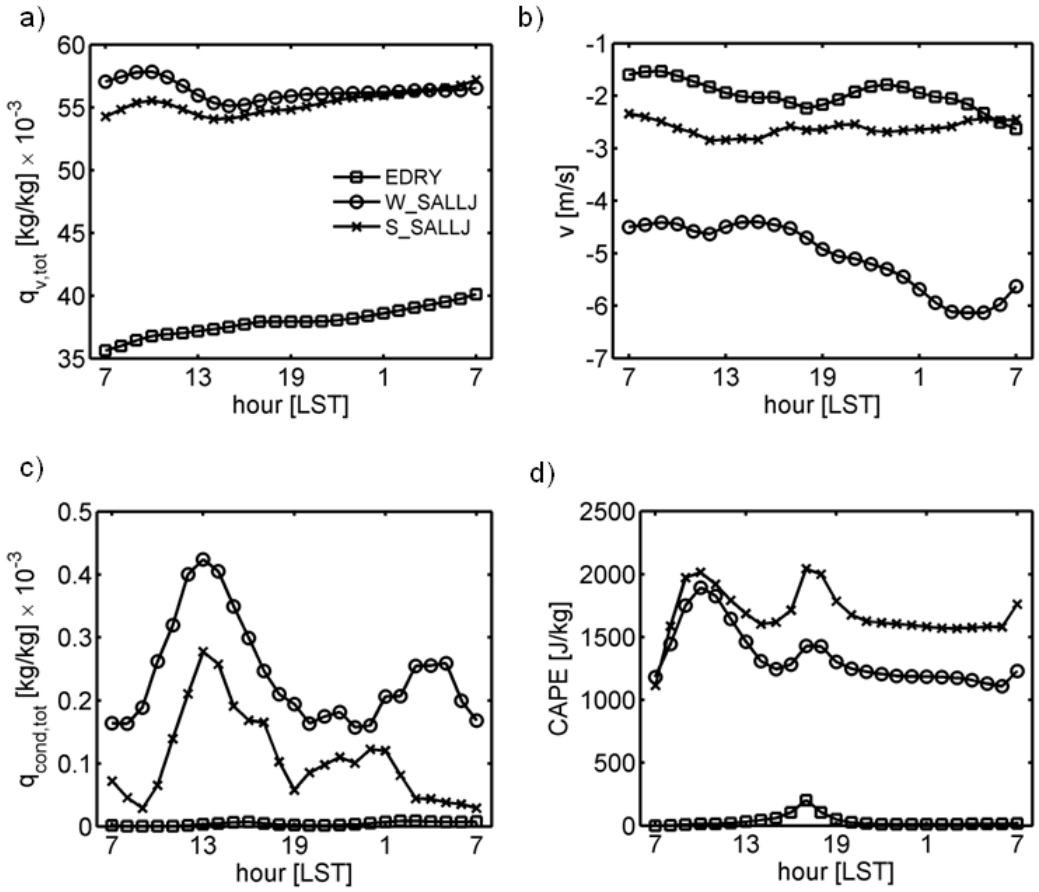

Figure 4.3 *Diurnal cycles for the three case studies (EDRY, W_SALLJ and S_SALLJ) of a) total water vapor mixing ratio available over HRDI upstream of the Andes eastern flanks (at topographic height below 600 m); b) mean y-direction wind component, v, at low-levels (first 27 model layers) upstream of the Andes eastern flanks; c) total condensate mixing rate over HRDI; d) mean CAPE over HRDI.*

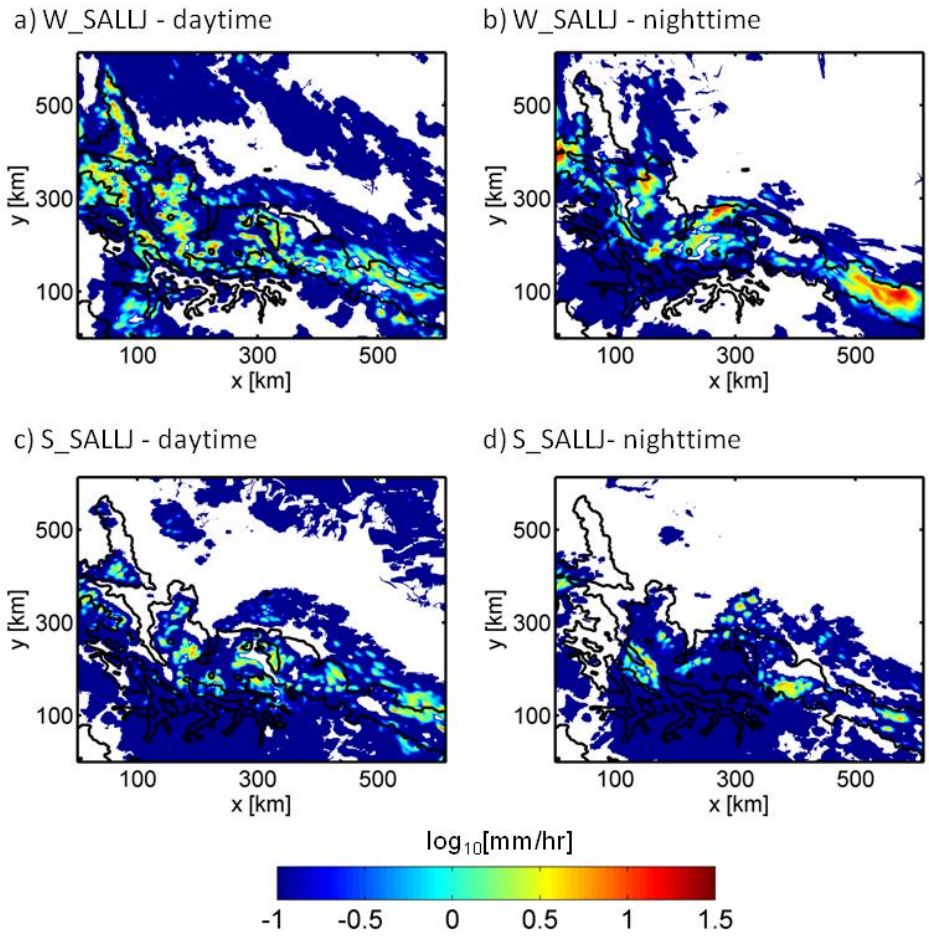

Figure 4.4 *Simulated mean hourly rainfall rate during daytime (7 to 19 LST) for case a) W_SALLJ and c) S_SALLJ; and during nighttime (19 to 7 LST) for case b) W_SALLJ and d) S_SALLJ. The black solid lines represent topographic elevation at 600 and 3500 m.*

The most intense rainfall patterns throughout the diurnal cycle were found under weak SALLJ conditions, when the low-level jet withdraws to the north (see Fig. 4.3 and Table 4.1), also in agreement with Romatschke and Houze (2010). This is explained by the more intense upslope moisture fluxes in the W_SALLJ case compared to S_SALLJ, with larger magnitude of the upslope flow (Fig. 4.3b) and larger moisture availability during the morning hours (Fig. 4.3a) resulting in stronger orographic triggering and enhancing of convection with associated larger and faster consumption of CAPE (Fig. 4.3d) causing proportionally large peaks in atmospheric condensation (Fig. 4.3c). The peak local rainfall accumulation occurs during the nighttime in case W_SALLJ with an increase of nearly 60% compared to the daytime peak (Table 4.), corresponding to the large intense structure over the south-east corner of Fig. 4.4b. This result contrasts with more modest daytime peaks of CAPE consumption (Fig. 4.3d) and atmospheric

condensate production (Fig. 4.3c). During daytime there is a layer of low-level strongly unstable moist flow impinging upon the Andes eastern flanks, with higher equivalent potential temperature, θ_e, than the above mid-altitude air (Fig. 4.5a). This strong instability tends to be released at first opportunity upon impinging on the foothills of the Andes (Houze, 2012), resulting in transient and intermittent condensation patterns. During the nighttime the upslope low-level flow is still strongly unstable with mean CAPE values over 1000 J/kg (Fig. 3d), despite the decreases in the strength of the vertical θ_e gradient (Fig. 5b). Additionally there is a nocturnal intensification of the upslope flow (Fig. 3c) which interacts with the local nighttime downslope mountain breeze to reinforce convection (as exemplified in Fig. 5b). The result is the nighttime generation of more organized and larger deep convective precipitation features with more persistent spatial distributions, responsible for the higher local rainfall accumulations.

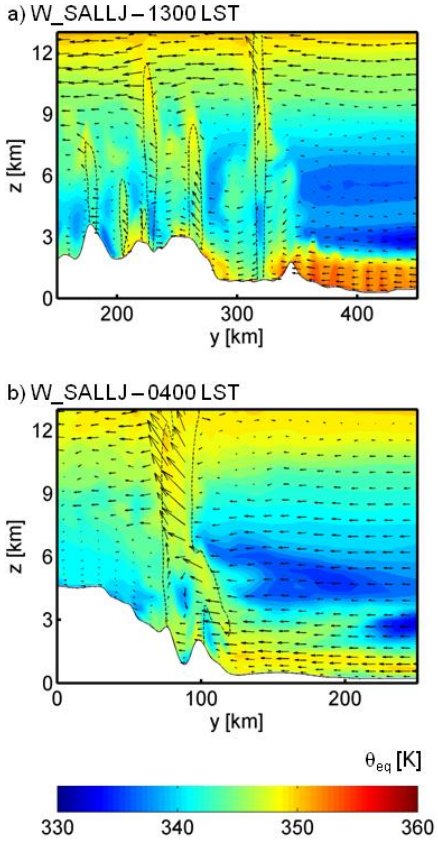

Figure 4.5 *Case W_SALLJ y-z cross sections of equivalent potential temperature (colorscale) and v-w flow (arrows) crossing the Andes at a) 1600 LST and b) 0400 LST. Dashed countour lines represent atmospheric condensate mixing ratio concentrations of 1 g/kg.*

4.4 Statistical scaling analysis

4.4.1 Ensemble scaling analysis

4.4.1.1 Kinetic energy spectral analysis

The horizontal scaling of atmospheric wind and water fields simulated by WRF was investigated separately in the x- and y-directions, accounting for possible horizontal anisotropy. The 1-dimensional power spectra and statistical moments were obtained by spatially averaging over all segments available inside a volume defined by seven constant height horizontal levels between 6000 and 9000 m over the HRDI, ensuring that all grid points are above the maximum topographic height of 5500m for this region. The 24-hour ensemble kinetic energy density per unit mass (KE) spectra for the three considered cases (EDRY, W_SALLJ and S_SALLJ) was computed using a one-dimensional spectral decomposition of velocities (u,v,w) following Skamarock (2004). The analysis was performed for the HRDI 1.2 km resolution fields, and also for a d02 sub-region co-centered with HRDI, with 128 × 128 pixels at 6 km resolution. Although this d02 sub-region occupies a slightly larger area than HRDI, it captures the same type of structure while the chosen power of two number of grid points keeps the Fourier analysis robust. Wavelengths below approximately $4\Delta s$ are considered unreliable due to the finite model grid resolution, Δs, and also due to well known problems associated with Fourier analysis over finite sized samples that also affect the analysis at the opposite edge of the scale range, for wavelengths close to the domain size, L_0.

For the non-convective case EDRY, the ensemble KE spectra displayed remarkable $\beta = 2$ behavior over nearly the entire considered range of scales from domain length, L_0~750 km, down to a few kilometers (Fig. 4.6a), with close agreement between the x- and y-direction and also between HRDI and d02 spectral scaling. For case W_SALLJ the 24h-hour ensemble KE spectra over HRDI showed nearly x-y direction isotropy but with two distinct scaling regimes separated by a break around the 12-13 km wavelength (Fig. 4.6b): a large-scale regime characterized by $\beta \approx 1.7$, and a small-scale regime with much steeper slopes in the 3.3-3.6 range. An algorithm based on a variable break point and minimization of the least-square error was used to fit two linear segments to the power spectrum and find the spectral location of the scaling break. For case S_SALLJ, the ensemble KE spectral analysis showed clear horizontally anisotropic scaling with distinct behavior in the x- and y-directions (Fig. 4.6c): unbroken scaling

behavior with $\beta = 2.0$ in the y-direction contrasting with a scaling break in the x-direction occurring around 13 km separating the large-scale $\beta = 1.6$ regime from a steeper $\beta = 3.4$ slope at the small-scales. The power spectra computed from d02 for W_SALLJ and S_SALLJ cases displays very close agreement with those of HRDI at least down to about 24 km, corresponding to 4 times the 6 km resolution of d02 as expected.

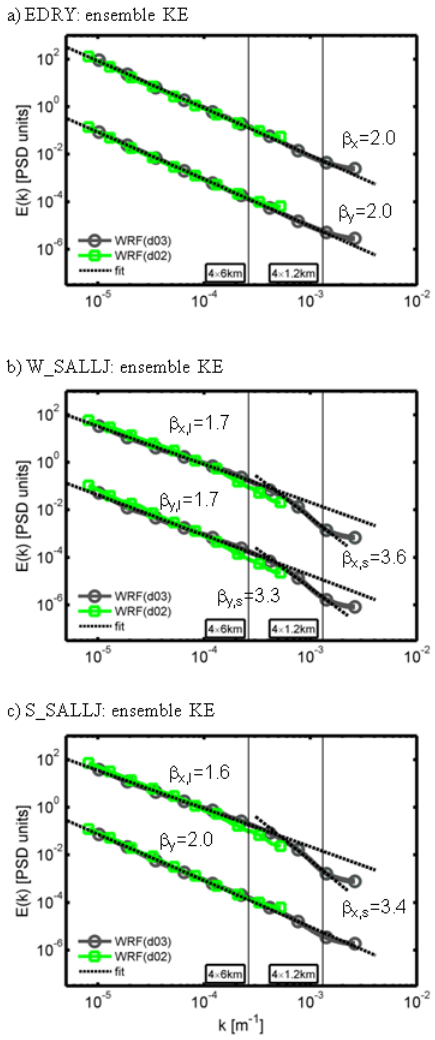

Figure 4.6 Log-log plots of 24-hour ensemble 1-dimensional Fourier kinetic energy spectra for HRDI (from 512×512 pixels 1.2 km resolution, in gray) and d02 (from 128×128 pixels 6 km resolution, in green) for simulations a) EDRY, b)W_SALLJ and c) S_SALLJ. Top lines represent x-direction and bottom y-direction spectra. Lines have been vertically displaced for better visualization. Dashed black lines represent least-square fits to d03 spectra.

4.4.1.2 Atmospheric water spectral analysis

The spectra for atmospheric total water mixing ratio fields (vapor+clouds+rain+ice), q_t, was also analyzed since the q_t statistics are of primary importance for sub-grid scale parameterization of clouds (e.g. Bony and Emanuel, 2001). The choice of total water has the further advantage of avoiding the complex problem of handling the large portions of zero values in the heavily thresholded water fields such as clouds or precipitation, which can deform the spatial scaling behavior significantly unless the analysis is performed only in non-zero pixels posing a considerable limitation for high-resolution large domains (see e.g. Nogueira et al., 2014 and references therein). In fact, here the fraction of nonzero condensate mixing ratio values was around 10% for both cases W_SALLJ and S_SALLJ, and nearly zero for EDRY, hence preventing the desired robust statistical analysis. However the fraction of nonzero q_t values in the considered volume is only ~1% for all cases.

Field	**Simulation**	$\beta_{x,l}$	$\beta_{x,s}$	$l_{b,x}$ **[km]**	$\beta_{y,l}$	$\beta_{y,s}$	$l_{b,y}$ **[km]**
KE	EDRY	2.0	2.0	-	2.0	2.0	-
	W_SALLJ	1.7	3.6	12	1.7	3.3	13
	S_SALLJ	1.6	3.4	13	2.0	2.0	-
q_t	EDRY	2.1	2.1	-	2.1	2.1	-
	W_SALLJ	1.7	4.0	15	1.6	4.4	15
	S_SALLJ	1.7	4.3	15	1.6	4.3	15

Table 4.2 *Estimated spectral exponents from 24-hour ensemble analysis for kinetic energy (KE), and total water mixing ratio (q_t). Subscripts l and s correspond to large- and small-scales spectra slopes, with $l_{b,x}$ and $l_{b,y}$ representing the respective length where break of the scaling occurs.*

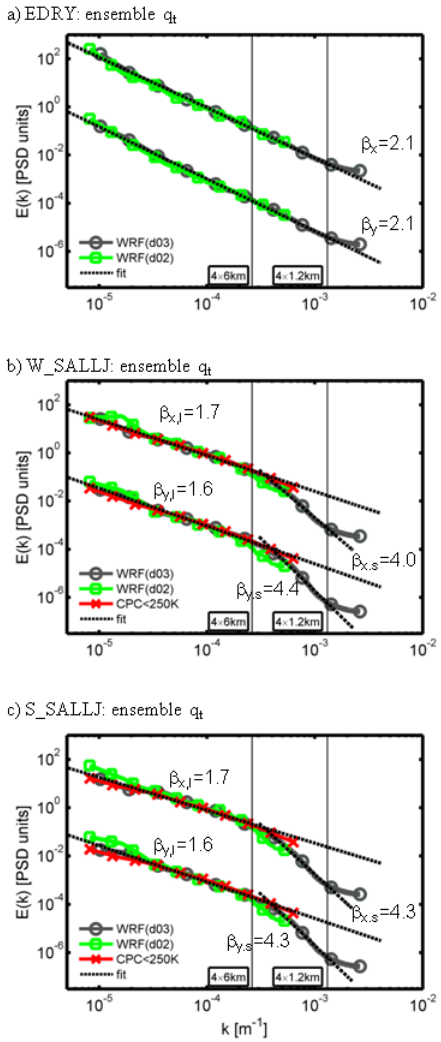

Figure 4.7 *Log-log plot of 24-hour ensemble 1-dimensional q_t Fourier spectra for HRDI (from 512×512 pixels 1.2 km resolution, in gray) and d02 (from 128×128 pixels 6 km resolution, in green) for simulations a) EDRY, b)W_SALLJ and c) S_SALLJ. Red line represents power spectra from NCEP CPC brightness temperatures <250 K fields. Top lines represent x-direction and bottom y-direction spectra. Lines have been vertically displaced for better visualization. Dashed black lines represent least-square fits to d03spectra.*

The 24-hour ensemble power spectra of q_t are tightly connected to the results obtained for KE: case EDRY shows unbroken scaling behavior with $\beta = 2.1$ (Fig. 4.7a), while a scaling break around 15 km was found in both W_SALLJ (Fig. 4.7b) and S_SALLJ cases (Fig. 4.7c) separating the large-scale regime with $\beta = 1.6 - 1.7$ slopes from a much steeper small-scale slopes with values >4. Total water fields also display very good agreement in the spectra

obtained from d02 and HRDI with nearly horizontally isotropic behavior for EDRY and W_SALLJ cases. The main difference between KE and q_t occurs for case S_SALLJ where nearly horizontally isotropic scaling was obtained in contrast to the anisotropic behavior in the former (see Table 4.2).

The scaling derived from NCEP Climate Prediction Center (NCEP/CPC) globally merged infrared product at 4 km is used to inform on the scale-invariant behavior of the real atmosphere under convective conditions. Following Nesbitt et al., (2000), satellite measured brightness temperatures below 250K are used to identify convective structures. The scaling behavior of such convective structures (red lines in Fig. 4.7a and Fig. 4.7b) matches the simulated spectra of both W_SALLJ and S_SALLJ. Under dry conditions, when atmospheric condensate is nearly absent such analysis from brightness temperatures is not possible. The robustness of the simulated large-scale scaling behavior is further supported by the simulations ability to reproduce the main features observed over the central Andes under respective synoptic conditions as discussed in Section 3, and also in Sun and Barros (2014).

Similar scaling breaks separating a shallower large-scale linear behavior from an abrupt steepening at small-scales were previously observed in high-resolution NWP simulations of convective storms for ensemble KE spectra (Skamarock, 2004) and hourly rainfall spectra (Harris et al., 2001), who also found similarity between the large-scale simulated and observed spectra down to the model effective resolution. The model effective resolution was defined by Skamarock (2004) as the wavelength separating the large-scale scaling behavior in good agreement with observations of the atmosphere from a spurious spectral steepening at smaller wavelengths, reaching unphysical values of $\beta > 3$. Also, Skamarock (2004) showed that the steepening is caused by the underrepresentation of small-scale variability associated with the numerical integration over a finite grid with finite resolution, and the smoothing artifacts of the subgrid-turbulence mixing parameterization and (unphysical) numerical diffusion schemes introduced to maintain the numerical simulations stable. Hence the effective resolution was shown to depend on the particular physical options of the NWP model. In the present work, the effective resolution is shown to also be dependent on the particular flow regime. Under convective conditions, the effective resolution estimated here at 1.2 km resolution is between $10\Delta s$ and $14\Delta s$, much larger than the typically 4-5Δs values typically considered for numerical

simulations. An important implication of these results is that the effective improvement in resolution associated with the nested dynamical downscaling between 6- and 1.2-km resolutions is on the order of 2 or lower (between the effective resolutions of 25-30km in d02 and 10-16 km in d03), hence much smaller than the 5 ratio between the respective grid resolutions.

4.4.1.3 Moment scaling analysis

Ensemble horizontal 1-directional moment scaling analysis of HRDI KE (Fig. 4.8a) and q_t (Fig. 4.9a) fields under dry conditions (EDRY) showed remarkable unbroken multifractal behavior up to moment orders of 3 over the scale range of interest, from scales near L_0 down to approximately $4\Delta s$. For convective cases, under SALLJ synoptic conditions the multifractal scaling behavior was found at large-scales above to the scaling break length estimated in the spectral analysis, and non-scaling behavior was obtained at smaller-scales below the break length scale (Fig. 4.8b and Fig 4.8c for KE fields, and Fig. 4.9b and Fig. 4.9c for q_t). Table 4.3 presents the UM parameters C_1 and α estimated for the large-scales (using the break length scales obtained in the spectral analysis) using the DTM technique. For both KE and q_t, the estimated intermittency parameters C_1 in the x- and y-directions were lower (0.07-0.10) in the non-convective dry scenario (EDRY) as compared to (0.13-0.20) for deep convective cases (W_SALLJ and S_SALLJ). This increased intermittency in convective cases is intuitive given the presence of strong localized convective updrafts and associated increased atmospheric condensation. The multifractal parameter α varies in the range 1.5-2.0, with slightly lower values in EDRY case for KE and q_t but without any clear tendency between the distinct simulations.

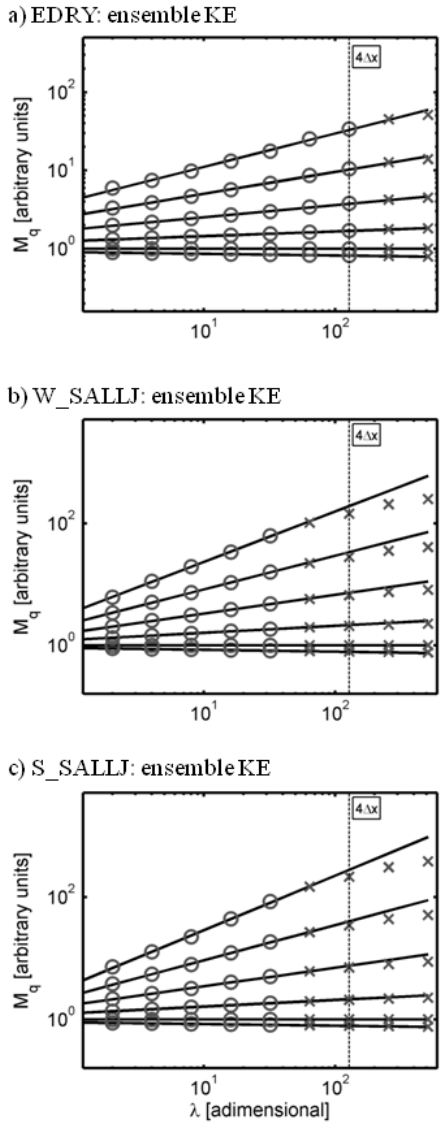

Figure 4.8 *Log-log plot of 24-hour ensemble x-directional kinetic energy statistical moments against scale ratio, computed over the HRDI for simulations a) EDRY, b) W_SALLJ and c) S_SALLJ. The 'o' markers represent estimated values included in the fits (black lines) while 'x' markers represent scales below the scaling break length scale estimated from spectral analysis (Table 4.1). From bottom to top, the different lines represent moment orders q=0.5, 1, 1.5, 2, 2.5and 3.*

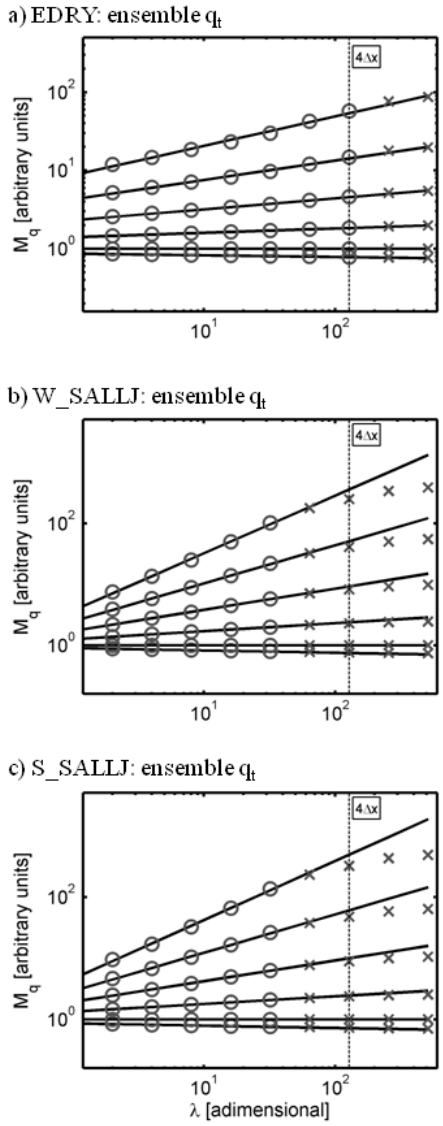

Figure 4.9 *Same as Fig. 4.8 but computed from q_t fields.*

In summary the ensemble scaling analysis reveals that WRF simulated fields are able to reproduce the scaling behavior in atmospheric observations down to the model effective resolution, below which the statistical structure is misrepresented by the model due to finite grid spacing, deficiencies in the used sub-grid scale parameterizations and the (unphysical) numerical diffusion introduced to keep the simulations stable. A fundamental transition was found in the scaling behavior of atmospheric wind and water fields between non-convective and convective regimes. Additionally, in the convective regime the HRDI effective resolution shifts to length scales well above 4-5Δs, causing a significant decrease in the resolution gain when the grid-

length spacing is reduced from 6- to 1.2km, i.e. from a resolution where convective parameterizations are required to convection allowing resolution.

Field	Simulation	$C_{1,x}$	$\alpha_{x,}$	$C_{1,y}$	α_y
KE	EDRY	0.08	1.8	0.10	2.0
	W_SALLJ	0.15	2.0	0.17	2.0
	S_SALLJ	0.15	2.0	0.16	2.0
q_t	EDRY	0.08	1.6	0.09	1.8
	W_SALLJ	0.17	2.0	0.19	2.0
	S_SALLJ	0.17	2.0	0.20	2.0

Table 4.3 *Estimated UM parameters from 24-hour ensemble moment scaling analysis for kinetic energy (KE) and total water mixing ratio (q_t).*

4.4.2 Transient scaling analysis

4.4.2.1 Transient spectral analysis

The ability of NWP models to reproduce the scale-invariant behavior of observations to a good approximation over wide ranges of scales provides a path to investigate the dynamical variability of the scaling behavior under different conditions. In this context, the dynamical transient character of horizontal scaling behavior was investigated by 1-dimensional spectral analysis of instantaneous velocity and water HRDI fields, averaged over the considered 6 to 9 km constant height levels.

The diurnal cycle of estimated spectral slopes is presented in Fig. 4.10 for simulated KE and q_t fields. The non-convective dry season case (EDRY, in blue) exhibits unbroken horizontal scaling behavior with nearly isotropic behavior and small variability of the scaling exponent in the [2, 2.3] range for both fields, similar to the ensemble scaling behavior presented in the previous section. The KE scaling behavior for convective cases (W_SALLJ and S_SALLJ) also showed single spectral exponents nearly horizontally isotropic during the first morning hours (7 to 9 LST) with β~2-2.3. After these initial hours, there is an abrupt change in scaling behavior with spectral slopes fluctuating around 5/3, mostly below this value due to the K(2) intermittency

correction (see Eq. 4.5). Horizontal isotropy holds to a good approximation throughout most of the day for case W_SALLJ, with similar β trends in the x- and y-direction conserving the differences below 0.25 which cannot be distinguished from the typical uncertainty in the estimation of β for single instantaneous fields (e.g. Barros et al., 2004). The only exceptions occurring in the early morning (6 to 7 LST in the next morning) larger x-y anisotropy is found in the KE spectra, with x-direction statistics displaying broken 5/3 behavior while unbroken behavior with steeper slopes around 2 is found in the y-direction. In contrast, KE spectra for case S_SALLJ display horizontally anisotropic behavior throughout most of the day, with unbroken $\beta \sim 2$ scaling in the y-direction and broken $\beta \sim 5/3$ in the x-direction in agreement with the result obtained from ensemble scaling analysis in Section 4.4.1.

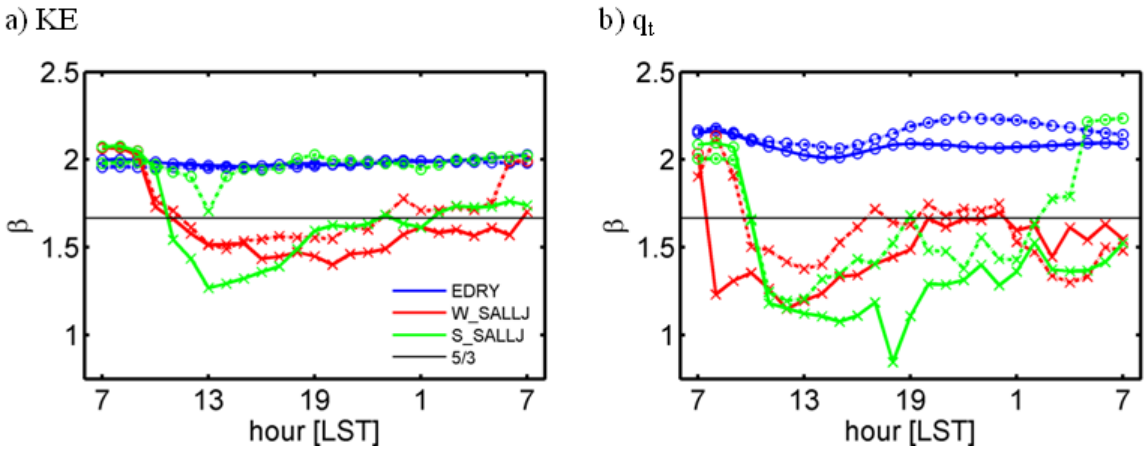

Figure 4.10 *Diurnal cycle of transient spectral exponent computed from instantaneous fields in the x- (solid line) and y-direction (dashed line) for cases EDRY (blue), W_SALLJ (red) and S_SALLJ (green) for a) KE and b) q_t. Unbroken scaling behavior over scale range between L_0 and $4\Delta x$ is signaled by 'o' markers while broken scaling behavior is signaled by 'x' markers, with the value represented in the latter case corresponding to the large-scale scaling behavior.*

Total water mixing ratio fields (Fig. 4.10b) from case W_SALLJ display a generally similar diurnal cycle to KE, including a similar transition between unbroken β~2-2.2 spectra in the non-convective regime to a broken scaling with decreased slopes around 5/3 at the large-scales when convection sets in. This transition was also present in S_SALLJ q_t fields, but in contrast to KE transient scaling for total water case S_SALLJ remains mostly horizontally isotropic except in the early morning at the end of the study time-period, where significant anisotropy emerges.

Also, for both SALLJ simulated cases the results associated with q_t show larger amplitudes of the β fluctuations below the 5/3 values under convective regime, with amplitudes as high as 0.5 in agreement with the intermittency corrections for the UM parameters found in the present investigation. This significant variability of the scaling exponent under convective regime highlights the variability of the multifractal parameters under different stages of dynamical convective organization, as previously found in Nogueira et al. (2013) who reported significant differences in the scaling behavior of organized banded and cellular convection.

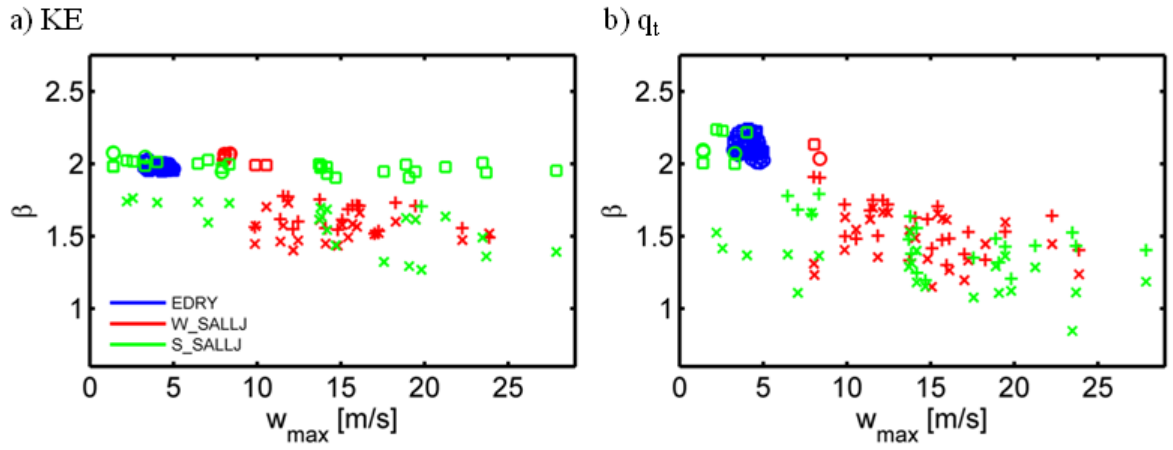

Figure 4.11 *Transient spectral exponents against peak ascending vertical velocity (w_{max}) in HRDI for a) KE and b) q_t. EDRY is represented in blue, W_SALLJ in red and S_SALLJ in blue. Unbroken scaling behavior over scale range between L_0 and $4\Delta x$ is signaled by 'o' markers in the x-direction and '□' markers in the y-direction, while broken scaling behavior is signaled by 'x' markers in the x-direction and '+' markers in the y-direction, with the value represented in the broken case corresponding to the large-scale scaling behavior.*

The observed transition in the scaling behavior under SALLJ conditions between unbroken $\beta \approx 2 - 2.3$ and broken spectra with shallower slopes is tightly coupled to the presence of strong deep convective structures, occurring around the same time of abrupt CAPE release (Fig. 4.4d) and the associated rapid increase of atmospheric condensate concentration (Fig. 4.4c). This concurrence between the transition in the scaling regime of total water fields and the strength of convection is clearly illustrated in Fig. 4.11b, where β is plotted against the maximum updraft intensity within HRDI, w_{max}. When w_{max} is below 5 m/s, in the absence of strong updrafts, single scaling behavior with spectral slopes ~2-2.3 is obtained, except for 3 outliers in the more

variable S_SALLJ case. Broken scaling behavior with spectral slopes fluctuating below 5/3 was found for much stronger updrafts, with updraft peak intensities above ~12-13 m/s. For w_{max} values in between, the results show a transition zone where β takes values over the entire 1-2.2 range. Similar dependence on w_{max} was found for KE (Fig. 4.11a) in both EDRY (blue) and W_SALLJ (red) cases. Case S_SALLJ displays a more complex structure, associated with strong horizontal anisotropy, with unbroken ~2-2.3 values for strong updrafts in the y-direction and broken ~5/3 behavior occurs in the x-direction.

Examples of instantaneous q_t spectra at 7 and 19 LST (Fig. 4.12a and Fig. 4.12b) illustrate the nearly linear log-log behavior under the two distinct regimes - unbroken scaling with $\beta \approx$2-2.3 and broken spectra with lower β values around 5/3. The linear fits to instantaneous fields hold to a remarkable approximation, with linear regression coefficients r^2>0.99 for KE and >0.93 for water mixing ratio, in the latter case with values >0.99 at all times for cases EDRY and W_SALLJ, and slightly less consistent values for case S_SALLJ. The spatial patterns corresponding to these spectra are depicted in Fig. 4.12c to Fig. 12f. The single scaling behavior corresponds to situations where large-scale gradients dominate, with a strong orographic component. In fact, the topography in HRDI displays single spectral scaling itself, with β values near 2.1 in the x-direction and 2.3 in y-direction (Fig. 4.13), very similar to the scaling regime found for kinetic energy and water fields, thus suggesting that orography plays a major role in their variance distribution, as previously pointed out by Bindlish and Barros (2000). Additionally, spectral exponents with values around 2 are typically found for the Earth topography (see e.g. Gagnon et al., 2006), which could explain the spectral exponents reported in the literature for humidity fields. Under stratiform or weak convective conditions the presence of a few local cells is possible with minor impact on the scaling behavior, as exemplified by the top spectra in Fig. 4.12a corresponding to pattern in Fig. 4.12d. In contrast, the 5/3 regime arises when intense local gradients develop associated with the emergence of deep convective cells extending well inside the considered z=6-9 km layer (see Fig. 12f and also Fig. 4.5). Notice that in the so-called convective regime, differences in the spectral slopes of 0.5 or larger can be found between different times and/or simulations, suggesting that this convective range does not correspond to a unique scaling regime. In other words different types of convective organization can display different scaling exponents.

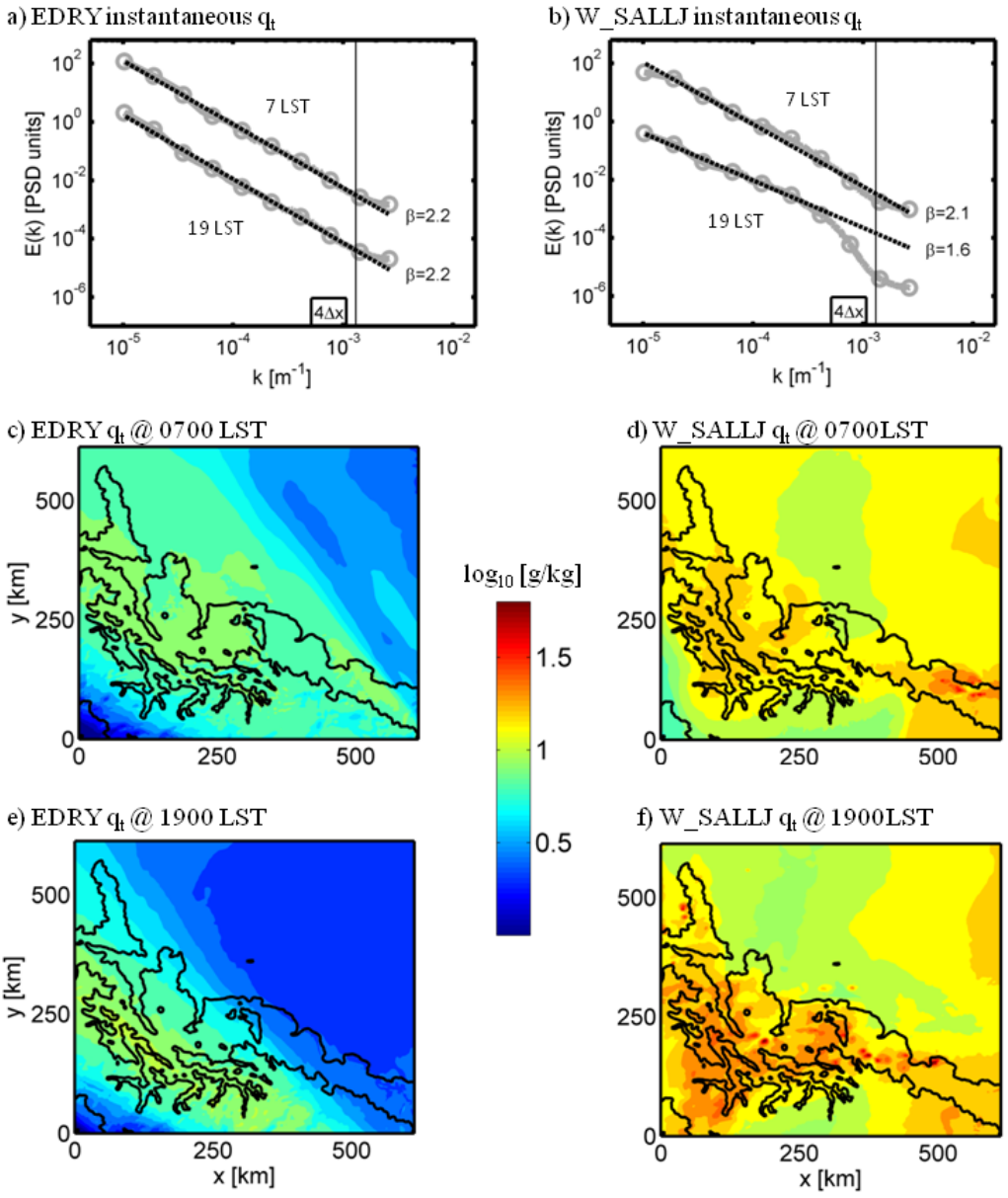

Figure 4.12 *Log-log plots of vertically averaged instantaneous q_t horizontal spectra (gray) for simulation a) EDRY, b) W_SALLJ, with top line at 07LST and bottom at 19LST. Black dashed line is least square fit. Horizontal maps of qt vertically integrated q_t over z=6-9km at 07LST and 19LST respectively for c) and e) EDRY and d) and f) W_SALLJ.*

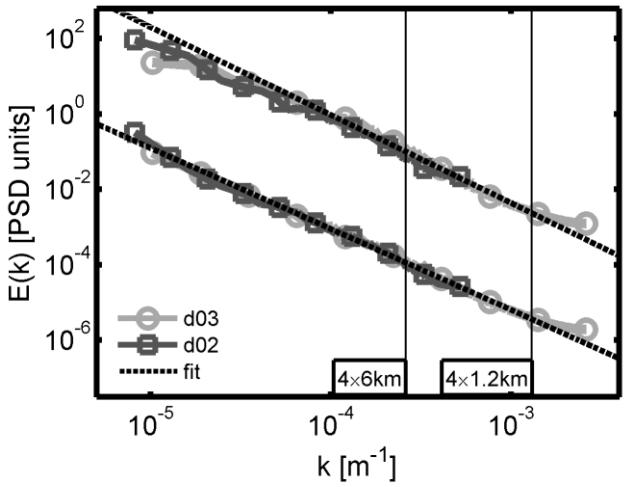

Figure 4.13 *Log-log power spectra computed from topographic elevation over HRDI (light grey) and d02 (dark grey) and the respective least square fit (black dashed line). Vertical black thin lines represent the 4 times grid resolution scales for d02 and HRDI.*

4.4.2.2 Transient moment scaling analysis

Scaling also holds to a very good approximation for the statistical moments of instantaneous water and kinetic energy fields, with small variations about the log-log linear (power law) relationships with scale. The transition between weak and strong updrafts is also present when the statistical moments are analyzed (Fig. 4.14), with single scaling behavior and lower intermittency ($C_1 \approx 0.05 - 0.1$) for w_{max}<5-7 m/s and broken scaling with higher intermittency for strong updrafts, w_{max}>10-15 m/s. As pointed out for the ensemble moment scaling analysis, the increased intermittency in convective regimes is expected due to emergence of localized intense cellular features compared to the smoother stratiform patterns. Between these two ranges there is a transition zone where C_1 increases approximately linearly. Similar to the results obtained for the ensemble analysis in Section 4.4.1, UM parameter α does not show any clear tendencies for the transition between non-convective and convective regimes (Fig. 4.15) statistics.

In summary, scaling behavior holds to a remarkable approximation in numerically simulated instantaneous atmospheric wind and water fields. This scale-invariant behavior is intrinsically transient, characterized by scaling parameters that dynamically depend on the atmospheric state. In particular, a robust transition was found in parameters β and C_1 between non-convective and

convective regimes. Because the high-resolution NWP simulations are obtained under fully realistic configurations, capable of representing the observed atmospheric behavior down to the model effective resolution, the present results extend the previous results of Nogueira et al. (2013) that found similar non-convective/convective transitions for rainfall and cloud fields obtained from highly idealized simulations of orographic convection at 250m resolution.

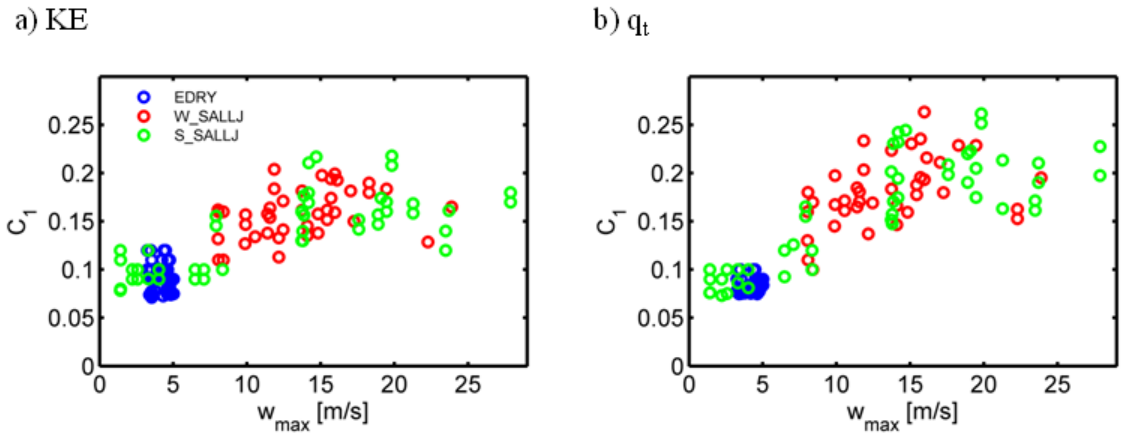

Figure 4.14 *Transient intermittency parameter, C_1, against maximum ascending vertical velocity (w_{max}) in HRDI for a) KE and b) q_t. EDRY is represented in blue, W_SALLJ in red and S_SALLJ in blue.*

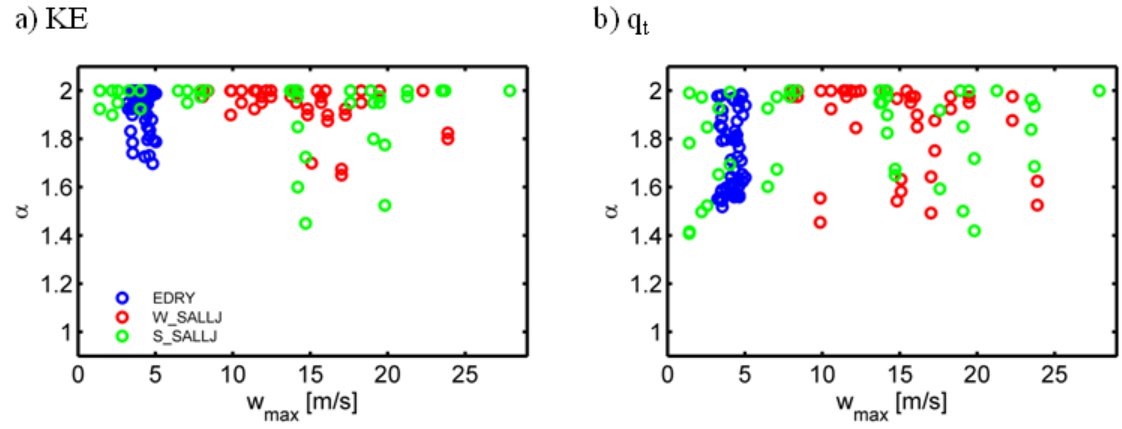

Figure 4.15 *Transient multifractal parameter, α, against maximum ascending vertical velocity (w_{max}) in HRDI for a) KE and b) q_t. EDRY is represented in blue, W_SALLJ in red and S_SALLJ in blue.*

4.5 Sub-grid scale statistics of atmospheric moisture

Cloud fraction, cf, is a key variable in the sub-grid parameterization of clouds in NWP, representing the relative volumes of clear-sky and clouds inside a certain large-scale domain, which can be a coarse resolution grid volume or any other convenient domain of choice. In other words, the cloud fraction parameter describes the spatial distribution of condensed water within this domain. Cloud fraction can be equivalently defined as the fraction of horizontal area under the simplifying assumption that water fields are homogeneous along the vertical direction inside a grid-box, based on a smaller vertical grid spacing of the numerical simulations (in the order of 100 m) compared to the horizontal grid spacing (1.2 km in the highest resolution domain). Following Bony and Emanuel (2001) the probability distribution function (PDF) of total water mixing ratio (q_t), $\int_0^\infty P(q_t)dq_t = 1$, can be used to represent stochastically the cloud fraction within a model grid-box as $cf = \int_{q_s}^\infty P(q_t)dq_t$, where q_s is the saturation mixing rate, that can be diagnosed from the coarse resolution temperature and pressure fields. Consequently, the determination of the sub-grid probability distribution of total water mixing ratio is a question of primary importance for the stochastic parameterization of clouds.

Bony and Emanuel (2001) assumed a generalized log-normal form to model $P(q_t)$ which might not be ideal for multifractal fields as argued in Section 4.1. Here the ability of statistical scale-invariant behavior to represent the sub-grid scale q_t PDF was investigated by using a stochastic modified fractal interpolation algorithm to generate an ensemble of plausible q_t fields at the desired resolution based on the known coarse resolution information alone. These fractal downscaling methods work in the Fourier spectral framework, assuming horizontal isotropy for simplicity to generate 2-dimensional fractional Brownian surfaces with the desired spectral slope, which are then used as spatial interpolating surfaces. Detailed descriptions of the algorithm and performance evaluations can be found in Bindlish and Barros (1996, 2000), Rebora et al. (2006), Tao and Barros (2010) and Nogueira and Barros (2014). In analogy with the dynamical downscaling undertaken with nested domains in WRF, the resolution increase occurs only in the horizontal directions, while in the vertical the much higher resolution of the numerical grid is kept unchanged. Notice that to extend the downscaling to the vertical direction the horizontal-vertical anisotropy must be taken into consideration as discussed in Section 4.1 and Section 4.2.

Previous research demonstrated that the fractal methods used here are able to accurately preserve the coarse resolution structure while enhancing the variability at the sub-grid scales, and can rapidly produce a large number of statistically coherent high-resolution realizations of the field. In particular Nogueira and Barros (2014) showed that downscaled realizations of observed precipitation fields generated by fractal methods can be used to produce accurate stochastic predictions of streamflow in hydrological simulations representing a considerable improvement in prediction accuracy compared to other interpolation methods. It is important to stress that such fractal downscaling methods require the *a priori* knowledge of the spectral exponent, which is far from being a trivial problem when the transient scaling behavior is taken into account, as pointed out in Nogueira et al. (2013) who found complex non-linear transitions in the scaling behavior between different flow regimes, with dynamical dependencies on several large-scale properties including atmospheric stability, mean wind speed and orographic forcing. The transient scaling parameters can potentially be estimated directly from the instantaneous coarse resolution field, as done in Nogueira et al. (2014). However, for limited-area domains the information in instantaneous coarse resolution fields is generally not sufficient to obtain direct robust estimates of the scaling parameters.

Fractal downscaling methods combining coarse resolution observations and high-resolution ancillary data have been proposed for remote sensing applications (Kim and Barros, 2002; Barros and Tao, 2008). In the general case, such ancillary fields will not be available at the resolutions required for cloud parameterization and for prognostic applications, and hence a strategy based on coarse resolution information alone is preferred. An alternative method is presented here based on the non-convective/convective scaling transition. Whereas a nonlinear fit to the spectral slope dependencies in Figs. 4.10 and 4.11 is possible, the limited number of cases studied in this manuscript prevents the estimation of general relationships. Thus, a first-order assumption is made by taking $\beta = 2.1$ for non-convective cases and $\beta = 1.5$ for convective cases (representing the 5/3 regime with intermittency correction), corresponding to the respective mean spectral slopes estimated from instantaneous q_t statistics for the three considered simulated cases in Section 4.4.2.

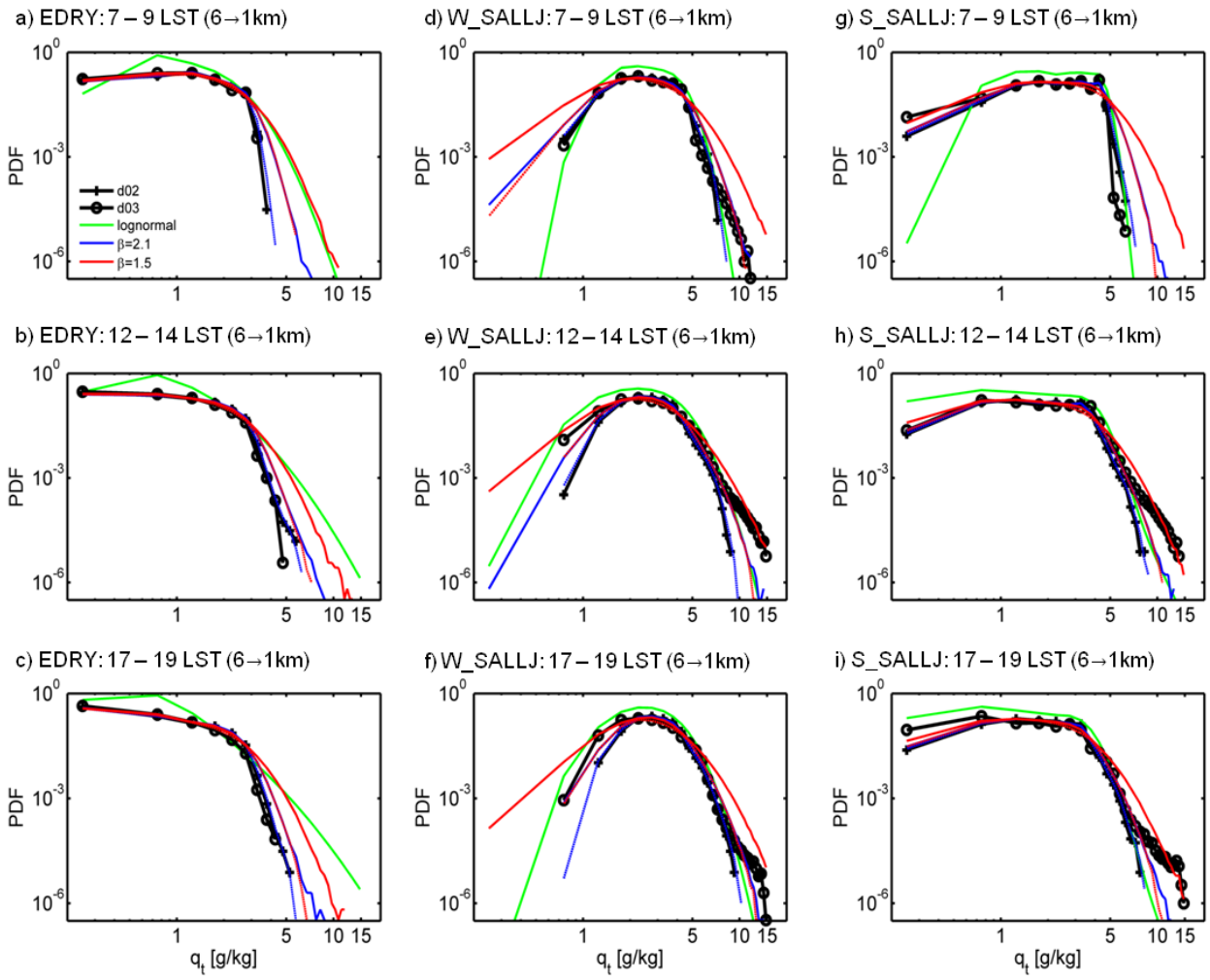

Figure 4.16 *Probability distribution function computed from HRDI (black circle markers) and d02 (black 'x' markers) for simulation EDRY (left column), W_SALLJ (middle column) and S_SALLJ (right column) in the period 7-9 LST (top row), 12-14 LST (middle row) and 17-19 (bottom row). Green line represents the lognormal distribution estimated from d02 fields over the same period and simulation. Red (blue) lines represent lower and higher PDF limits estimated using an ensemble of 50 fractal downscaled realizations from d02 fields at 6km resolution to 1.2km resolution considering a spectral slope β=1.5 (β=2.1).*

The PDFs obtained directly from the WRF simulated q_t fields over the HRDI region at 6- and at 1.2 km resolution are shown by black lines in Fig. 4.16 for the 3 simulations. The results display clearly distinct shapes of the PDF between the different simulated cases. Case EDRY displays higher probabilities associated with q_t values $\leq$ 1 g/kg and maximum intensities below 5 g/kg (Fig. 4.16a to Fig. 4.16c). In the most intense convective case W_SALLJ the higher probabilities

are associated with q_t values in the [1,5] g/kg range and maximum intensities can reach values around 15 g/kg when deep convective structures form during the afternoon (Fig. 4.16e and Fig. 4.16f). Finally, case S_SALLJ displays high probabilities associated with low q_t (≤ 1 g/kg), but also reaching high intensities around 15 g/kg. The respective PDFs estimated for each case using log-normal statistics are represented by green lines in Fig. 4.16, with the statistical moments estimated directly from the 1.2 km HRDI domain, hence representing a best case scenario where the high-resolution statistics are known exactly. Note that, in the general case, the high-resolution must be estimated from the coarse resolution information alone introducing further uncertainties to the log-normal PDFs. The blue (red) lines in Fig. 4.16 represent the PDFs estimated from the fractal downscaling from 6- to 1.2-km resolution considering $\beta = 2.1$ ($\beta = 1.5$). The two lines for each case mark the limits of the ensemble spread of PDF resulting from 50 realizations, hence representing the range of possible solutions given by the fractal downscaling algorithm including the associated uncertainty. While the log-normal statistics can capture the essential shape of the PDF, they overestimate the probabilities over the dominant ranges (most probable intensities) in all cases, and largely overestimate the probabilities associated with higher intensities in the EDRY (Fig. 4.16a-c) and underestimate the high intensity tails in the convective cases (Fig. 4.16e,f,h,i). The fractal downscaling solutions capture the most probable range of values in all cases independently of the chosen scaling exponent. The ability of the fractal scheme to conserve the coarse resolution structure has a large contribution to this very good fit, since the differences between 6- and 1.2-km PDFs in this interval of values are small.

The present analysis is limited by the errors associated with the misrepresentation of the statistical structure in the high-resolution simulated fields, as discussed in Section 4. Nonetheless, the fractal downscaling scheme is capable of capturing important properties of the expected PDF behavior when increasing resolution: on the one hand by taking $\beta = 2.1$ the results capture the PDFs for cases where the distribution changes slowly with increasing resolution, typical in the less intermittent non-convective cases; on the other hand the 1.5 spectral slopes represent convective situations where there is a sharp increase in the high-values tail and a corresponding increase in the low-value end, caused by mass conservation. Overall, the high-resolution PDF can be found within the ensemble spread of fractal solutions. Consequently these results provide a basis for stochastic sub-grid parameterization of cloud fraction in prognostic

applications relying on simulated fields only, and it that can easily be generalized for any scaling geophysical fields given that the respective spectral exponents can be estimated. The fractal downscaling solutions with the regime-based spectral slope approximations provide computationally affordable alternatives for real-time applications, and can be also useful when coarse resolution fields do not have enough information to characterize their scaling behavior (i.e. limited area domains, very large scale ratios).

4.6 Conclusions

High-resolution one-way nested simulations performed with WRF model over the central Andes region were able to accurately reproduce the main features of observed rainy season orographic deep convective events and dry season conditions (Sun and Barros, 2014). The typically observed horizontal scaling behavior of atmospheric fields over wide ranges of scales was also captured by the numerical simulated wind and atmospheric water content fields down to the model effective resolution, which is a transient length-scale dependent on the particular simulated conditions and model physics, that is the chosen NWP physical options.

Under non-convective conditions the effective resolution is around 4-5Δs associated with the finite grid spacing. However, when convection sets in, a spurious scaling break emerged around 10-15Δs with an abrupt steepening of the spectral slope at the small-scales reaching unphysical $\beta > 3$ values, associated with excessive smoothing introduced by turbulent sub-grid parameterization and (unphysical) numerical diffusion (e.g. Harris et al., 2001; Skamarock, 2004). This decrease in effective resolution has important implications since it is more pronounced in the high-resolution convection-allowing simulation at 1.2-km resolution than at 6-km resolution that requires a convective parameterization. Consequently the effective gain in nested dynamical downscaling is significantly reduced from a ratio of 5 between the 6- and 1.2-km resolutions to a ratio around 2 between the respective effective resolutions, demonstrating that a decrease in grid spacing without changing the numerical algorithm and the physical parameterizations does not yield to the desired improvement in the representation of small–scale processes.

The scaling analysis of instantaneous wind and atmospheric water fields shows that stochastic scale invariance holds closely, but with intrinsically transient scaling exponents depending on the atmospheric state. In particular a robust sharp transition of the scaling properties between stratiform and convective regimes is found for ensemble and instantaneous statistics of kinetic energy and total water content, both in the spectral analysis and in the multifractal intermittency parameter. This generalizes the previous results of Nogueira et al. (2013) who found a similar transition in rainfall and cloud fields in highly idealized orographic precipitation simulations. When no intense convective updrafts are present, the results displayed single nearly isotropic horizontal scaling behavior with $\beta \approx 2 - 2.3$ for ensemble and instantaneous statistics of wind and atmospheric water fields, from nearly the domain length scale (~700 km) down to about 5 km. As strong updrafts emerge, there is a clear change in the scaling behavior such that for intense convective events the estimated spectral exponents fluctuate at lower values, closer to 5/3. These results can explain two commonly observed scaling regimes (Nastrom and Gage, 1985; Nastrom et al., 1986; Lovejoy et al., 2004; Tuck et al., 2004; Tuck, 2008; Lovejoy et al., 2010a; Tuck, 2010). The $\beta \sim 2$ regime arises under stratiform or very weak convective conditions, when the spatial patterns are dominated by large-scale gradients and by landform. In fact, this scaling behavior was found to be very similar to the scaling of the underlying topography and commonly reported in the relevant literature (see e.g. Gagnon, 2006). When strong convective structures are present, the turbulent regime dominates with horizontal scaling exponents generally fluctuating under 5/3, in agreement Kolmogorov scaling accounting for the intermittency correction. The intermittency parameter, C_1, showed a transition from lower values in the 0.05-0.1 range under non-convective conditions, to higher values, here going as high as 0.3 when strong convective updrafts develop.

The implications of the properties of non-convective/convective transient scaling to stochastic sub-grid parameterization of clouds were investigated, using a fractal interpolation scheme to generate an ensemble of 50 total water content horizontal fields at 1.2-km resolution from the 6-km resolution simulated fields. The ensemble of PDFs derived from the fractal downscaled fields captured the high-resolution simulated PDF, representing a considerable improvement compared to the typically assumed log-normal distributions, even in the best case scenario when the latter statistics were obtained from the high-resolution fields rather than estimated from the coarse resolution as is generally the case. A spectral slope $\beta = 2.1$ is taken for fractal downscaling of

non-convective cases, representing the mean spectral slope obtained from transient scaling analysis when no strong updrafts are present. For convective cases a value $\beta = 1.5$ is assumed for fractal downscaling, representing the mean spectral slope from transient scaling analysis when strong updrafts exist. This simplifying assumption greatly reduces the computational requirements of a priori determination of the scaling parameters, which is notoriously difficult in limited-area simulation domains due to limited coarse resolution information together with the complex non-linear transient nature of the scaling properties of atmospheric fields (Nogueira et al., 2013). The results show that high-valued tails in non-convective cases are better represented when $\beta = 2.1$ is used compared to $\beta = 1.5$. Conversely the low- and high-value ends of the PDF in convective cases are better represented when $\beta = 1.5$ is taken compared to $\beta = 2.1$. This provides an independent confirmation of the non-convective/convective transition in scaling structure.

Consistent with the findings Berner et al. (2011), our results show that physically based stochastic methods can generate ensemble statistical distributions capable of accurately parameterizing sub-grid scale cloud fields in NWP. These methods can be generalized to any field for which stochastic scaling holds to a good approximation, hence representing an alternative to the current sub-grid parameterization scheme often based on oversimplified bulk empirical expressions that fail to reproduce reality in many occasions with important impacts to numerical weather and climate forecasts. An important future development will be the generalization of the 2-dimensional fractal downscaling methods to include horizontal anisotropy, which can play an important role under certain atmospheric states as shown here, particularly for kinetic energy fields in case S_SALLJ.

The sub-grid parameterization of clouds remains an important challenge to improve our weather and climate forecasts. This problem needs to be addressed in parallel to the current efforts to increase the resolving power of numerical models and the use of adaptive resolution grids, capable of dynamically embedding high-resolution regions depending on the local conditions (Skamarock et al., 2012; Randall et al., 2013). The use of such models is consistent with the present results demonstrating the dependence of the small-scale structure and energy distribution on the local dynamics and in particular the highly increase in resolution requirements that arise in regions where strong convective features emerge.

As a final note, it is important to stress that although the non-convective/convective distinction has proven valuable to characterize and understand different precipitation events, this distinction is far from straightforward due to the complexity of the numerous nonlinear physical processes at play in orographic precipitation, and in particular the wide variety of possible convective structures that represents a major challenge from both theoretical and predictability points of view, with important impacts to the obtained solutions. In fact, our results show that under the convective regime differences in the spectral slopes of 0.5 or larger can be found between different times and/or simulations. Additionally, the horizontal isotropic symmetry can be broken and restored throughout this dynamical evolution. Consequently, the convective range does not correspond to a unique scaling regime and distinct convective organizations can display different scaling behavior. Future work analyzing the scaling of a large number of events spreading over several locations and weather conditions can provide further refinement to the present binary non-convective/convective framework to include the ability to distinguish among different types of convective regime morphologies. In fact, Nogueira et al. (2013) showed different scaling regimes to exist between cellular and organized banded convection events. Paraphrasing Phillipe Saffman (1978), fitting all the diversity of orographic (and non-orographic) precipitation processes into the "Procrustean bed" of stratiform/convective regimes is likely an ultimately impossible task. However, there is a robust transition where the spectral exponent tends to fluctuate around 5/3 in the convective regime when strong updrafts dominate, while higher values are found in non-convective regime when strong updrafts are absent.

Acknowledgements

Xiaoming Sun performed the W_LLJ, S_LLJ and EDRY simulations using the WRF model. The work was supported in part by NASA NNX13AH39G and NSF EAR-0711430 grants. The first author was also supported in part by the Portuguese Foundation for Science and Technology (FCT) under grant SFRH/BD/61148/2009 and by project SMOG funded by FCT grant PTDC/CTE-ATM/119922/2010.

5 Overall conclusions

The dynamics of convective orographic precipitation was investigated, with particular focus on the transition between stratiform and convective regimes, relying on observational QPE and fully nonlinear 3-dimensional high-resolution numerical simulations of orographic precipitation events, under both highly idealized and realistic setups. Analytical linear stability analysis revealed some skill in qualitative prediction of the orographic convective structure resulting from idealized numerical simulations and also providing physical insight on the triggering and growth of deep convective structures in high-resolution numerical simulations of rainy season orographic convective precipitation events over the central Andes region under SALLJ conditions, where the easterly transport of warm moist flow towards the Andes eastern slopes gives rise to complex rainfall patterns. The linear model predictions on the dominant role of static instability magnitude, upslope wind speed and the role of landform over the foothills of the Andes in triggering convection were in clear agreement with the simulated results. However, the results also showed that such simple linearized models are unable to provide any quantitative predictions or even predict the correct spatial distribution patterns (except in very particular cases) due to the highly transient and intrinsically non-linear character of convective dynamics, including the decay of convective cells, interaction with synoptic-scale systems including flow deflection, blocking and channeling, interaction with local circulations (e.g. mountain/valley circulations associated with radiative fluxes) and diverse microphysical processes, amongst other effects. In other words, the resulting rainfall fields are modulated over wide ranges of spatial and temporal scales by numerous non-linear interactions amongst themselves, with terrain, radiative fluxes and local circulations giving rise to complex orographic cloud and rainfall spatial patterns with variability over a wide scale spectrum, as clearly shown by our results.

Statistical scale-invartiant behavior is found to be a convenient alternative framework to characterize and understand orographic convection due to its theoretical simplicity, its ability to handle nonlinear dynamics over wide range of scales, its potential for sub-grid downscaling and parameterization applications and its appropriate statistical treatment of these intrinsically turbulent flows. The scaling analysis of statistical moments, structure functions and Fourier power spectra clearly showed that multifractal behavior holds to remarkable approximations over wide ranges of spatial scales, from 1 km up to over 500 km length scales, for rainfall,

atmospheric water in its different phases (including clouds, vapor and total water mixing ratios), wind and topographic elevation. High-resolution NWP models at different horizontal resolution and under both idealized and realistic setups are able to reproduce the observed horizontal scaling behavior of atmospheric fields down to the model effective resolution length-scale, below which the models misrepresent the variability of atmospheric fields due to the finite grid spacing effects and limitations associated the sub-grid turbulent parameterization and (unphysical) numerical diffusion introduced to keep the model stable. The effective resolution was shown to be a transient property dependent on the particular simulated conditions, and also on the NWP formulation. NWP nested dynamical downscaling was shown to preserve the scaling behavior found in coarse resolution forcing, hence preserving the large-scale statistical structure from the (re-)analysis data with assimilated observations used to force the models. However, it was found that the gain in effective resolution can be lower than the grid-length ratio between parent and nested domains, particularly under strong convective setups, implying that a blunt decrease in grid spacing without adjusting numerical techniques applied may not lead to the improvements desired.

The scaling behavior of heavily thresholded fields such as rainfall and clouds is shown to be deformed by the presence of large fractions of zero values, causing breaks and curvature to the log-log linear relations. Traditionally, this problem has been handled considering only rainfall field realization with low zero fractions. However, when the domains have large spatial extent, such as the IPHEx domain extending over the southeastern US, this approach can bias the analysis towards large mesoscale convective systems and synoptic-systems and hence potentially not representative of more localized structures such as summertime orographic convection. An alternative method for spatial scaling analysis of thresholded fields was presented here, for the first time to the best of the author's knowledge, by using a cluster identification algorithm to isolate nonzero areas hence allowing a broader investigation covering several types of rainfall structures.

The spatial scaling analysis was extended beyond the typically considered ensembles averages over numerous realizations. Instead, large domains of high-resolution were used to rigorously investigate the dynamical evolution of the multifractal behavior, based on previous reports of variable scaling behavior and on the transient nature of orographic precipitation. The results for

all the analyzed observed and simulated atmospheric fields showed robust and important deviations from the ensemble scaling behavior that cannot be explained by uncertainty in the scaling analysis over limited samples. This behavior held for fields with barely any zero values (such as wind and water vapor) and also when the zero problem was explicitly taken into account in heavily thresholded fields and hence cannot be explained by the effect of zero values on scaling either. Consequently, the scaling exponents are intrinsically transient properties with complex nonlinear dependencies on the particular terrain forcing and atmospheric state, including mean wind speed and static stability. This result provides important evidence on the crucial but non-consensual question of whether the scaling behavior should be considered as a universal or a dynamical property of atmospheric fields. An important new result obtained here was the finding of a sharp transition in the scaling behavior between non-convective and convective regimes, which has a clear physical correspondence as a transition from less intermittent stratiform cases to more organized convective structure with more localized features. This result was robustly found in both idealized and realistic simulations for rainfall, wind, clouds, water vapor and total water content fields. This transition was first found in the highly idealized simulations in Chapter 2 and then generalized for the realistic simulations over the central Andes region, where the non-convective cases (when no intense convective updrafts are present) displayed robust unbroken nearly isotropic horizontal scaling behavior with $\beta \approx 2 - 2.3$ for ensemble and instantaneous statistics of wind and atmospheric water fields over the considered range of scales, from nearly the domain length scale 700 km down to about 5 km. When strong updrafts emerged, the results showed a clear change in the scaling behavior, such that for intense convective events the estimated spectral exponents fluctuate at significantly lower values, closer to 5/3. These results can explain two commonly observed scaling regimes: on the one hand, the $\beta \sim 2$ regime arises under non-convective or very weak convective conditions, when the spatial patterns are dominated by large-scale gradients and by landform. In fact, this non-convective scaling behavior was very similar to the scaling for the underlying topographic elevation found here and also commonly reported in the relevant literature (see e.g. Gagnon, 2006). When strong convective structures are present, the turbulent regime dominates with horizontal scaling exponents generally fluctuating below 5/3, in agreement Kolmogorov prediction accounting for the intermittency correction. Further robustness to this result was provided by the multifractal analysis, where the intermittency parameter, C_1, showed a transition

from lower values in the 0.05-0.1 range under non-convective conditions, to higher values, here going as high as 0.3 when strong convective updrafts develop.

The undertaken transient spatial multifractal analysis over an unprecedentedly large 3 years of hourly radar derived rainfall estimates covering a large-domain over the Southern Appalachian region, together with high-resolution NWP simulations of orographic convection under idealized and realistic setups provide important insights onto the structure of orographic rainfall and cloud fields, for which a comprehensive analysis on the spatial structure spanning over several atmospheric and terrain forcings was lacking in the state-of-the-art literature. The results agree with the generally found ability of NWP models to capture the main features of large-scale structures but with well-known shortcomings in representing timing, intensity, triggering, location and structure of localized convective features, highlighting the importance of resolution and suggesting that significant improvements can be obtained by sub-grid scale parameterizations capable of accurately representing the small-scale statistical structure. In this sense, the applicability of stochastic scaling behavior of atmospheric fields for stochastic sub-grid scale parameterization of clouds and for rainfall downscaling applications was investigated. The former represents a major source of uncertainty in NWP and climate models with important impacts to the solutions because of the interactions between clouds and radiation amongst other effects (e.g. Christensen et al., 2007; Zelinka and Hartman, 2012; Randall et al., 2013; Gianotti and Eltahohir, 2014). Rainfall downscaling applications are crucial to bridge the gap between observed/simulated data and the high-resolution requirements of many hydrometeorological applications (e.g. Barros and Lettenmaier, 1994; Bindlish and Barros, 2000; Harris et al., 2001; Rebora et al., 2006, Tao and Barros, 2013, 2014a). To this end, fractal interpolation methods were used here due to their theoretical simplicity, ease of implementation, continuity in the spectral domain and their ability to rapidly generate large ensembles of high resolution statistically robust fields without any additional data or calibration requirements.

In Chapter 3 hourly Stage IV rainfall fields at 4 km resolution were downscaled to the 1km resolution IPHEx grid using two types of fractal interpolation methods. In the first, a fixed value of the scaling exponent ($\beta_{Ens} = 1.9$) was considered as estimated from the ensemble analysis of 3 years of hourly radar derived rainfall estimates. In the second, transient spectral exponent estimated from the respective coarse resolution realization of the rainfall field was used. Both

methods were able to conserve the coarse resolution information while enhancing the small-scale variability, hence adding value to the original field. The transient estimation of the spectral scaling exponent resulted in better coherence between the sub-grid scale statistical structure and the respective coarse resolution information when the scaling behavior deviates significantly from the ensemble behavior. Additionally, the transient method also captured more accurately the high intensity rainfall statistics observed by a dense raingauge network, providing further support into the transient nature of the scaling behavior. Consequently StageIV_TF was chosen as representing the best fractal downscaling method and used to force hydrological simulations over the Pigeon River Basin in the Southern Appalachians. The hydrological simulations forced by the 1 km resolution ensemble averaged fractal downscaled fields overperformed the commonly used bilinear interpolation as expected. Non-fractal interpolation methods are unable to reproduce the subgrid-scale variability resulting in significant shortcoming in predicting extreme rainfall events associated with localized features, though the specific impact on skill metrics will necessarily depend on basin scale and geomorphic properties as well as the storm system proper. The results also show that the smooth character of the ensemble downscaled rainfall products resulting from averaging over several realizations cause an underestimation of the peak streamflow, particularly relevant for flashflood causing events extreme rainfall events such as the 2008 summer Tropical storm Fay case studied here. A more informative stochastic streamflow prediction was obtained by considering all the hydrological simulations forced by each of 50 single realizations of the fractal downscaled rainfall. The resulting spread of solutions was capable of capturing the observed intense streamflow peaks compared to the intrinsically smoother ensemble products. The stochastic forecasts were further enhanced by improving the resolution of fractal downscaled rainfall forcing to 250 m, resulting in reliable probabilistic forecasts and associated uncertainties with large value for extreme event forecasting and risk management.

In Chapter 4 a fractal interpolation scheme was used to generate an ensemble of 50 realizations of total water content fields at 1.2 km resolution from the 6-km resolution data. The q_t PDFs resulting from the ensemble of fractal downscaled fields showed skill in reproducing the q_t PDF explicitly simulated at 1.2 km resolution, representing a considerable improvement when compared to the usually assumed log-normal distributions. This improvement occurred even in the best case scenario, when a log-normal distribution was derived from the actual high-

resolution fields, rather than from the coarse resolution information, as is generally the case, causing further errors to the fitted log-normal distributions. A simplifying assumption was taken on the transient variability of the spectral slope, greatly reducing the complex problem of a priori estimation of the spectral slope: $\beta = 2.1$ was assumed in non-convective cases, representing the mean spectral slope obtained from transient scaling analysis when no strong updrafts are present; while $\beta = 1.5$ was considered for convective cases, representing the mean spectral slope from transient scaling analysis when strong updrafts exist. The results show that the high-valued tails in non-convective cases are better represented when $\beta = 2.1$ is used compared to $\beta = 1.5$. Conversely the low- and high-value ends of the PDF in convective cases are better represented when $\beta = 1.5$ is taken compared to $\beta = 2.1$. These results provide further robustness to the found convective/non-convective scaling transition. Furthermore, the present results open a promising path towards stochastic sub-grid parameterization of cloud fraction, that can be generalized to any field for which stochastic scaling holds to a good approximation, hence representing an alternative to the current sub-grid parameterization scheme often based on oversimplified bulk empirical expressions that fail to reproduce reality in many occasions with important impacts to numerical weather and climate forecasts.

It is important to stress that although the convective/non-convective distinction was proven valuable to characterize and understand different precipitation events, this distinction is far from straightforward due to the complexity of the numerous nonlinear physical processes at play in orographic precipitation and particularly the wide variety of possible convective geometries, representing a major challenge from both theoretical and predictability points of view with important impacts on the obtained solutions. In fact, the results show that under the convective regime differences in the spectral slopes as larger as 0.5 can be found between different times and/or simulations. Additionally, the horizontal isotropic symmetry can be broken and restored throughout this dynamical evolution. Consequently, the convective range does not correspond to a unique scaling regime and different types of convective arrangements can display different scaling exponents. This result is in agreements with the results of Nogueira et al. (2013) that found significant differences of the scaling parameters between cellular and organized banded convection. Making use of Phillipe Saffman (1978) pertinent words on turbulence classification, the task of fitting all the diversity of orographic (and non-orographic) precipitation processes into the “Procrustean bed” of stratiform/convective might be a very limited and ultimately impossible

task. However, there is a robust transition where the spectral exponent tends to fluctuate around 5/3 in the convective regime when strong updrafts dominate, while higher values are found in non-convective regime when strong updrafts are absent.

Given the numerous physical process involved in convective orographic precipitation and their attendant uncertainties, it is perhaps likely that confidence in any particular model prediction will always remain low. In this sense, the use of transient stochastic fractal methods with statistics conditional on large-scale conditions to rapdily generate stochastic ensemble forecasts of plausible, statistically coherent, solutions, together with the associated uncertainties, provides a promising path to improve the predictibility of these events, and their impact on hazardous extreme events and water management. Whether the produced fractal downscaled fields represent a plausible span of solutions and how this spread can be improved represents a promising topic of investigation, with important implications for stochastic weather forecasting. Also, the determination of the sub-grid scale asymptotic PDF directly from scaling arguments instead of derived from virtually generated downscaled fields will allow for operational use of the very promising stochastic sub-grid scale parameterization presented here. Towards this end, it is also critical to obtain a more complete understanding of the regime based dynamical variability of the scaling parameters in order to accurately estimate them from the coarse resolution information alone. Finally, the downscaling algorithms should be extended to explicitely account for horizontal anisotropy and intermittency, which can play important effects under certain atmospheric conditions.

References

Baldwin, M. E. and Mitchell, K. E., 1998: Progress on the NCEP hourly multi-sensor U.S. precipitation analysis for operations and gcip research. Preprints, 2nd Symposium on Integrated Observing Systems, 78th AMS Annual Meeting, 10-11.

Barros, A. P., *and* Lettenmaier, D. P., 1994: Dynamic modeling of orographically induced precipitation, Rev. Geophys., 32*(*3*)*, 265–284.

Barros, A. P., and Lang, T. J. , 2003: Monitoring the monsoon in the Himalayas: Observations in central Nepal, June 2001, Mon. Weather Rev., 131(7), 1408–1427.

Barros, A. P., Kim, G., Williams, E., and Nesbitt, S. W., 2004: Probing orographic controls in the Himalayas during the monsoon using satellite imagery. Natural Hazards and Earth System Science, 4 (1), 29-51.

Barros, A. P., S. Chiao, T. J. Lang, D. Burbank, and J. Putkonen, 2006: From weather to climate—Seasonal and interannual variability of storms and implications for erosion processes in the Himalaya, Spec. Pap. Geol. Soc. Am., 398, 17–38.

Barros, A. P. and Tao, K., 2008: A space-filling algorithm to extrapolate narrow-swath instantaneous TRMM microwave rain-rate estimates using thermal IR imagery. J. Atmos. Oceanic Technol., 25, 1901-1920.

Berg, P., Moseley, C., Haerter. J. O., 2013: Strong increase in convective precipitation in response to higher temperatures. Nature Geoscience, 6, 181-185.

Berner, J.,Ha, S.-Y., Hacker, J. P., Fournier, A., and C. Snyder, 2011: Model Uncertainty in a Mesoscale Ensemble Prediction System: Stochastic versus Multiphysics Representations. Mon. Wea. Rev., 139, 1972–1995.

Bindlish, R. and Barros, A. P., 1996: Aggregation of digital terrain data using a modified fractal interpolation scheme. Computers & Geosciences, 22 (8), 907-917.

Bindlish, R. and Barros, A. P., 2000: Disaggregation of rainfall for one-way coupling of atmospheric and hydrological models in regions of complex terrain. Global and Planetary Change, 25 (12), 111-132.

Bhushan, S., and Barros, A. P., 2007: A numerical study to investigate the relationship between moisture convergence patterns and orography in central Mexico, J. Hydrometeorol., 8, 1264–1284.

Bolgiano Jr., R., 1959*:* Turbulent spectra in a stably stratified atmosphere, J. Geophys. Res., 64*(*12*)*, 2226–2229.

Bony, S., and Emanuel, K. A., 2001: A parameterization of the cloudiness associated with cumulus convection: Evaluation using TOGA COARE data. J. Atmos. Sci., 58, 3158–3183.

Brussolo, Elisa, Jost von Hardenberg, Luca Ferraris, Nicola Rebora, Antonello Provenzale, 2008: Verification of Quantitative Precipitation Forecasts via Stochastic Downscaling. *J. Hydrometeor*, 9, 1084–1094.

Campetella, C., and Vera, C., 2002: The influence of the Andes Mountains on the South American lowlevel flow. *Geophys. Res. Lett.,* 29**,** 1826.

Christensen, J. H., and Coauthors, 2007: Regional climate projections. Climate Change 2007: The Physical Science Basis, S. Solomon et al., Eds., Cambridge University Press, 847–940.

Corsin, S., 1951: On the Spectrum of Isotropic Temperature Fluctuations in an isotropic Turbulence, J. Appl. Phys., 22, 469-473.

Cosma, S., Richard, E., and Miniscloux, F., 2002: The role of small-scale orographic features in the spatial distribution of precipitation, Quart. J. Roy. Meteor. Soc., 128, 75–92.

de Montera, L., 2009: The effect of rain-no rain intermittency on the estimation of the universal multifractals model parameters. J. Hydrometeor, 10, 493-506.

Deidda, R, 2000: Rainfall downscaling in a space-time multifractal framework, Water Resour. Res., 36, 1779–1794.

Deidda, R., Badas, M. G., and Piga, E., 2004: Space-time scaling in high-intensity tropical ocean global atmosphere coupled ocean-atmosphere response experiment (TOGA-COARE) storms. Water Resources Research, 40 (2).

Douglas E. M., and Barros, A. P., 2003.: Probable Maximum Precipitation Estimation Using Multifractals: Application in the Eastern United State, J. Hydrometeor, 4, 1012-1024.

Ebtehaj, A. M., Foufoula-Georgiou, E., Lerman, G., 2012: Sparse regularization for precipitation downscaling. J. Geophy. Res., 117, D08107.

Emanuel, K. A., 1994: Atmospheric Convection, Oxford University Press, New York.

Evans, J., 1996: A procedure for automated satellite-based identification and climatology development of various classes of organized convection. J. Appl. Meteor, 35, 638-652.

Ferraris, L., S. Gabellani, N. Rebora, *and* A. Provenzale, 2003*:* A comparison of stochastic models for spatial rainfall downscaling, Water Resour. Res., 39*, 1368.*

Ferreira, R. N., Rickenbach, T. M., Herdies, D. L. and Carvalho, L. M. V., 2003: Variability of South American convective cloud systems and tropospheric circulation during January–March 1998 and 1999. Mon. Wea. Rev., 131, 961–973.

Frehlich, R. G., and Sharman, R. D., 2010: Equivalence of velocity statistics at constant pressure or constant altitude, Geophys. Res. Lett., 37, L08801.

Foufoula-Georgiou, E.; Ebtehaj, A. M., Zhang, S. Q., and Hou, A. Y., 2014: Downscaling Satellite Precipitation with Emphasis on Extremes: A Variational ℓ_1-Norm Regularization in the Derivative Domain. Surveys in Geophysics, 35, 765-783.

Fuhrer, O., and Schär, C., 2005.: Embedded cellular convection in moist flow past topography, J. Atmos. Sci., 62, 2810–2828.

Fuhrer, O., and Schär, C , 2007.: Dynamics of Orographically Triggered Banded Convection in Sheared Moist Orographic Flows, J. of the Atmos. Sci, 64, 3542-3561.

Garreaud, R. D., Vuille, M. and Clement, A. C., 2003: The climate of the Altiplano: Observed current conditions and mechanisms of past changes. Palaeogeogr. Palaeoclimatol. Palaeoecol., 194, 5–22.

Gianotti, R. L., Eltahir, E., 2014: Regional Climate Modeling over the Maritime Continent. Part I: New Parameterization for Convective Cloud Fraction. *J. Climate*, **27**, 1488–1503.

Giovannettone, J. P., and Barros, A. P., 2009: Probing regional orographic controls of precipitation and cloudiness in the central Andes using satellite data. J. Hydrometeor., 10, 167–182.

Gires, A., Onof, C., Maksimovic, C., Schertzer, D., Tchiguirinskaia, I., and Simoes, N., 2012: Quantifying the impact of small scale unmeasured rainfall variability on urban runoff through multifractal downscaling: A case study. Journal of Hydrology, 442-443 (0), 117-128.

Gupta, V. K., and Waymire, E., 1991: On Lognormality and Scaling in Spatial Rainfall Averages? Non-linear variability in Geophysics, pp. 175-183.

Gupta, V. K., and Waymire, E. C., 1993.: A statistical analysis of mesoscale rainfall as a random cascade, J. Appl. Meteor., 32, 251–267.

Hamilton, K., Y. O. Takahashi, and W. Ohfuchi, 2008: Mesoscale spectrum of atmospheric motions investigated in a very fine resolution global general circulation model. J. Geophys. Res., 113, D18110.

Harris, D., Menabde, M., Seed, A. and Austin, G., 1996: Multifractal characterization of rain fields with a strong orographic influence. Journal of Geophysical Research: Atmospheres, 101(D21), 26, 405-414.

Harris, D., Foufoula-Georgiou, E., Droegemeier, K. K., and Levit, J. J., 2001: Multiscale statistical properties of a high-resolution precipitation forecast. J. Hydrometeor, 2, 406-418.

Houze, R. A. Jr., 2012*:* Orographic effects on precipitating clouds, Rev. Geophys., 50, *RG1001.*

Kahn, B., and Teixeira, J., 2009: A global climatology of temperature and water vapor variance scaling from the Atmospheric Infrared Sounder. J. Climate, 22, 5558–5576

Kahn, B., and Coauthors, 2011: Temperature and water vapor variance scaling in global models: Comparisons to satellite and aircraft data. J. Atmos. Sci., 68, 2156–2168.

Kim, G., and Barros, A. P., 2002: Downscaling of remotely sensed soil moisture with a modified fractal interpolation method using contraction mapping and ancillary data. Remote Sensing of Environment, 83, 400-413.

Kirshbaum, D. J., and Durran, D. R., 2004.: Factors governing cellular convection in orographic precipitation, J. Atmos. Sci., 61, 682–698.

Kirshbaum, D. J., and Durran, D. R., , 2005a.: Atmospheric factors governing banded orographic convection, J. Atmos. Sci., 62, 3758–3774.

Kirshbaum, D. J., and Durran, D. R. , 2005b: Observations and modeling of banded orographic convection, J. Atmos. Sci., 62, 1463–1479.

Kirshbaum, D. J., Rotunno, R., and Bryan, G. H. , 2007a: The Spacing of Orographic Rainbands Triggered by Small-Scale Topography, J. Atmos. Sci., 64, 1530-1549.

Kirshbaum, D. J., Bryan, G. H., Rotunno, R., and Durran, D. R., 2007b: The triggering of orographic rainbands by small-scale topography, J. Atmos. Sci,, 66, 1530-1549

Kolmogorov, A. N. , 1941: Local structure of turbulence in an incompressible liquid for very large Reynolds numbers, Proc. Acad. Sci. USSR. Geochem Sect., 30, 299–303

Koshyk, J. N., Hamilton, K., and Mahlman, J. D., 1999: Simulation of the $k^{-5/3}$ mesoscale spectral regime in the GFDL SKYHI general circulation model. Geophys. Res. Lett., 26, 843–846.

Koshyk, J. N., and Hamilton, K., 2001: The horizontal kinetic energy spectrum and spectral budget simulated by a highresolution troposphere-stratosphere-mesosphere GCM. J. Atmos. Sci., **58**, 329-348.

Kuo, H. L., 1963.: Perturbations of plane Couette flow in stratified fluid and origin of cloud streets, Phys. Fluids, 6, 195–211.

Lang, J. T., and Barros, A. P., 2002: An investigation of the onsets of the 1999 and 2000 monsoons in central Nepal, Mon. Weather Rev., 130, 1299–1316.

Lavallée, D., Lovejoy, S., Schertzer, D., and Ladoy, P., 1993.: Nonlinear variability and Landscape topography: analysis and simulation, Fractals in Geography, Eds. L. De Cola, N. Lam, 158-192, PTR, Prentice Hall.

Lazarev, A., Schertzer, D., Lovejoy, S., and Chigirinskaya, Y., 1994.: Unified multifractal atmospheric Dynamics tested in the tropics: part II, vertical scaling and generalized scale invariance, Nonlin. Processes Geophys., 1, 115-123.

Liebmann, B., Kiladis, G., N., Vera, C. S., Saulo, A. C. and Carvalho, L. M. V., 2004: Subseasonal variations of rainfall in South America in the vicinity of the low-level jet east of the Andes and comparison to those in the South Atlantic convergence zone. J. Climate, 17, 3829–3842.

Lilley, M., Lovejoy, S., Strawbridge, K., and Schertzer, D., 2004: 23/9 dimensional anisotropic scaling of passive admixtures using lidar aerosol data, Phys. Rev. E, 70, 036307.

de Lima, M. I. P., and de Lima, J. L. M. P. , 2009.: Investigating the multifractality of point precipitation in the Madeira archipelago, Nonlin. Processes Geophys., 16, 299-311.

Lin, Y. and Mitchell, K. E., 2005: The NCEP Stage II/IV hourly precipitation analyses: development and applications. Preprints, 19th Conf. on Hydrology, American Meteorological Society, San Diego, CA, 9-13.

Lovejoy, S., Schertzer, D., and Tsonis, A. A., 1987: Functional box-counting and multiple elliptical dimensions in rain, Science, 235, 1036-1038.

Lovejoy, S., Schertzer, D., and Tuck, A., 2004: Fractal aircraft trajectories and nonclassical turbulent exponents, Phys. Rev. E, 70, 036306.

Lovejoy, S., and Schertzer, D., 2007: Scale, scaling and multifractals in geophysics: twenty years on, Nonlinear dynamics in Geosciences, Ed. A.A. Tsonis, J. Elsner, Springer, 311-337.

Lovejoy, S., Schertzer, D., and Allaire, V., 2008a.: The remarkable wide range spatial scaling of TRMM precipitation, Atmos. Res., 90, 10-32

Lovejoy, S., Tarquis, A. M., Gaonac'h, H., and Schertzer, D., 2008b.: Single- and Multiscale Remote Sensing Techniques, Multifractals, and MODIS Derived Vegetation and Soil Moisture, Vadose Zone Journal, 7, 533-546

Lovejoy, S., Tuck, A., Schertzer, D., 2010a: The Horizontal cascade structure of atmospheric fields determined from aircraft data, J. Geophys. Res, 115, D13105.

Lovejoy, S. and Schertzer, D., 2010b.: Towards a new synthesis for atmospheric dynamics: space-time cascades, Atmos. Res., 96, 1–52,

Lovejoy, S., and Scherzter. D., 2010c: On the simulation of continuous in scale universal multifractals, part I: Spatially continuous processes, Computers & Geosciences, 36, 1393-1403.

Miniscloux, F., Creutin, J. D., and Anquetin, S. , 2001: Geostatistical analysis of orographic rain-bands, J. Appl. Meteor., 40, 1835–1854.

Mohr, K. I., Slayback, D., Yager, K., 2014: Characteristics of Precipitation Features and Annual Rainfall during the TRMM Era in the Central Andes. *J. Climate*, **27**, 3982–4001.

Nastrom, G. D., and Gage, K. S., 1985: A climatology of atmospheric wavenumber spectra of wind and temperature observed by commercial aircraft. *J. Atmos. Sci.*, 42, 950–960.

Nastrom, G. D., Jasperson, W. H. and Gage, K. S., 1986: Horizontal spectra of atmospheric tracers measured during the global atmospheric sampling program. J. Geophys. Res., 91, 13 201–13 209.

Nykanen, D. K., 2008: Linkages between orographic forcing and the scaling properties of convective rainfall in mountainous regions. J. Hydrometeor, 9, 327-347.

Nogueira, M., Barros, A. P., and Miranda, P. M., 2013: Multifractal properties of embedded convective structures in orographic precipitation: toward subgrid-scale predictability. Nonlinear Processes in Geophysics, 20 (5), 605-620.

Nogueira, M. and Barros, A. P., 2014a: Dynamical Downscaling of Quantitative Precipitation Estimation for Hydrological Predictions in the Southern Appalachians. Submitted to J. of Hydrometeo.

Nogueira, M. and Barros, A. P., 2014b: The non-convective/convective structural transition in stochastic scaling and its implications for NWP effective resolution and sub-grid parameterization, To be submitted

Over, T. M., and Gupta, V. K., 1994: Statistical analysis of mesoscale rainfall: Dependence of a random cascade generator on large-scale forcing, J. Appl. Meteor., 33, 1526–1542.

Obukhov, A., 1949: Structure of the Temperature Field in a Turbulent Flow, lzv. Akad. Nauk. SSSR Set. Geogr.l Jeofiz, 13, 55-69.

Paegle, J., Zhang, C. D. and Baumhefner, D. B., 1987: Atmospheric response to tropical thermal forcing in real data integrations. *Mon. Wea. Rev.,* 115**,** 2975–2995.

Parodi, A., Foufoula-Georgiou, E., *and* Emanuel, K., *2011:* Signature of microphysics on spatial rainfall statistics, J. Geophys. Res., 116, *D14119.*

Peters, O., Neelin, J. D., and Nesbitt, S. W. , 2009: Mesoscale Convective Systems and Critical Clusters, J. Atmos. Sci., 66, 2913-2924.

Perica, S., and Foufoula-Georgiou, E., 1996: Linkage of scaling and thermodynamic parameters of rainfall: Results from midlatitude mesoscale convective systems, J. Geophys. Res., 101, D3. 7431–7448.

Pinel, J., Lovejoy, S., Schertzer, D., and Tuck, A. F., 2012: Joint horizontal-vertical anisotropic scaling, isobaric and isoheight wind statistics from aircraft data. Geophys. Res. Lett., 39, L11803.

Pressel, K. G., Collins, W. D., 2012: First-Order Structure Function Analysis of Statistical Scale Invariance in the AIRS-Observed Water Vapor Field. *J. Climate*, **25**, 5538–5555.

Radkevich, A., Lovejoy, S., Strawbridge, K., and Schertzer, D., 2007: The elliptical dimension of space-time atmospheric stratification of passive admixtures using lidar data, Physica A, 382, 597-615.

Randall, D., Branson, M., Wang, M., Ghan, S., Craig, C., Gettelman, A. *and* Edwards, J., 2013*:* A Community Atmosphere Model With Superparameterized Clouds, Eos Trans. AGU, 94*(*25*)*, 221.

Rasmussen, K. L., and Houze Jr., R. A. , 2011: Orogenic convection in South America as seen by the TRMM satellite. Mon. Wea. Rev., 139, 2399–2420.

Rebora, N., Ferraris, L., von Hardenber, J., and Provenzale, A., 2006: RainFARM: Rainfall Downscaling by a Filtered Autoregressive Model. J. Hydrometeor., 7, 724-738.

Roe, G. H., 2005. Orographic precipitation. Ann. Rev. Earth Planetary Sci, 33: 645–671.

Romatschke, U., and Houze Jr., R. A., 2010: Extreme summer convection in South America. J. Climate, 23, 3761–3791.

Saffman, P. G., 1978: Problems and progress in the theory of turbulence, in Structure and Mechanis of Turbulence, II, ed. Fiedler, H., Lec. Notes Phys., Springer.

Schertzer, D., and S. Lovejoy, 1985: The dimension and intermittency of atmospheric dynamics, in Turbulent Shear Flow 4, edited by B. Launder, pp. 7–33, Springer, New York.

Schertzer, D., and Lovejoy, S., 1987: Physical modeling and analysis of rain and clouds by anisotropic and clouds by anisotropic scaling of multiplicative processes, J. Geophys. Res., 92, 9692-9714.

Schertzer, D., and Lovejoy, S., 1992: Hard and Soft Multifractal processes. Physica A, 185, 187-194,

Schmitt, F., Vannitsem, S., and Barbosa, A., 1998: Modeling of rainfall time series using two-state renewal processes and multifractals. Journal of Geophysical Research: Atmospheres, 103 (D18), 23, 181-193.

Skamarock, W., 2004: Evaluating mesoscale NWP models using kinetic energy spectra. Mon. Wea. Rev., 132, 3019-3032.

Skamarock, W. C., Klemp, J. B., Dudhia, J., Gill, D. O., Barker, D. M., Duda, M., Huang, X.-Y, Wang, W., and Powers, J. G., 2008: A Description of the Advanced Research WRF Version 3. NCAR Technical Note.

Skamarock, W. C., Klemp, J. B., Duda, M. G., Fowler, L., Park, S.-H., and Ringler, T. D., 2012: A Multi-scale Nonhydrostatic Atmospheric Model Using Centroidal Voronoi Tesselations and C-Grid Staggering Mon. Wea. Rev., 240, 3090-3105,

Smith R. B., 2006: Progress on the theory of orographic precipitation. Chapter 1 in Special Paper 398: Tectonics, Climate and Landscape Evolution. Willett SD, Hovius N, Brandon M, Fisher D. (eds). Geological Society of America: Boulder, Colorado.

Stolle, J., Lovejoy, S., and Schertzer, D., 2009: The stochastic multiplicative cascade structure of deterministic numerical models of the atmosphere. Nonlinear Processes in Geophysics, 16 (5), 607-621.

Sun, X., and Barros, A. P., 2010: An evaluation of the statistics of rainfall extremes in rain gauge observations, and satellite-based and reanalysis products using universal multifractals. J. Hydrometeor, 11, 388-404.

Sun, X., and Barros, A.P., 2014: Isolating the Role of surface evapotranspiration on moist convection and cloud formation along the eastern flanks of the Andes using a quasi-idealized approach. Submitted to J. *Atmos. Sciences*.

Tao, K. and Barros, A. P., 2010: Using fractal downscaling of satellite precipitation products for hydrometeorological applications. J. Atmos. Oceanic Technol, 27, 409-427.

Tao, J. and Barros, A. P., 2013: Prospects for flash flood forecasting in mountainous regions: an investigation of tropical storm Fay in the Southern Appalachians. Journal of Hydrology, 506 (0), 69-89.

Tao, J. and A. P. Barros, 2014a: Coupled prediction of flood response and debris flow initiation during warm and cold season events in the Southern Appalachians, USA. Hydrology and Earth System Sciences Discussions, 10 (7), 8365-8419.

Tao, J. and Barros, A. P., 2014b: The integrated precipitation and hydrology experiment. Part I: Quality high-resolution landscape attributes datasets. Report EPL-2014-IPHEX-H4SE 1, 60 pp. [EPL/Duke University (Pub.)].

Tao, J. and Barros, A. P., 2014c: The integrated precipitation and hydrology experiment. Part II: Atmospheric forcing and topographic corrections. Report EPL-2014-IPHEX-H4SE 2, 80 pp. [EPL/Duke University (Pub.)].

Takahashi, Y. O., Hamilton, K. and Ohfuchi, W., 2006: Explicit global simulation of the mesoscale spectrum of atmospheric motions. Geophys. Res. Lett., 33, L12812.

Terasaki, K., Tanaka, H. L, and Satoh, M., 2009: Characteristics of the Kinetic Energy Spectrum of NICAM Model Atmosphere. SOLA, Vol. 5, 180-183.

Tessier, Y., Lovejoy, S., and Schertzer, D., 1993: Universal multifractals: Theory and observations for rain and clouds, J. Appl. Meteor., 32, 223–250.

Vasiloff, S. V., Seo, Howard, D., Harold, D., Brooks, E. Zhang, J., Barbara, J., Brown, G., and Berkowitz, D., 2007: Improving QPE and very short term QPF: An initiative for a community-wide integrated approach. Bull. Amer. Meteor. Soc., 88, 1899-1911.

Verrier, S., de Montera, L., Barths, L. and Mallet, C. , 2010: Multifractal analysis of African monsoon rain fields, taking into account the zero rain-rate problem. Journal of Hydrology, 389 (12), 111-120.

Verrier, S., Mallet, C. and Barths, L., 2011: Multiscaling properties of rain in the time domain, taking into account rain support biases. Journal of Geophysical Research: Atmospheres, 116 (D20).

Yoshizaki, M., Kato, T., Tanaka, Y., Takayama, H., Shoji, Y., Seko, H., Arao, K., and Manabe, K. , 2000: Analytical and numerical study of the 26 June 1998 orographic rainband observed in western Kyushu, Japan. J. Meteor. Soc. Japan, 78, 835–856